DOCTORAL DISSERTATION

Inkjet printing of perovskite solar cells

Barbara Wilk

Supervisors:
Prof. Robert Kudrawiec, PWr
Konrad Wojciechowski Ph.D., SRI

Wrocław 2022

Table of contents

Abstract

The work documented in this thesis concerns the development of perovskite solar cells fabrication by inkjet printing technique. Recently, solar cells based on perovskite absorbers have emerged as one of the most promising photovoltaic technologies. After a decade of intensive scientific research, perovskite solar cells are now approaching the commercialization stage. At this moment the production of large-area devices is still to be established. Inkjet printing is one of the solution-based methods which can satisfy the requirements for fast and cheap thin film deposition. Herein, the boundaries of perovskite research are pushed towards industrial prospects by tackling the challenge of scalable film formation in air conditions. In this work, the development of inkjet printing was carried out for a few different perovskite formulations and one electron transport layer.

Initially, this thesis gives an overview of the most important properties of perovskite materials pointing out the bright sides as well as the challenges of perovskite solar cells technology.

The second chapter provides the guide through the inkjet printing technique necessary to understand the correlations between the ink properties, deposition parameters and substrate surface energy. This section explains the complexity of inkjet printing and addresses the challenges of printing process development.

The experimental part consists of three publications and one patent application submitted during this PhD track.

The first experimental chapter reports the design of mixed cation perovskite ink and its stability. The work focuses on finding green solvent composition and adjustment of coordination chemistry in the perovskite precursor solution. The study points out the importance of careful evaluation of ink stability, especially for perovskite ink formulation where chemical interactions can strongly affect the ink properties. By understanding the coordination mechanisms occurring in the precursor solution the sufficient reliability of the ink is obtained leading to printable devices of 11.4% power conversion efficiency (PCE) on a flexible substrate.

The second study is concerning the printing and post-processing of quasi-2D perovskite. In this work, the correlation between crystallization conditions and specific phases distribution is being analysed. Adjustment of the ink composition and optimization of the drying method allowed to achieve good morphology and crystallinity of the film. Inkjet-printed devices surpassed 14% PCE on glass and 10% on flexible substrates, being one of the highest results for flexible quasi-2D perovskite solar cells up to date.

In the next publication, inkjet printing is evaluated for electron transport layer deposition. The ink based on a new fullerene material ([6,6]-phenyl-C61 butyric acid n-hexyl ester; $PCBC_6$) is composed to meet inkjet criteria, and printing parameters are optimized to obtain uniform coverage. Perovskite solar cells with printed $PCBC_6$ reached efficiency similar to

fully spin-coated devices showing high applicability of inkjet printing for the fabrication of multiple layers stack of perovskite solar cells.

The last part of the experimental section attached as a description of the patent application addresses the challenge of inorganic perovskite processing. The innovative method of introducing an additional seeding layer to the solar cell device stack allows to drastically decrease the temperature of $CsPbI_3$ perovskite phase crystallization allowing the use of polymeric substrates and making the process more industrially viable. The procedure developed during this study has a high implementation potential for inorganic perovskite printing as well as for other solution-based coating processes.

Acknowledgements

First and foremost I would like to thank my supervisor at Saule Research Institute Konrad Wojciechowski, Ph.D. for giving me professional scientific support without limiting my freedom in the research. I am very grateful for this fruitful cooperation during the whole Ph.D. project. Thanks to You my crazy ideas could become valuable scientific insights.

I would like to thank my supervisor at Wrocław University of Science and Technology prof. Robert Kudrawiec for making my academic experience smooth and joyful. Big thanks for the scientific inputs and for introducing me to the world of physics.

Thanks to CTO of Saule Technologies: Olga Malinkiewicz, Ph.D. for giving me the possibility of combining education with a professional career.

Big thanks to the whole Saule Technologies and Saule Research Institute team, for all the smiles and words of support during late hours in the lab.

Special thanks to my family and friends for believing in me and supporting my ambitious plans.

Motivation and hypothesis

The constant growth of global energy demand driven by industrialization and population increase challenges the energy production sector.[1] Omnipresent electricity became essential to maintain the basic day-to-day living of modern society. Available at a flick of a switch, electricity is often taken for granted, forgetting that every single watt of power needs to be first somehow generated and delivered. Huge consumption of fossil fuels used for electricity generation comes at a price to the environment. Carbon dioxide emission accused of climate change and rising prices of natural gas and crude oil are warning signs of the upcoming energy crisis.

In order to satisfy the rising demands and avoid catastrophic consequences, outdated processes need to be supported by environment-friendly alternatives. Improving cost-competitiveness of renewable technologies and dedicated policy initiatives are being addressed to secure the energy sector.

Renewable sources of energy are expected to satisfy 27% of the need by 2050 which is a 165% increase compared to its share in 2020.[1] Technological advances provide various solutions of clean energy production including tidal energy, geothermal, bioenergy, and renewable synthetic fuels, however, solar energy and wind are currently holding the biggest potential due to their availability and technological maturity.[2]

The sunlight that radiates our planet dwarfs all the other energy sources. According to the World Energy Council, every day the flux of 1000 W/m^2 arrives at the surface of Earth, equivalent to 1.08×10^8 GW of power. This value represents 7000 times more energy needed daily by the whole planet.[3] In a view of those numbers, it becomes clear that solar energy conversion is of vital importance among scientists and engineers. The history of commercial photovoltaics (PV) reaches 1954 when the first silicon solar cell able to convert sunlight into electricity was presented by Bell laboratories.[4] After that, the research progressed rapidly driven mostly by space applications. The solar cell structure and the methods of fabrication were evolving bringing more and more efficient devices. Up to now, the PV market consists of a few generations of devices with still dominant silicon solar cells, thin-film photovoltaics as well as polymer, organic, and hybrid photo converters with power conversion efficiencies above 20%.[5] Researchers are trying to find new materials and develop new methods of solar cell production in order to absorb the sunlight more efficiently and reduce manufacturing costs. Thus, thin-film photovoltaics offering flexibility and simplified production processes are gaining interest in the field.

Perovskite solar cells (PSC) appeared on the photovoltaics playground merely 10 years ago and quickly became one of the front-runners on the power conversion efficiency chart reaching 25.7%.[5] The hybrid organic-inorganic, synthetic compounds with perovskite crystal structures were found to be extremely attractive as light absorbers. Their optoelectronic properties like high absorption coefficient, bandgap tunability, defect

tolerance attracted the attention of many scientists around the world.[6]–[8] The extensive research led to the outstanding performance reached on versatile device configurations which together with a low-cost production (low-temperature solution process) makes them very attractive also commercially-wise. Due to their lightweight, high performance in low light conditions (40.1% under 824.5 lux), flexibility, colour tunability perovskite solar cells can offer new functionalities extending the market beyond rigid, heavy rooftop installations. [9][10]

Considering the great economic prospects of this technology, the research is pushed towards the development of commercially viable processes enabling large scale production. In order to enter the market, a few shortcomings need to be mitigated. Perovskite technology underwent rapid technological development, but industrial reliability is still to be proven. The stability and performance of large-area modules, as well as the production process, need to meet the requirements of an extremely competitive utility-scale PV market.

The PhD track of Barbara Wilk was conducted as an Implementation Doctorate Programme in Saule Research Institute (SRI). SRI is a foundation established to carry out scientific projects in the field of optoelectronics. Projects are focusing on the fundamental understanding of physical phenomena behind the solar cell performance as well as processing development and chemical synthesis optimization of functional materials used in the field. Currently, perovskite solar cells are one of the topics studied in the institution. The Ph.D. research presented in this thesis was performed within the *First Team* project titled: *Enhancement of structural stability and operational reliability of perovskite solar cells* led by Konrad Wojciechowski, Ph.D. The program was aimed to develop scalable inkjet printing processes of perovskite materials with intrinsically enhanced stability.

The hypothesis stated in this thesis is that inkjet printing is capable of large-area deposition of various perovskites and adjacent layers building perovskite solar cells. The main objective arises from the need of expanding the knowledge on various perovskites crystallization, as well as inkjet ink design, printing parameters optimization and methodologies of layers post-treatment. To pursue this goal, the printing of three different perovskite materials (mixed cation perovskite, 2D perovskite and inorganic perovskite) and one functional layer was optimized. The study shows the importance of ink composition adjustment, ink rheology and stability analysis as well as careful selection of crystallization parameters. As a result of presented work, three scientific publications and one patent application were issued. The research conducted in this thesis delivered ink compositions and methodology of printing new perovskite compositions with a high potential of implementation into perovskite solar cells production.

1. Basic principles of solar cell operation

The solar cell is defined as a light-absorbing material (normally a semiconductor) connected to the external circuit keeping the electrical asymmetry enabling extraction of carriers generated by photoexcitation. In the dark it acts as a diode, conducting the current only in one direction. Upon illumination, photons with energy greater than the bandgap of a given semiconductor, are being absorbed promoting the electron from the valence band to the conduction band. The excited electron is bound by Coulombic force with a hole created in the valence band forming an electron-hole pair called exciton. The strength of electron-hole attraction (so called binding energy) is defined by the dielectric constant of the semiconductor, thus it varies between materials. Due to built-in asymmetry (difference in electron affinity of adjacent layers) the exciton can split and electrons and holes can be extracted. This asymmetry can be provided by specific doping of one material into p-type (electron-deficient) and n-type (electron excess) and creating p-n homojunction or by sandwiching an intrinsic semiconductor between n-type and p-type materials (heterojunction). When p-type and n-type materials are joined together, the difference in electrons concentration force a migration of carriers towards the balance. Firstly, carriers diffuse towards the interface and recombine forming a depletion region. When electrons (and holes) move, they leave the core ions behind (negative in the p-type material and positive ions in the n-type) creating an electric field in the junction. The higher the doping density, the higher electric field is established and thus higher built-in potential (V_{bi}). The magnitude of V_{bi} is equal to the difference between Fermi levels of two semiconductors. Upon illumination, the density of carriers increase breaking the thermal equilibrium and causing a Fermi level split into two quasi-Fermi levels. [11]

The operation of a solar cell is described by its current-voltage (*I-V*) characteristic (figure 1.1). The current produced when two terminals are connected is called the short circuit current (I_{SC}) and it is the point where the *I-V* curve cross with Y-axis. The voltage when the circuit is open and the current flow is zero is called an open-circuit voltage (V_{OC}) and it is an *I-V* intersection with X-axis. During the normal operation upon a load with resistance R, the voltage can vary between zero and V_{OC} and the current is between zero and I_{SC} according to the Ohm law (*V = IR*). As the current values are directly proportional to the active area of the illuminated device it is often presented as current density (J_{SC}) expressed in mA/cm^2.[11]
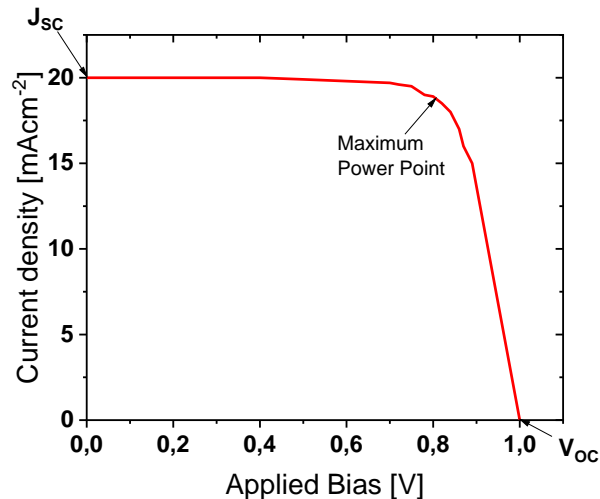
Figure 1.1 Current-Voltage (J-V) characteristic of a solar cell

The amount of generated current depends on the incident light spectrum and the bandgap of the absorber. Only the light with energy higher than the bandgap can promote the electron to the conduction band and enable its extraction. Thus, the bandgap of the material must be suitable for a given light spectrum to be able to convert it into current.

The voltage of a solar cell is defined by the energy difference between quasi-Fermi levels of the extracted electron and hole thus by the bandgap of the absorber. In real conditions, it is always reduced by non-radiative recombination processes. In a polycrystaline absorber the defects in the lattice and on the grain boundaries are a dominant source of this recombination, so the morphology of the film plays a crucial role in maximizing the device performance.

The power generated by the solar cell is the product of voltage and current. The point on the curve where it reaches the maximum value is called Maximum Power Point (MPP). In a working solar cell, this point is always below the theoretical maximum which could be obtained with maximum voltage (V_{OC}) and Current (J_{SC}). The deviation from the theoretical maximum is called Fill Factor (FF) and it is expressed in percentage. The most important parameter describing the solar cell operation is power conversion efficiency (PCE) which is a ratio between the power density generated by the device to the incident light power density.[11]

The power conversion efficiency is directly related to the amount of the absorbed photos, thus to the spectrum of incident light flux. In order to standardize the solar cells measurements, a fixed solar spectrum reference is established which represents the solar spectrum at ground level for mid-latitude regions at a solar zenith angle of 48°. It is called an Air Mass 1.5 spectrum (AM 1.5) and it was calculated for a yearly average at mid-latitudes. Similarly the standard irradiance is assumed based on average value equal 100 mW/cm^2. The standardized solar irradiance is shown on figure 1.2.

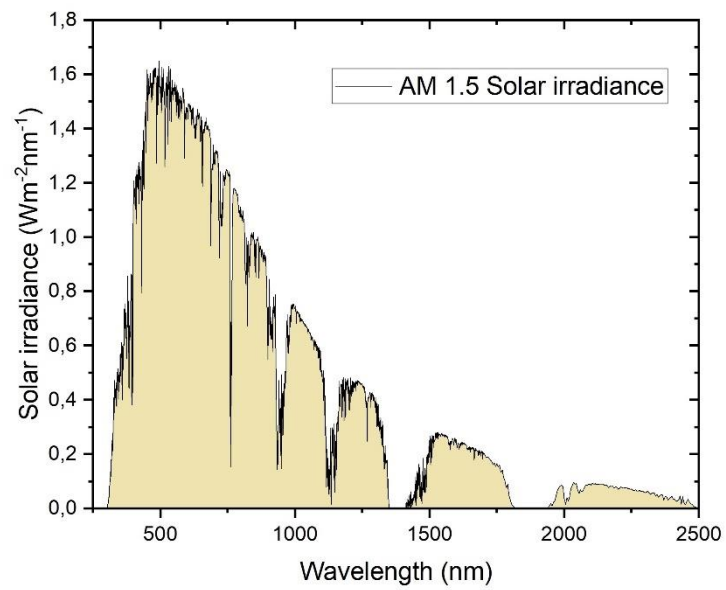*Figure 1.2 Standardized solar spectral irradiance AM 1.5*[12]

It is important to note that each solar cell utilize only a specific part of the whole spectrum according to its bandgap. An interesting strategy to extend the range of absorption is to combine two different materials with shifted absorption onset creating a tandem cell. In this way more light can be absorbed, thus more current is generated.

2. Perovskite Solar Cells

2.1.Definition of perovskite

The term perovskite relates to the group of compounds sharing a typical crystallographic structure belonging to the *Pm3m* crystallographic space group. Those materials have a general formula ABX_3 and a cubic shape unit cell with a B atom placed in the centre. The A atoms are positioned on the vertices of the cube and there is one X atom on each wall creating a BX_6 octahedron.[13][14] The structure of a unit cell is presented in figure 2.1.
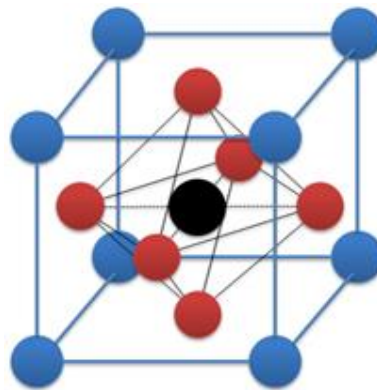

Figure 2.1 The unit cell of a perovskite

The fact that many different atoms can fit into A, B and X positions makes this group very diverse. Materials with this crystallographic structure include naturally existing inorganic minerals (like $MgSiO_3$, $CaTiO_3$), and synthetic ceramics (like $BaTiO_3$) or hybrid organic-inorganic compounds where the A atom is replaced by an organic group. Upon substitution of atoms, certain distortions may occur due to a change in the atoms' radius. The limitation in a selection of atoms is described by a Goldschmidt tolerance factor (t) which specify that the ionic radius of atoms has to stay in this relation:

$$R_A + R_X = t\sqrt{2(R_B + R_X)}$$

where, R_A, R_B, and R_X are the relative ionic radii of the A site, B site cations and X anion.

The perfect perovskite crystal has *t = 1* and it was calculated for the first discovered perovskite: $CaTiO_3$. This factor allows predicting whether the atoms can form a perovskite shape lattice. A desired, cubic structure is stable for values of t in the range between 0,89 to 1. The smaller values of *t* give an ilmenite symmetry and factors above 1 lead to the hexagonal perovskite structure.[15]

Perovskites gained interest in 2009 when Japanese researcher Miyasaka and his colleagues reported the application of a hybrid perovskite compound (with a formula $CH_3NH_3PbI_3$ known as MAPI) as a light absorber in dye-sensitized solar cells.[16] In MAPI the cubic phase is stabilized at a temperature above 330K. Upon decreasing the temperature the rotational disorder of PbI_6 can occur leading to a phase transition to tetragonal (160-330K) and

orthorhombic (below 160K)[17]. In 2012 the same compound (MAPI) was successfully applied to build a solid-state device which was a key discovery which triggered a broad research of perovskite solar cells.[18][19] During 12 years, the power conversion efficiency of perovskite photoconverters increased from initial 3.8% to 25.5%.[5] This exceptionally fast, compared to other PV technologies, progress was witnessed due to the intensive research of the scientist from the entire world. The path of efficiency enhancement led through the modification in device architecture, incorporation of new carrier transport materials and compositional engineering of the absorber layer. Up to 2019 over 16000 scientific reports concerning this topic were published and the number of publications per year keeps rising.[20] The exploration of the unique properties of halide perovskite materials is still a popular topic in many fields of science. The attractiveness of Miyasaka's discovery arises from the fact that it is not only one candidate for an absorber but the whole family of materials with tuneable optoelectronic properties, which can be used to build efficient solar cells.

Elemental compositional engineering of halide perovskites led to the creation of totally new materials like mixed perovskites, where A and X sites are occupied by a few different groups/atoms (e.g. $Cs_{0.1}FA_{0.75}MA_{0.15}PbI_{2.49} Br_{0.51}$) and low dimensional perovskites (quasi-2D, 2D, 1D or 0D) where the long-chain compounds are employed.

The following section will describe the most important properties of halide perovskites explaining why these materials became the front runners among emerging photovoltaic materials.

2.2.Advantages and challenges of perovskite solar cells

Every technology has its advantages and the draw-backs. Following paragraph will highlight the most important aspects of perovskite solar cell technology including the most attractive optoelectronic properties and stability concerns.

2.2.1.Optoelectronic properties of perovskites

- Tunability

The most attractive feature of perovskites is the tunability of their optoelectronic properties by compositional engineering. There is a whole range of possible candidates which fit into the *A*, *B,* and *X*-site of perovskite cage. It was found that the substitution or intermixing of some atoms allows to keep light harvesting properties, but altering some of the electronic properties (most importantly the bandgap). Such a compositional engineering of crystalline perovskites can be easily done by doping at the precursor solution stage leading to the whole variety of perovskite compounds with the bandgap ranging from 1.2 to 3.55 eV.[7], [21], [22]

Upon mixing halides at the *X* position the PL signal varies from visible to the near-infrared region.[7] Figure 2.2 shows the tunability of absorption (colour) of $MAP(I_{1-x}Br_x)_3$ upon changing the Br content. There is almost a linear relationship between the Br content and the bandgap of perovskite (figure 2.2b).

In ABX_3-type metal-halide perovskites, the valence band maximum is formed from an antibonding hybrid state of the metal *s* and halide *p* orbitals. The conduction band minimum is a hybrid of metal *p* and halide *p* orbitals. Thus, when the X element is replaced by other with different electronegativity, the orbital's energy change, and so is the bandgap.[23]

The observed decrease of the bandgap by replacing X ions going from bromide to iodide is accompanied by the decrease in the effective mass of the exciton and the decrease of the exciton binding energy what is the result of an increased difference in electronegativity between Pb and Br. Similarly, the substitution of the lead cation on the B-site (e.g. by tin) changes the bandgap of the material. Replacing B and X atoms induce the difference of orbital energies, thus the metal-halide orbitals overlap. The more electronegative X-site atom, the lower-energy valence band, and therefore a larger bandgap.[24]

The bandgap can be also tuned by A-site cation replacement. Substitution of formamidinium (FA) group by smaller cesium cation (Cs^+) alters the character of B-X bonds by steric and Coulombic interactions and induces a tilt of X-Pb-X dihedral angle changing the orbitals overlap which in turn causes an increase of the bandgap.[25] Interestingly, in the case of tin-based perovskites the same caesium doping does not cause the tilt but only the isotropic lattice contraction (due to smaller size of Cs atoms), thus the effect is opposite (decrease of the bandgap).[23] Figure 2.2c shows the effect of caesium doping in lead and tin halide perovskite. The competitive effects of octahedral tilt and lattice contraction on the bandgap of these materials provide a strategy to tune its value in a wide range between 1.2 to 1.7 eV.

Octahedral tilts in halide perovskites may also originate from the H-bondings between organic groups and halide frame. Theoretical calculations have shown that tuning the degree of hydrogen bonding can be used as an additional control parameter to optimize the photovoltaic properties of perovskites.[26]

The ability to tune the bandgap of perovskite materials is intriguing for the field of optoelectronics as it opens the possibility for tandem architectures, where, by combining materials with different absorption onset the absorption range is extended leading to higher conversion efficiency.
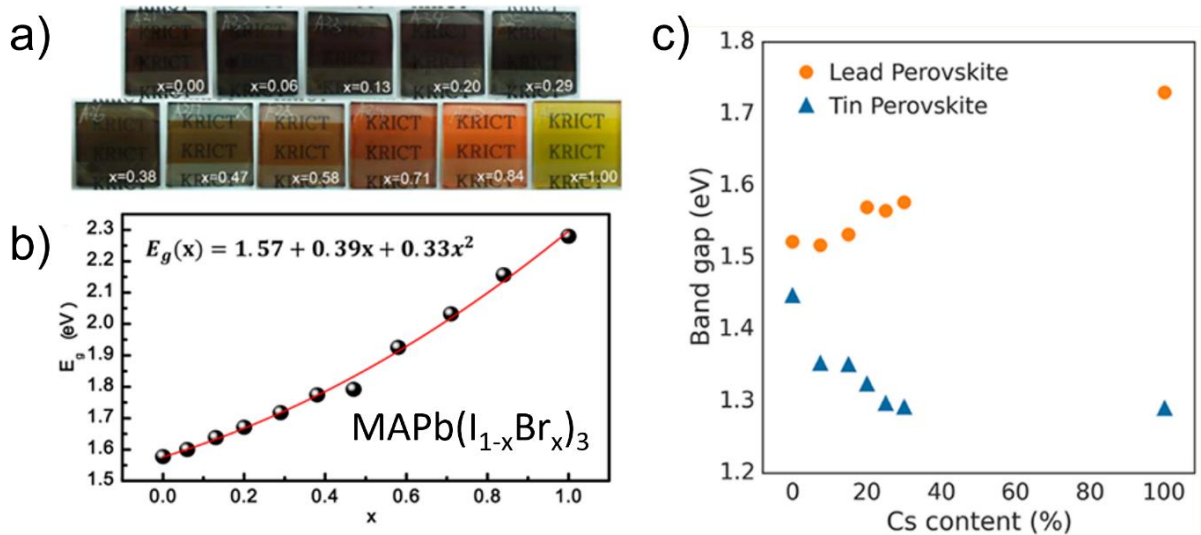
Figure 2.2 The change of colour(a) and the bandgap (b) of MAP(I$_{1-x}$Br$_x$)$_3$ perovskite as a function of Br content. Adapted with permission from [7]. Copyright 2013 American Chemical Society. C) Change in the bandgap of lead and tin perovskite upon caesium doping. Reprinted with permission from [23].Copyright 2017 American Chemical Society

- Defect tolerance and efficient charge transport

Due to the less controlled nature of solution-process fabrication and polycrystalline nature of perovskite films few types of defects can occur in the perovskite lattice including vacancies, interstitials, and substitutions of atoms. The density of defects is defined by growth conditions and solution composition. The impact of the defect depends on the nature of the state. The imperfection of the lattice can serve as a recombination centre for electron and hole (when located in the middle of the bandgap) or as a trap state (when closer to the valence or conduction band).[11] Density functional calculations used to elucidate the effect of defects on MAPbI$_3$ showed that the formation of deep trap states is energetically unfavoured and most of the defects are formed close to the bands.[8] The deep defects, responsible for non-radiative recombination, have higher formation energy so they are less probable to form. Thus, perovskite materials are often described as defect-tolerant, because small lattice imperfections are negligible for the solar cell operation if the layer is compact (no voids between the grains). If the layer has poor morphology the transport of carriers is impeded and the non-radiative recombination might occur at the grain boundaries. [27]

Additionally, high carrier mobility (for both electrons and holes) reaching tens of cm^{2}V^{-1}s^{-1} and their long lifetimes in halide perovskites provide very efficient charge transport through the absorber.[28] The values of diffusion lengths of halide perovskites reach 380 um for single crystals and vary between 100 and 1000 nm in polycrystalline layers depending on the composition and fabrication method.[29]–[31] In a solar cell with good quality crystalline perovskite the transport is mostly limited by ETL and HTL layers and the interface recombination.[32]

- High absorption coefficient

The absorption coefficient is one of the most important properties of a solar cell absorber. It determines how deep into a material light of a particular wavelength has to penetrate before it can be absorbed. Thus, it defines how thick the layer of a given absorber must be to absorb the light and convert it into electrical energy.[11] Perovskite materials show a high absorption coefficient, so the layer of only a few hundreds of nm suffice the solar cell. The values of the absorption coefficient (for 220 nm of MAPI) plotted against the photon energy are presented in figure 2.3 together with the values for different semiconductors used in photovoltaics including amorphous silicon (a-Si), GaAs, CIGS, CdTe, and crystalline silicon.
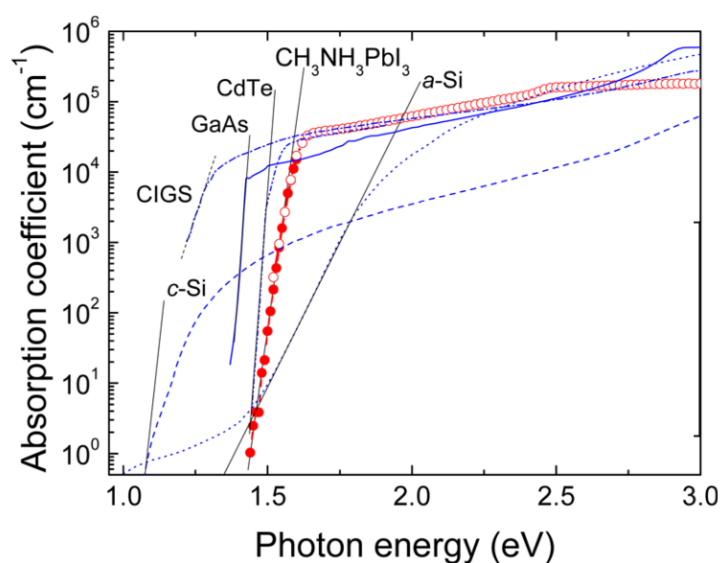
Figure 2.3 Comparison of absorption coefficient spectrum for MAPI perovskite and other absorbers. Reprinted with permission from[6]. Copyright 2014 American Chemical Society

It can be seen from figure 2.3 that MAPI shows a sharp shoulder near its bandgap value (1.57 eV). The calculated from this graph Urbach energy is 15 meV which is very low compared to other materials.[6]

2.2.2.Challenges

The main factors influencing commercial consideration for the energy-generating asset are performance, cost, and stability.[10] Perovskite solar cells reached an impressive performance surpassing 25%, so their potential is not questionable. The cost of the perovskite module is still unknown, as the large scale production is still to be explored. However, the low-temperature solution process is expected to give a cost-competitive product. Thus, long-term stability remains the biggest concern in the field.[33] Perovskite instability can originate from intrinsic lattice strain or can be induced by external

factors.[34] As it was mentioned before, the size of atoms constituting the perovskite lattice affects the stability of the structure.[35] Deviation of tolerance factor induces the distortion in the lattice affecting its thermodynamic stability.[36] As an example, the replacement of the methylammonium group by a bigger formamidinium group cause the formation of hexagonal non-perovskite phase at room temperature. The formation of cubic phase FAPI perovskite is possible, however it requires a higher annealing temperature (150°C). Similarly for the $CsPbI_3$, where A cation is much smaller, at room temperature, the formation of the non-perovskite orthorhombic phase is favoured. [37]

Solar cell operating in real conditions is subjected to external factors like light, heat, oxygen and moisture. Thus, the stability under these stressing conditions has to be considered. The ionic nature of perovskite lattice results in easy degradation in the presence of moisture. It was shown that MAPI perovskite can form hydrates with water molecules, which cause the structural deformation of $(PbI_6)^{4-}$ octahedra, weakening the bonds with A-site moiety, and making it more sensitive to heat and bias. Upon complete saturation, the hydration causes decomposition to initial precursors (CH_3NH_3I and PbI_2).[37]

Another origin of perovskite degradation is volatility of an organic part. It was shown that the methylammonium group can escape the lattice at an elevated temperature of 85°C as methylamine and hydroiodic acid gas. [38]

Under illumination, mobile ions trapped in perovskite lattice (mostly iodine) can move, inducing local compositional changes, which affect optoelectronic properties.[39] In the mixed halide formulations, this phenomenon can also cause phase segregation.[40][41] Additionally, the migration of ions upon operating conditions is a source of hysteretic behaviour observed on J-V curves, while biasing the device in the reverse and forward direction.[42] Moreover, the most mobile iodide ions can penetrate through the device and interact with adjacent layers, often resulting in degradation of metal electrodes.[43]

Most of the abovementioned issues can be improved by compositional engineering of the perovskite absorber. A strategy to overcome thermodynamic instability is using mixed atoms at the A site. It was shown by mixing atoms/groups with different sizes the thermodynamic criteria can be mitigated and intrinsic stability is greatly improved.[44] Replacement of volatile methylammonium group by formamidinium group, which creates stronger bonds with Pb octahedra, enhance the thermal stability of the material. The introduction of Cs cations improves further the thermal stability because of its primary bonding with PbX_6 which is stronger than H-bonds created by organic groups. The moisture resistance is greatly enhanced for 2D systems where a hydrophobic chain is introduced in the lattice. [45][46]

Another strategy to improve the stability of perovskites is additive engineering. Many compounds have been shown to have a beneficial impact on perovskite lifetime. Additives can be implemented directly into precursor solution or as a post-treatment (passivation). There are different mechanisms of stabilization including restricting the movement of ions, passivation of trap states, filling the vacancies in the lattice or surface modification. [37][47]

The stability of a solar cell is also affected by its architecture. Compositional engineering at the perovskite/charge carrier transport layer interface by chemical modification, interlayers, or replacing electrodes into more inert ones are some of the topics studied in the field.[48]–[50]

Despite scattering in data and claims, there is a consensus that the overall stability of perovskite solar cells is affected by perovskite composition and device architecture. Both considerations need to be addressed to facilitate their commercial uptake.

2.3. Architectures of PSC

Perovskite solar cells can be built in a few different architectures. In the early attempts, PSCs were fabricated in analogy to Dye-Sensitized Solar Cells (DSSC) containing mesoporous oxide as an electron transport layer. Typically, titanium oxide (TiO_2) was used what required a high temperature (>500°C) for the sintering step limiting the choice of the substrate to glass.[51] As the research advanced, new device structures with different ETLs were proposed.[52] Especially the work provided by Snaith et al which proved the possibility of using hybrid perovskites in the planar configuration (without mesoscopic scaffold) due to their ambipolar character and long carrier diffusion length pave the way towards high efficiency planar devices.[53] Nowadays, those planar architectures are the most commonly studied in the field.[54] The typical stack contains a transparent conductive oxide(Indium Tin Oxide-ITO or fluorinated tin oxide-FTO), hole transporting layer, perovskite absorber, electron transporting layer, and the metal or carbon electrode. Devices are produced on both rigid and flexible substrates and in p-i-n and n-i-p modes (figure 2.4).
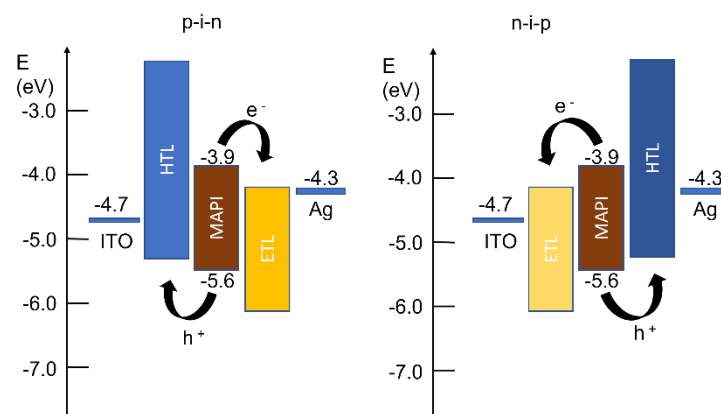
Figure 2.4 Band diagram of perovskite solar cell in p-i-n and n-i-p configuration.

Transport layers play a vital role in the process of charge extraction. Materials with the highest occupied molecular orbital (HOMO) level higher than the perovskite can be used as hole transporting layers (HTL). Many materials are currently used, including Spiro-OmeTAD, P3HT, NiO, CuO, CuI, Cu_2O, PTAA, PEDOT: PSS, or self-assembling monolayers.[55]–[57] Materials used for transporting electrons and blocking holes (ETL)

must have both HOMO and LUMO (Lowest unoccupied molecular orbital) levels lower than the ones of perovskite. Fullerenes and metal oxides like SnO_2, TiO_2, ZnO are widely used as ETLs[58]. Additionally, the layer on the side exposed to light must have a good transmission in the UV-Vis range.[59]

In some cases, an additional thin layer of insulating material (like bathocuproine) is included on top of ETL as a buffer protecting from metal penetration during electrode deposition (i.e. by thermal evaporation).

In perovskite solar cells, hole transport materials provide improved extraction of charges boosting operational performance, however, it is not an essential component. Recently, devices with simplified architecture without HTL were shown to be quite effective reaching an efficiency above 20%. [60]

2.4. Techniques used for PSC fabrication

Fabrication of PSC mostly relates to thin layer deposition processes. Over the years many techniques were developed for both perovskite and adjacent layers coating.[61] It was shown that the method and conditions of the deposition process affect the final photostability of perovskite, as it defines the layer morphology and concentration of defects. [62] Perovskite crystalline layer can be obtained by thermal evaporation of powdered precursors in the vacuum chamber or by wet chemistry processes where a precursor solution is spread on the substrate and crystallized upon drying. Both approaches have their advantages and drawbacks.

2.4.1.Vacuum deposition

The crystallization of perovskite from a gas phase is realized by the sublimation of precursor powders in a closed chamber under vacuum conditions (around 1×10^{-3} Pa). The substrate is placed on a rotating holder above the sources, so the gas can condensate on it and form desired material. The process can be realized in two ways, in a one-step process by simultaneous sublimation of two (or more) precursors, which adsorb on the surface of the substrate and react forming perovskite crystalline layer or by a two-step process, where PbI_2 is deposited first and the reaction occurs in a second step upon exposing it to methylammonium iodide vapours. [63] [64]

Vacuum deposition is a solvent-free process that does not require any post-treatment (drying) of the sample. The layer formed in this way is uniform and highly crystalline. The stoichiometry is defined by an evaporation rate controlled by a quartz crystal microbalance mounted inside the chamber. Usually, each precursor has one dedicated sensor. Due to the high vapour pressure of organohalide perovskites and the multidirectional flow of vapours, this method is not very precise and can give a misleading reading affecting the reproducibility of the process. It is also very sensitive to the precursor impurities, which can

change the sticking coefficient to a golden plate of the sensor. Apart from poor control over the perovskite composition, scalability and cost of the vacuum deposition process is also under debate. Further upgrades of the gas phase deposition processes are currently being developed. Varying the process parameters like pressure, the temperature of the substrate and the walls or presence of carrier gas affect the final layer quality.[65] More sophisticated tools like a laser, Atomic Layer Deposition(ALD), sputtering are being employed to make this process more efficient and reproducible.[66]–[69] However, up to now, perovskite solar cells featuring layers processed with these methods have not yet reached the same performance as their solution-processed counterparts. [70]

2.4.2.Solution processes

The term solution process relates to all the methods where precursor salts are dissolved and spread on a substrate in a liquid state. The crystallization occurs when the sample is exposed to drying allowing solvent evaporation. There are many techniques developed for perovskite precursor solution coating but the overall process can be divided into three stages: solution, deposition and crystallization. Each stage requires specific optimization and selection of conditions. The following sections will provide insights into important factors affecting each step.

- Solution

Perovskite precursor solutions have colloidal nature. The colloids are made of a lead polyhalide framework and can be structurally tuned by a coordination degree.[71] The Pb^{2+} cation as a Lewis acid can coordinate up to six ligands. All the Lewis base species (halide ions, organic groups, solvents) present in the solution compete with each other to bond to lead. The competition is ruled by their binding strength, thus the composition of a complex and degree of coordination vary upon changing the solution ingredients. The evolution of colloids can be evidenced by tracking their size (by Dynamic Light Scattering- DLS) or their coordination degree (by measuring UV-Vis absorption spectrum of solution). The changes in structure, size and concentration of colloids strongly affect the later crystallization of perovskite.[72] Tuning the coordination chemistry of a precursor solution is an important step in perovskite solar cell fabrication and apart from solution composition, it can be realized by solution ageing or conditioning. The first publication included in the experimental part of this thesis (*Green Solvent-Based Perovskite Precursor Development for Ink-Jet Printed Flexible Solar Cells*) concerns this matter for triple cation perovskite composition.

- Deposition

To form a uniform layer of perovskite, precursor solution has to be spread all over the substrate evenly. The most common technique used in the field is spin-coating. In this method, the solution is simply dropped on the sample and the spreading is realized by spinning the sample at a defined speed which directly affects the thickness of the obtained

layer. A schematic illustration of this method is presented in Figure 2.5a. Spin-coating provides a very even and fast distribution of solution leading to a uniform layer. The process is easy to manipulate and compatible with glove box conditions, thus it is very commonly used for the fabrication of high-efficiency perovskite solar cells. The drawback of this method is certainly low industrial potential due to high material waste and the limitation of a sample size.

Another method that is applied for bigger areas deposition is blade coating. In this method, the spreading is realized by a meniscus created between the blade and the substrate. The shoulder with a blade is moving across the substrate spreading the solution. A schematic illustration of this method is provided in Figure 2.5b. Blade coating is successfully applied for perovskite deposition on a larger scale, however, the material wastage is also high and difficult to recycle.
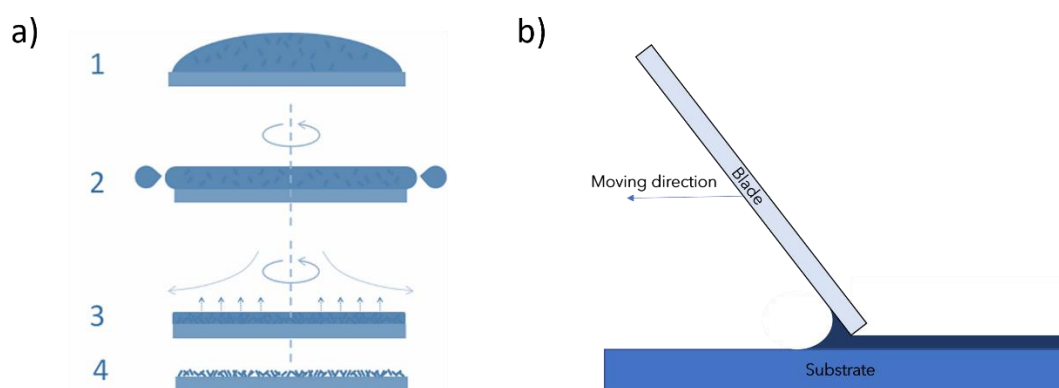

Figure 2.5 Schematic illustration of a spin coating process (a) and blade coating (b). The numbers indicate the order of steps.

The selection of a deposition technique is a key factor determining the process of perovskite solar cells production. Proper consideration needs to be given, to choose the technique that will allow sufficient coating of multiple layers. The deposition process impacts also the overall cost of the production influencing both operational costs and material usage efficiency. In the next chapter, the inkjet printing technique will be evaluated in a view of those constraints.

- Crystallization

The crucial part of perovskite solar cell fabrication is crystallization. The morphology of a crystalline layer is affecting solar cell performance immensely. Voids between the grains reduce the active area and impede the transport of carriers which results in diminished J_{SC}. Moreover, any pinholes in a film allow the contact between adjacent layers (HTL and ETL) which creates the paths of low resistance reducing the shunt resistance (R_{SH}), the $V_{OC,}$ and the fill factor.[72] The most important is to obtain a pinhole-free layer, but the size of the perovskite grains also affects cell performance. Bigger grains provide fewer grain boundaries, thus fewer recombination centres. Additionally, the stability of such a film is improved as the degradation of the perovskite film may proceed via surface defects.[73]

The crystallization process can be divided into two steps: nucleation and growth. Both steps are controlled by various, though related, sets of physicochemical parameters. The nuclei form when the solution reaches the supersaturation point. The nucleation process is ruled by the total Gibbs free energy change. When homogeneous nucleation takes place the nuclei form in the bulk of the solution and ΔG is the sum of the bulk (volume) free energy change (ΔG_V) and surface (interfacial) free energy change (ΔG_S) given by:

$$\Delta G = \Delta G_V + \Delta G_S = \frac{4}{3}\pi r^3 \Delta G_B + 4\pi r^2 \gamma$$

Where r is a radius of spherical nuclei, γ is the interfacial energy or the surface energy between the supersaturated solution and crystalline surface and the ΔG_B is the bulk free energy proportional to the logarithm of solution supersaturation ratio defined as C/C_S. Hence, at the supersaturation point, the ΔG_B becomes positive the sign of ΔG depends on whether the ΔG_S overcomes the ΔG_V. A critical nuclei radius r^* can be calculated for which the positive value of ΔG_S cancel out the negative value of ΔG_V so d(ΔG)/dr = 0. If the radius of nuclei is below the critical r^* value the nuclei will be re-dissolved and if it exceeds r^* it will be thermodynamically stable and can exist in the solution, able to grow further. The correlation between the free energy values and nuclei radius is illustrated in Figure 2.6.
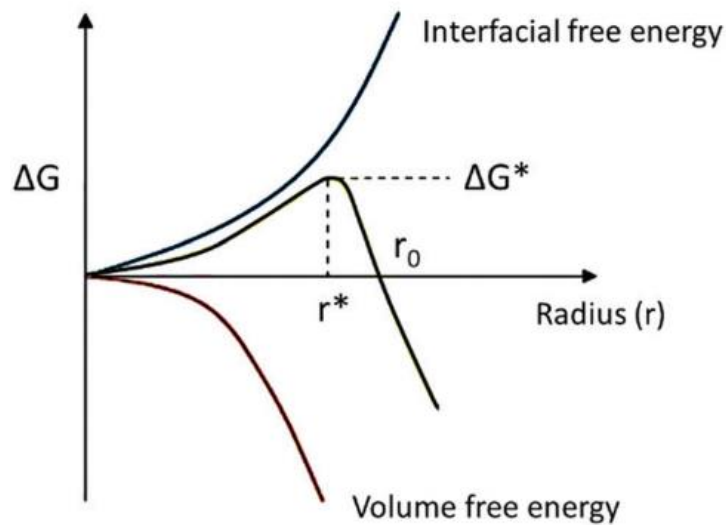
Figure 2.6 Free energy diagram indicating the existence of the critical radius value. Reprinted from [74] *with permission from the Royal Society of Chemistry*

In the classical theory of homogeneous crystallization further growth of nuclei leads to the formation of the crystals.[61] In the context of perovskite crystallization, it becomes clear that the aforementioned coordination reactions happening in the precursor solution influence the nucleation process, as the Pb-complexes can serve as nucleation centres. However, as we consider the formation of a layer on a solid substrate, surface energy plays an important role in the nucleation process as well. In this case, it is not homogeneous, but a heterogeneous process. The solid surface of the substrate assists in the process of phase transformation by decreasing the total free energy for forming a critical nucleus. According to Volmer's theory:

$$\Delta G^{het} = \varphi \Delta G^{homo}$$

$$\varphi = \frac{(2+cos\theta)(1-cos\theta)^2}{4},$$

where θ is the contact angle between the solution and the substrate. For contact angle 180° meaning no affinity between the phases, the free energy is equal to the free energy defined for homogeneous nucleation and the surface does not impact it. However, for lower contact angles when the solution spreads easily on the substrate surface the energy barrier is decreased, as the surface provides active centres for nucleation.[75]

Concerning the solution process of perovskite deposition, research has emphasized the need for nucleation control by doing both: tuning the colloid size (described in a previous section) and changing the surface energy of a substrate. The physical methods of surface activation are commonly used in the field and they will be described further in the following chapter. The nucleation can be also drastically changed by the chemical treatment of a surface including the seeding method. [76]

The successful implementation of a seeding layer strategy for inorganic perovskite growth developed within this work is included in an Experimental Part Chapter 7 as a patent application description.

The next stage, right after the formation of stable nuclei, is crystals growth. The growth is ruled by two processes being the diffusion of monomers to the surface and surface reactions. Thus factors like concentration gradient, temperature, gas flow can affect the speed of formation and the final morphology of crystals. The density of nuclei and the growth dynamics can be correlated with the size of the grains and the surface coverage (in case of a layer formation). It was shown for perovskite crystallization that the growth of crystals may be controlled by changing the drying conditions.[77] In this work, the impact of different drying conditions was evaluated for 2D perovskite crystallization, where the orientation of the grains is of great importance. The study is included in an Experimental Part Chapter 5 as a publication titled: *Inkjet printing of quasi-2D perovskite layers with optimized drying protocol for efficient solar cells*.

3. Inkjet printing technique

The concept of inkjet printing was originated in the second half of the nineteenth century by Lord Rayleigh and Lord Kelvin. In the 1970s and 1980s, the first inkjet printers were developed and utilized for products marking.[78] Since then technology advanced tremendously expanding the range of applications. While the most popular application of inkjet remains graphics and text printing for packaging, recently, it was found to be useful also in other fields like electronics, biotechnology and pharmacy.[79] Inkjet technique has shown great versatility turning out to be a useful tool for both research activities and industry. Inkjet printing is used for the deposition of different materials including paints, coatings, polymers, nanoparticles and conductive inks. It is a non-contact technique, thus the substrate can be either rigid or flexible. Printing is widely performed on paper but also on textiles and polymers.

The unifying feature in all these applications is inkjet's high precision. The printing is realized by forming a layer from a large number of individual drops, typically 10-100 um in diameter. This entails the other important feature which is the high accuracy of the placement of a drop enabling printing of detailed and sophisticated shapes. This technique allows printing the layer of a certain shape based on a pre-designed digital file, without a physical template, in contrast to the other conventional printing methods (e.g. lithography). The complex patterning in a single pass deposition is the main advantage over standard screen printing and photolithography. High control over drops ejection provides also the repeatability and the ease to tune the thickness by varying the drop volume and printing resolution. Additionally, it ensures low ink consumption as the ink is distributed only on the area specified by a digital pattern loaded to the machine software.

Cost-efficiency, ability to apply on a large scale and fast rate of deposition are the factors that make it an industrially viable tool. High control over the ejection process and precision of a drop placement allow using of inkjet printing already in the research and development stage of the process.

This thesis brings into consideration the application of inkjet printing for perovskite solar cells production, which is currently in an early stage of commercialization. To address this topic a fundamental understanding of inkjet printing technique, including the impact of the ink and substrate properties as well as printhead technology on printing quality has to be provided. Thus, in this chapter, the most important factors affecting the printing process will be described. The overall process characteristic can be illustrated by a so-called, magic triangle of inkjet printing and it is presented below (figure 3.1).
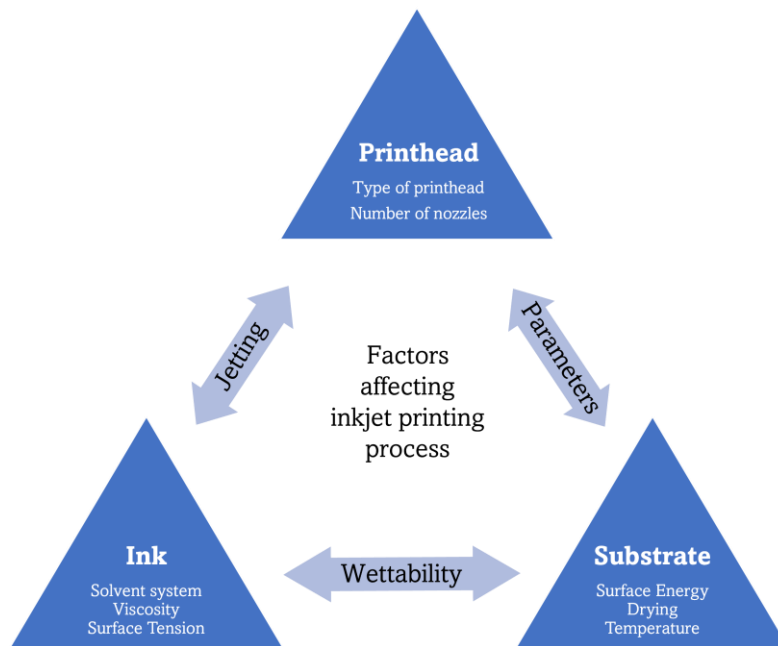
Figure 3.1 Relationships between printhead, ink and substrate used in the inkjet printing process (Magic triangle of inkjet)

As can be seen from Figure 3.1 the printing process is governed by printhead technology and physicochemical properties of the ink and the substrate. In later sections, the relationships between all three factors and their influence on printing quality will be described in details leading to a better understanding of the process complexity.

3.1.Types of printheads

There are two main categories of inkjet printing according to the mechanism of drop formation. In a so-called continuous inkjet (*CIJ*) the drops are created in a continuous stream whereas in a drop-on-demand (*DOD*) system the drop is ejected only if required. The general mechanism of drop ejection is pictured in Figure 3.2.

Figure 3.2 Schematic comparison between a) continuous inkjet system and b) Drop-on-demand inkjet system. [80]

In a continuous mode, a high-pressure pump directs the ink from the container to a nozzle where the constant vibration of the piezoelectric crystal causes the stream of liquid 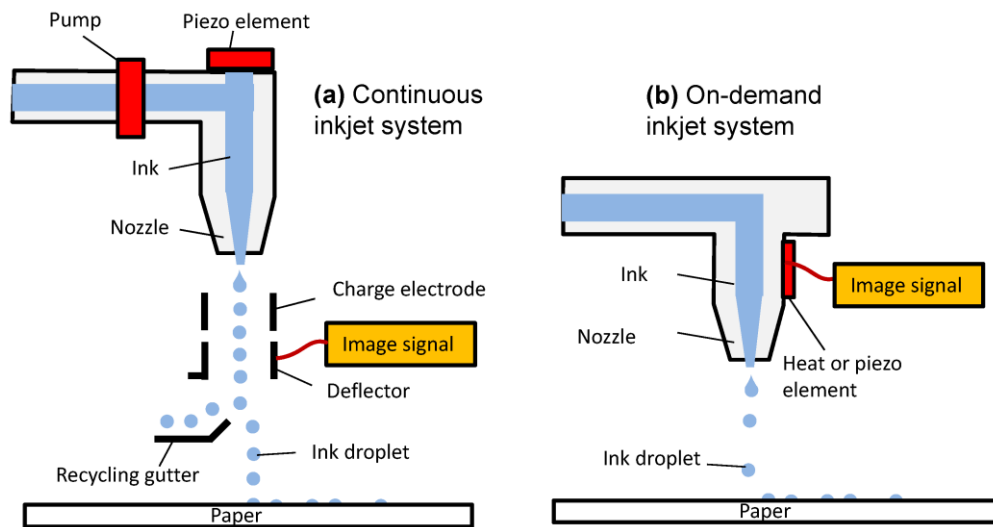to break into single drops. Then the electrostatic field is applied to deflect the drops and direct them to the substrate or the recirculation gutter. The ink from the gutter is directed back to the nozzle and reused. The pattern is created by switching the drops destination during the printing. Such an approach provides the ejection of high-velocity drops at high frequency (up to 100kHz) which might be desired for mass production processes. Additionally, as the nozzle is working continuously it doesn't tend to clog. Apart from its advantages, continuous inkjet printheads have also few inconveniences compared to *DOD* systems. During the recirculation, the ink is exposed to the environment which may cause some changes in the ink composition induced by the contamination or partial evaporation. Also, a bigger volume of the ink is required to feed the machine as most of the ink fills a recirculation channel. The fact that the drops are steered by electrostatic field limit the choice of ink which is restricted to electrically conductive materials.[78]

DOD systems might be divided further into two main categories depending on the method of pulse generation for drop ejection: thermal or piezoelectric.

Thermal DOD inkjet printing, also known as a bubble jet, uses the thermal expansion of the ink to generate the pressure pulse. Each nozzle is equipped with a resistor element, which receives a current signal and warms up the ink. As the ink vaporizes, a small bubble is created increasing the pressure inside the nozzle propelling the drop towards the substrate. This method is commonly used in desktop printers, but its industrial application is limited due to the ink restrictions of having a volatile component and materials resistant to high temperatures (reaching 300°C).[78]

In the piezoelectric inkjet printheads, the drops are generated by a piezoelectric actuator. In the most common system the ejection is realized by wall distortion. In this case the channel is built from (or contains a layer of) a piezoelectric material, which receives an electric signal and change the shape accordingly. The movement of the walls generates the

pressure wave which ejects the drop from the nozzle. In the first stage the channel expands pulling the ink from a reservoir refilling the nozzle, then the walls contract squeezing the liquid in between the channels causing the release of a drop. A simple schematic of a wall distortion is shown in Figure 3.3.
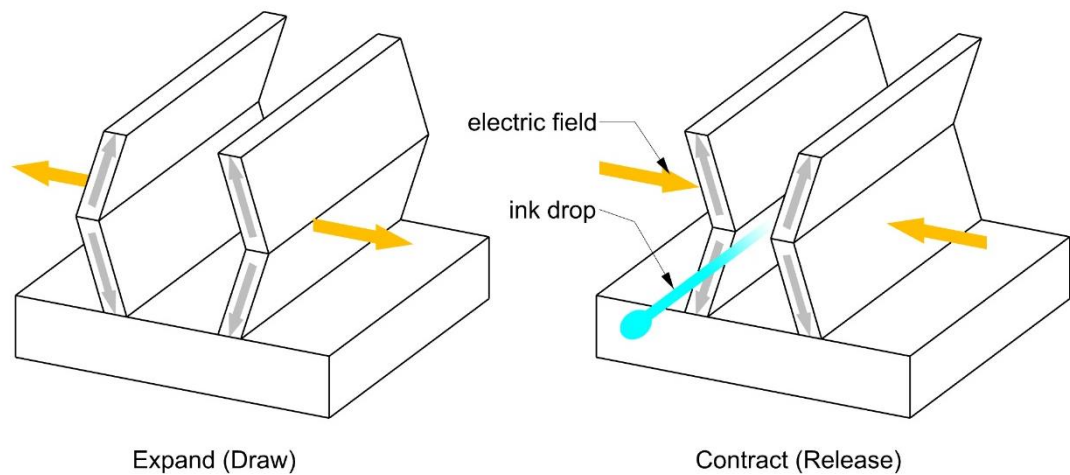

Figure 3.3 Schematic of a wall distortion by an electric pulse in a piezoelectric inkjet printhead

The sequence of electrical pulses, with the corresponding timescale, which drives the piezoelectric printhead is called a waveform. Usually, a sequence of pulses with opposite directions is required to enhance the ejection efficiency by pressure wave resonance. The amplitude and the width of pulses composing the waveform have a direct influence on drop volume and velocity. As the rheological properties of the fluids affect their behaviour in the nozzle, a specific waveform has to be designed for each ink. The goal is to obtain uniform and stable jetting along the whole printhead with the drops of desired volume and speed.[81]

The piezoelectric inkjet technology can be used for a wider range of inks and it does not require high temperatures to vaporise the ink as thermal inkjet printing, thus it was used in the research presented in this thesis.

The geometry of the channels and used construction material can affect the drop ejection, thus each printhead has a specified range of ink properties. Also, compatibility with the ink should be taken into account while choosing the printhead, especially for organic solvents. There are currently few manufacturers on the market providing systems made of different materials for certain applications. The number of nozzles in the printhead can vary according to the need. Researchers might use single nozzle setups for studying the drop formation, while the industry aims for high-speed deposition with printheads with up to few thousands nozzles. [81]

3.2.Ink

As it was mentioned before, a wide range of materials can be subjected to inkjet printing. The inks used in inkjet printing technology can be divided into three groups: water-based inks, solvent-based inks and reactive ink (usually UV-curable polymers or resins). All of them needs to meet printhead criteria defined by viscosity, surface tension and density.

3.2.1.Viscosity

Viscosity is a measure of fluid's resistance to deformation at a given rate. In other words, it describes the fluid ability to flow, thus it is one of the most important properties of the ink. Too viscous inks require high pressure to be ejected from a nozzle. When the viscosity of the ink is too low the main drop will be followed by a small satellite, which can cause drop misplacement or alter the resolution of the printout. The optimum value has to be found to allow proper drop formation. Viscosity is sometimes correlated with the volatility of the ink. Those two properties are usually going against each other, so the trade-off between them needs to be found to provide good jetting and drying. Viscous inks are usually made of materials with high molecular weight or having strong intermolecular bonds, thus having low vapour pressure, which can prolong drying. As opposed to this, if the ink is made of low molecular weight material it has low viscosity, but high vapour pressure, which evaporates quickly. To obtain an optimum ink property, solvents of different characteristics can be mixed, although possible interactions need to be considered. In the case of perovskite printing, the difference of volatility between the solvents composing the ink can have a big impact on crystallization dynamics. Evaporation of one component may change the structure of the perovskite intermediate phase affecting the final morphology and crystallinity, which was observed for the widely used DMF: DMSO mixture.[82]

The viscosity is highly dependent on the temperature, thus some fine-tuning can be done by controlling printhead temperature. However, not all the printheads are equipped with a heating system and rising temperature can affect ink's stability.

Most of the inkjet systems have an operating viscosity window of 3-40 mPa·s and 10-20 mPa·s for *DOD* systems.[78]

3.2.2.Surface tension

The surface tension of the ink reflects the physical phenomenon that the atoms on the surface of the liquid have higher energy than the ones in the bulk. The energetical asymmetry implies that to create a new surface area, some energy needs to be delivered. This energy is proportional to the size of the area and it is measured in J/m^2 or N/m.[83] The difference between the energy of molecules on the surface and in the bulk originates from the intermolecular bonds thus it is correlated with viscosity. To divide a liquid continuum into small drops, some external force needs to be delivered. In DOD systems it is provided by applying a mechanical pressure of the channel and in CIJ by an electric field.

In piezoelectric DOD printheads, the higher surface tension and viscosity the higher voltage pulse have to be applied to eject the drop. Once the drop is ejected it will form a spherical shape to reach the energy minimum and create the smallest surface for a given volume.[78]

Adjustment of surface tension for a given ink can be realized by the addition of surfactants and it is a common strategy for water-based inks. There is a wide range of materials available on the market which can efficiently change the surface tension of the ink, however possible interactions with the ink and impact on final layer properties have to be considered.

Surface tension is also affecting the spreading of the ink on the substrate, which will be discussed further in a later section of this chapter.

3.2.3.Density

Density is a measure of solid content in a liquid volume. The value of density is affecting the drop formation, as there is a change in kinetic energy upon increasing solid concentration in the solution. Modification of density cause also a change in the acoustic speed inside the fluid, so the kinetics of wave propagation. For each change in density the shape of the waveform in the piezoelectric printhead has to be adjusted. Higher density implies a higher pulse required for drop ejection. [84]

3.2.4.Vapour pressure

Vapour pressure is a physical measure of volatility. As it was mentioned above, usually it is inversely proportional to the viscosity of a given ink. Vapour pressure of the ink is an important parameter, which affects the process of inkjet printing. For *DOD* piezoelectric systems the most crucial is its effect on ink drying behaviour. The drying dynamics affects not only the post-treatment process of the printed layer but also the jettability. Too volatile inks tend to dry at the nozzle orifice causing clogging. Solute accumulated on the nozzle plate can cause problems with the reproducibility and reliability of a printing process.

3.2.5.Jettability

All described above properties affect the jetting behaviour of the inkjet printhead. To find a direct relation between the ink rheological parameters and its jettability, a few dimensionless numbers were proposed.[85] Those numbers are describing the ratios between general forces acting on the fluid.

The Reynolds number (Re) describes the ratio between the inertial to viscous forces:

$$Re = \frac{\rho l^2 v^2}{\eta l v} = \frac{\rho l v}{\eta}$$

,where ρ -density [kg/m³], l-nozzle diameter[m], v-liquid velocity [m/s], η- dynamic viscosity [Pa·s]

The Weber number (We) is the ratio between inertial and cohesion force :

$$We = \frac{\rho l^2 v^2}{\eta l} = \frac{\rho l v^2}{\eta}$$

The Ohnesorge number (Oh) which relates the viscous to cohesion and inertial force:

$$Oh = \frac{\eta l v}{\sqrt{\rho \eta l}} \sim \frac{\sqrt{We}}{Re}$$

In inkjet printing the inverse of Ohnesorge number is often used and it is called a Z number:

$$Z = \frac{1}{Oh}$$

It is found that for DOD printheads a Z number has to be greater than 2 to enable stable jetting. The drop volume will increase with increasing of Z (for constant pulse voltage).[85] Another study says that there is also an upper limit when viscosity is too low and specify the printability range to 1<Z<10.[86] Another common procedure is to look at the graph illustrating the correlation between We and Re numbers (shown in Figure 3.4)
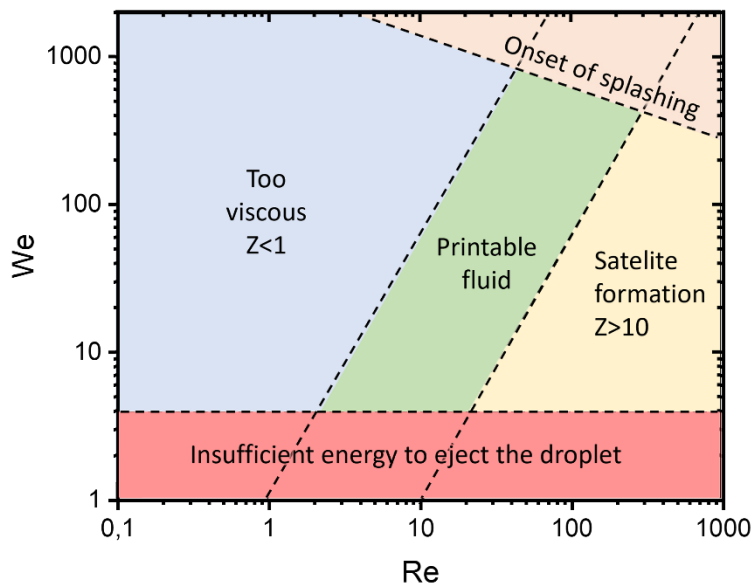

Figure 3.4 Printability defined by Weber (We) and Reynolds (Re) numbers [87]

Defining the dimensionless numbers allows simulating the ink behaviour in the printhead based on the simple rheological characterization. It can be used as a preliminary analysis to predict the behaviour of a new ink composition reducing the cost of further experimental

study. Once the rheology of the ink is in the printability range, the ink-substrate interaction should be studied.

3.3.Substrate
3.3.1.Wetting

Inkjet printing is a contactless technique, thus it can be performed on a wide range of substrates and the ejection of the drops is not affected by a change in the substrate material. However, once the drop is released, the ink-substrate interaction plays an important role in affecting the printing outcome. We can divide this process into two stages: firstly, the drop hits the substrate- this step is influenced mostly by drop velocity, size and inks' rheological parameters; then the drops are spreading radially outwards until they reach equilibrium. Properties like roughness, hydrophobicity, chemical character of the surface influence the spreading of drops and further layer formation. We can use the term wettability to describe a general behaviour of a drop on the substrate. The most common approach to characterize wetting is to measure the angle between the drop surface and the substrate. The physical foundation of a contact angle measurement lies in a Young equation:

$$cos\theta = \frac{\sigma_{SF} - \sigma_{SL}}{\sigma_{LF}}$$

Where σ is a surface tension on different interfaces, namely solid-fluid (SF), solid-liquid (SL) and liquid-fluid (LF), where fluid is the air and liquid is the ink.

The relation between the contact angle and wetting behaviour is illustrated in Figure 3.5.
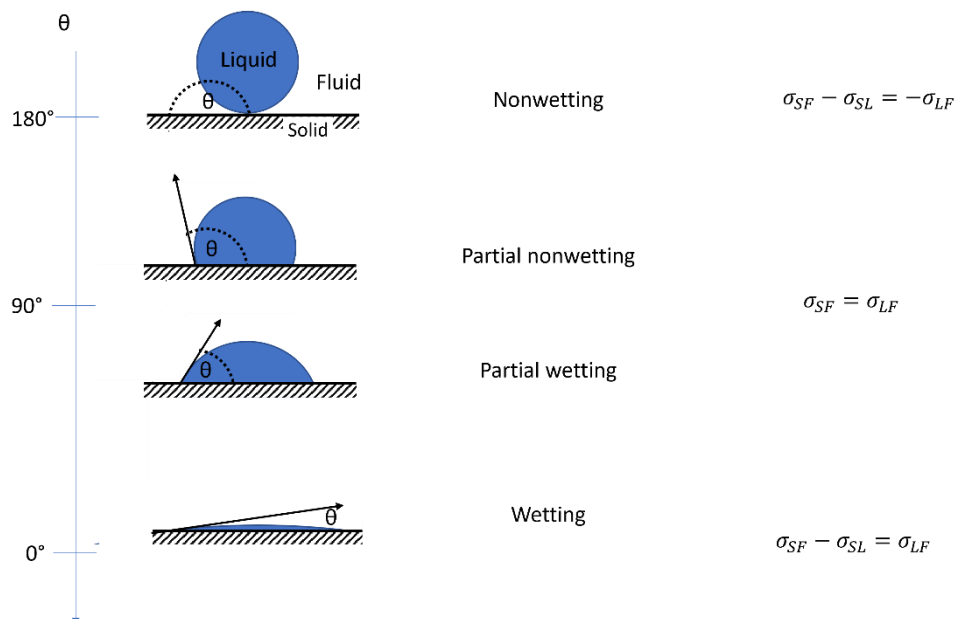

Figure 3.5. Graphical representation of wetting behaviours according to the contact angle θ

The Young equation assumes that the surface of the solid is perfectly smooth. From the processing point of view, it is important to evaluate the ink spreading on a real substrate during printing. The rough surface of the same material will show a greater contact angle leading to poor wetting. The desired behaviour is when the drop once placed on the substrate remains there (especially important for high precision detailed printing), and collapse with adjacent drops forming a uniform layer. Too good wetting can cause overspreading and deformation of the pattern and if the wetting is bad, the drops will not form a continuous layer but lines or single drops. Figure 3.6 illustrates the examples of both cases.
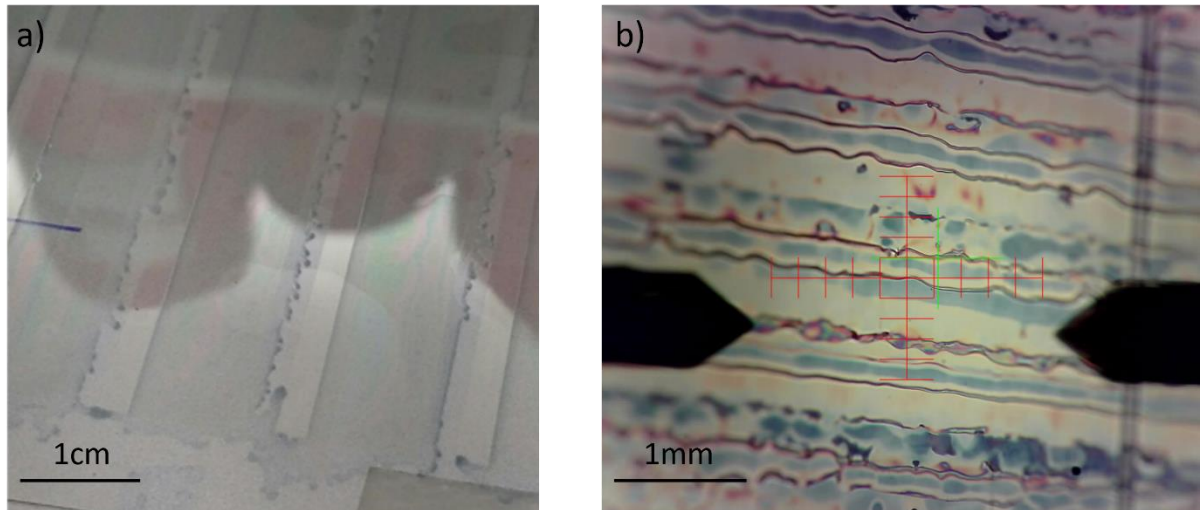
Figure 3.6 Polymer dispersion printed on PET/ITO foil showing overspreading(a) and bad wetting leading to not-continuous layer (b)

3.3.2.Substrate activation methods

The wettability of the surface can be adjusted by changing its surface free energy. It can be done either by chemical coating, physical treatment, or a combination of both. [88]–[91] All those methods act to add or modify the functional groups on the surface of the material. Chemical methods include simple coating materials or oxidizing agents. The chemical coating is widely applied for photos printing, where the surface of a paper is covered by an additional layer providing proper wetting and a good pigment appearance. It is an effective way of changing the surface energy, however, it is not sufficient for complex applications, like printed electronics, where additional layers may affect the final product performance. Physical activation methods are considered to be more reliable and more environmentally friendly as the use of hazardous solvents can be avoided.[92][93] Physical activations include Ultraviolet light (UV), corona, plasma, laser, X-ray treatment.[94] It is important to choose the method specifically for a given substrate and ink to activate the surface without causing any damage or change of its mechanical properties.

The most common method of surface activation is plasma treatment. In this method a gas (usually oxygen, nitrogen, argon) is ionised to turn into a mix of charged particles,

molecules, excited atoms, radicals and UV photons which interact with the substrate surface incorporating functional groups. The process can be done under a vacuum or at atmospheric pressure. This method is relatively gentle and provides a long-lasting effect, thus it is used in many fields including sensitive biodegradable polymers.[95] The effect of plasma can be adjusted by changing the gas, pressure and power of the source.

Depending on the gas and material the mechanism of activation can be slightly different. Charged gas molecules can build in the polymer creating new functional groups or oxidizing the existing ones on the surface modifying the properties and morphology of the material.[96] Plasma can be also used for dry cleaning, to remove organic impurities by breaking C-H bonds by ion bombarding. [97]

In the field of thin photovoltaics, also UV is widely applied. Especially the technique called UV-O_3 which combines two UV lamps with 184.9 nm and 253.7 nm spectrum wavelength. The first lamp (184.9 nm) radiates the oxygen from the air causing the formation of ozone in the following reactions:

$$O_2 \rightarrow O + O$$

$$O + O_2 \rightarrow O_3$$
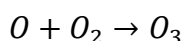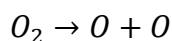
Then, the rays with 253.7 nm irradiate the ozone which breaks back into oxygen and highly energetic radicals. Those radicals created in both processes are effective in impurities removal and breaking the bonds of functional groups on the substrate surface [98]. Overall, the surface free energy is changed. The UV-O_3 method is less aggressive and the effect is not lasting as long as in the case of plasma, but both methods are suitable for substrate cleaning and activation before inkjet printing.

Surface free energy can also vary upon a temperature change and it is known as the Marangoni effect.[99] When the temperature rise, both viscosity and surface tension change. The spreading on the warm substrate can be also suppressed by fast evaporation of solvent induced by temperature rise. In some processes, a simple substrate pre-heating method is sufficient to provide optimum layer formation. In the case of reactive inks (like perovskite precursor printing), using this method strongly affects the reaction kinetics, thus it has to be studied carefully. For some perovskite compositions, the pre-heating method was shown to be beneficial, however, it needs to be adjusted for a specific perovskite composition, solvent system and deposition method.[100][101] Inkjet printers are usually equipped with a heating system for a printing table, so this method is viable to apply in industrial processes.

4. Inkjet printing of mixed cation perovskite

Green Solvent-Based Perovskite Precursor Development for Ink-Jet Printed Flexible Solar Cells, Wilk, B., Öz S., Radicchi E., Ünlü F., Ahmad T., Herman A.P., Nunzi F., Mathur S., Kudrawiec R., Wojciechowski K., ACS Sus. Chem. Eng. 2021, 9 (10), 3920-3930

DOI: 10.1021/acssuschemeng.0c09208 Impact factor: 7.8

Barbara Wilk contribution:

- Ink composition optimization: literature search for finding proper solvents; initial solubility trials and rheological analysis (not included in the final manuscript);
- Characterization: inks analysis including DLS, UV-Vis, rheological parameters measurement; X-ray Diffraction and Scanning Electron Microscope analysis of perovskite layers;
- Optimization of the printing process: waveform design; printing parameters adjustment; finding proper crystallization conditions and substrate surface activation method. Optimization of layers thicknesses;
- Solar cell fabrication: substrates preparation, electrode etching and coating of other layers building a full perovskite solar cell (spin-coating of PEDOT:PSS , thermal evaporation of C_{60}, bathocuproine and silver electrode) and I-V measurement of devices;
- Experiments design, data analysis and communication with collaborators (sending samples for external analysis and discussion about Density Functional Theory calculations results);
- Manuscript writing.

Research Article

Green Solvent-Based Perovskite Precursor Development for Ink-Jet Printed Flexible Solar Cells

Barbara Wilk, Senol Öz, Eros Radicchi, Feray Ünlü, Taimoor Ahmad, Artur P. Herman, Francesca Nunzi, Sanjay Mathur, Robert Kudrawiec, and Konrad Wojciechowski*

Cite This: https://dx.doi.org/10.1021/acssuschemeng.0c09208   Read Online

ACCESS | 📊 Metrics & More | 📰 Article Recommendations | 🆂🅸 Supporting Information

ABSTRACT: Within a decade, perovskite solar cells (PSCs) leaped to the forefront of photovoltaic research, rapidly moving toward the industrial phase. Despite the impressive progress in technology development and new efficiency records, there still remains a large scope for further advancement. Utilization of scalable deposition methods and good control of the perovskite crystallization process, especially with industrially compatible fabrication protocols, require more understanding to ascertain reproducible, large-format manufacturing. Here, we report ink formulation development for ink-jet printing of perovskite thin films in ambient conditions. We used the precursor solution on a nonhazardous solvent system, fulfilling industrial requirements. By carefully adjusting the coordination environment of the Pb^{2+} through additive engineering, we were able to tune the nucleation process and achieve uniform, pinhole-free perovskite thin films. Furthermore, we combined multiple characterization techniques with computational methods to analyze Pb-complex structures and evaluate their influence on perovskite formation. Lastly, we applied ink-jet printed photoactive layers into large-area (1 cm^2) photovoltaic devices and processed on flexible substrates (PET foil). Inverted (p−i−n architecture) PSCs, based on multication composition, $Cs_{0.1}[(HC(NH_2)_2)_{0.83}(CH_3NH_3)_{0.17}]_{0.9}Pb(I_{0.83}Br_{0.17})_3$, delivered 11.4% of power conversion efficiency.

KEYWORDS: perovskite solar cells, ink-jet printing, non-hazardous solvents, ambient processing
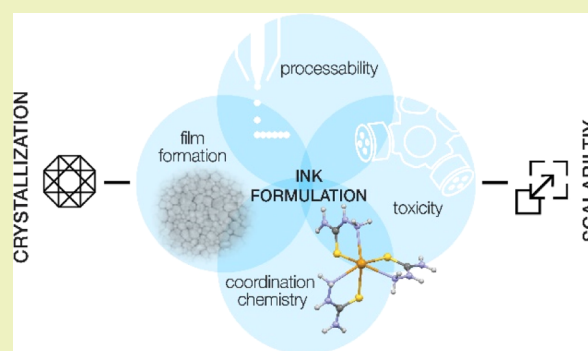
INTRODUCTION

In recent years, perovskite solar cells (PSCs) have emerged as one of the most promising next-generation photovoltaic technologies. High power conversion efficiency (PCE), reaching 25.5%, is attributed to outstanding properties of hybrid perovskites, such as strong optical absorption, low exciton binding energy, long free-carrier diffusion length, and ambipolar charge transport.[1−5] Polycrystalline perovskite films can be obtained by relatively simple and low-cost solution processes, which enables the utilization of flexible, polymeric substrates. This equips PSCs with new value propositions, making them attractive for the emerging and rapidly growing PV markets, such as building-integrated PV, automotive, or internet-of-things.[6,7] However, precursor solutions used for processing perovskite layers are typically based on highly toxic solvents, which have limited potential for industrial usage.[8]

The state-of-the-art perovskite photoactive layer composition is based on a mixture of monovalent cations at the A-site of the ABX$_3$ formula, namely, methylammonium, formamidinium, and cesium.[9] Several attempts have been made to dissolve different perovskite components in nonhazardous solvents, but there are very few reports of such formulations made for mixed-cation perovskite compositions.[10−14] Further-

more, the highest efficiencies are typically reported for the cells prepared in an inert atmosphere by a nonscalable spin-coating technique, with a solvent quenching approach.[15] There are still significant research efforts required to establish industrially feasible manufacturing methods. Challenges in scaling up PSCs include developing deposition protocols for uniform coating of photoactive layers over large-area substrates. Thus, good understanding of the precursor chemistry is needed to be able to control film formation dynamics.

One of the techniques that can be very attractive for the large-scale production of perovskite photovoltaic devices is ink-jet printing. This coating method has been widely applied in the field of printed electronics, primarily due to its high precision combined with low operational expenditure. Utilization of ink-jet printing for perovskite deposition provides not only excellent control over target layer thickness

but also enables seamless access to various customized shapes and geometries.[16] The development of ink-jet printing for perovskite deposition was initiated in 2014 by Wei et al.[17] Since then, the technique has attracted considerable interest as a coating method for active layers in a PSC stack.[18−21] Recently, outstanding results were reported by Eggers et al., where ink-jet printed PSCs demonstrated a PCE close to 21%.[22] However, printhead compatible, nonhazardous ink formulations have not been reported yet.

It is widely accepted that perovskite precursor solution chemistry strongly affects crystallization dynamics.[23] The mechanism of perovskite crystal formation is highly dependent on colloidal precursor solution, rich in PbX_n complexes.[24,25] The colloids can act as nucleation centers, organizing on the substrate and forming solid intermediate phases.[26,27] Their structure and stability can define the size and optoelectronic quality of ensuing perovskite grains.[28,29] Stable intermediate phases are often formed by utilizing Lewis acid−base interactions, which allow control of the crystal growth dynamics.[30] It also helps to stabilize the crystallization process in ambient conditions, where water molecules can coordinate to precursor structures, leading to undesired byproducts.[30] Understanding of the complex coordination chemistry occurring in perovskite precursor solutions is still limited. For each specific deposition strategy, an interplay between solvents, perovskite components, additives, and film formation dynamics needs to be resolved and optimized.

Here, we demonstrate ink formulation development, based on nontoxic solvents, for the ink-jet printing process of perovskite thin films. To carry out this process in ambient conditions, we incorporate the highly coordinating Lewis base additive, thiosemicarbazide (TSC), to the precursor solution, to form a stable intermediate phase of Pb complexes. We modulate the TSC structure with an acid additive to enable desired Pb complexation in the solution, which in turn leads to the crystallization of the pure perovskite phase. We provide detailed spectroscopic characterizations to elucidate the mechanism of interactions occurring in the solution, which we further corroborate with computational modeling. The optimized ink formulation results in over 11% of PCE, obtained for large-area, flexible PSCs, produced by ink-jet printing.

■ EXPERIMENTAL AND THEORETICAL SECTION

Materials. Lead acetate (99%, anhydrous), lead bromide (98%), cesium iodide (99.9%), TSC (99%), formic acid (FAc) (95 wt % aqueous), bathocuproine (BCP, 99.99%), γ-butyrolactone (GBL, ≥99%), 2-methylpyrazine (2MP, ≥99%), and dimethylsulfoxide (DMSO, ≥99%) were purchased from Sigma-Aldrich and used without further purification. Other materials used are poly(3,4-ethylenedioxythiophene) polystyrene sulfonate (PEDOT:PSS, Al4083, Heraeus), lead iodide (99.9985%, Alfa Aesar), formamidinium iodide (99.99%, Dyenamo), and methylammonium bromide (synthesized in house, following the previously reported method[31]).

Device Fabrication. 15 Ω/sq poly(ethylene terephthalate)/indium zinc oxide (PET/IZO) foil, purchased from Eastman, was applied as a substrate. The foil was cut manually, etched by dip etching in 15 wt % HCl, and cleaned by isopropanol rinsing, followed by 2 min N_2 plasma cleaning. For the hole transporting layer, we applied PEDOT:PSS dispersion (Al4083) modified with the lead acetate additive; as such, lead acetate was added to PEDOT:PSS solution to reach 5 mg/mL concentration and was stirred overnight. The modification was previously reported by Zhang et al. as a mean to improve characteristics of the hole extraction interface.[32] The layers were deposited by spin-coating in the air for 45 s, at 4500 rpm,

followed by annealing at 100 °C for 25 min. Perovskite precursor solution of 30 wt % concentration was prepared by dissolving formamidinium iodide, methylammonium bromide, lead bromide, and lead iodide in molar ratios of 0.8:0.17:0.18:1 and in GBL/2MP/DMSO 9.5:4.15:1 vol ratio, where DMSO stands for 1.2 M stock solution of CsI. TSC was added in a molar ratio of Pb/TSC 1:0.18. FAc was added in the last step, in a molar ratio of TSC/FAc 1:8. For the TSC preconditioning method, the amount of TSC was kept the same but it was first dissolved in the GBL and 2MP mixture (the same volume ratio as in the ink); then, FAc was added in a reduced amount (TSC/FAc 1:2.65), and the mix was stirred for 1 h at 80 °C before incorporation to the perovskite precursor. Subsequently, perovskite layers were printed using an LP50 PiXDRO ink-jet printer. The process was carried out in the air, at room temperature, with relative humidity at alevel of 20−25%. Printed wet films were dried by N_2 gas for 2 min, followed by 12 min of annealing at 100 °C in the oven. For the electron transporting layer, 30 nm of C_{60} was deposited by thermal evaporation at ∼10^{-6} mbar. In the last step, 6 nm thick buffer layer of BCP and 100 nm of Ag were thermally evaporated via a shadow mask as a back contact.

Characterization. Dynamic light scattering (DLS) spectra were obtained using Malvern Zetasizer.

Scanning electron microscopy (SEM) images were obtained using a Phenom Pro-X microscope.

X-ray diffraction (XRD) patterns were obtained using a Rigaku MiniFlex diffractometer.

For the steady-state photoluminescence (ss-PL) experiments, the samples were excited by a continuous wave laser at $E_{exc} \approx 2.33$ eV (532 nm) and a power density of 0.3 W cm^{-2}. The resulting spectra were recorded using a thermoelectrically cooled Si CCD spectrometer (Avantes AvaSpecHERO HSC1024 × 58TEC-EVO, integration time 3 s, slit width 50 μm).

Nuclear magnetic resonance (NMR) spectra were obtained on a Bruker AVANCE II 300 spectrometer. The chemical shifts for ^{1}H NMR (300.1 MHz) are given in parts per million (ppm), referenced to tetramethylsilane. The chemical shifts for ^{207}Pb NMR (62.9 MHz) were referenced externally to a solution of 1.0 M $Pb(NO_3)_2$ in D_2O (δ = −2986.3 ppm) and are reported relative to $Pb(CH_3)_4$ in toluene (δ = 0 ppm). Measurements were conducted at 25 °C. Solutions for the NMR measurements were prepared freshly in a nitrogen-filled glovebox. Lead iodide (320 mg), TSC (20 mg), and FAc (67 μL) were dissolved in 1 mL of deuterated solvent (DMSO-d_6). For the mixture of all components, 320 mg of PbI_2, 11 mg of TSC, and 37 μL of FAc were mixed in 1 mL of DMSO-d_6. The solutions were stirred at room temperature until a clear solution was obtained. After that, they were filled into a glass NMR tube.

The current−voltage ($J-V$) characteristics of perovskite devices were recorded under ambient conditions, with a digital source measurement unit (Keithley model 2461), under simulated AM 1.5G irradiation (100 mW cm^{-2}), using an AAA-rated solar simulator (Abet Technologies, sun 2000), calibrated against an RR-208-KG5 silicon reference cell (Abet Technologies). A photoactive area of 1.0 cm^2 was defined for the solar cells using a shadow mask. The bias voltage was swept in both directions (from short-circuit to forward bias and back), at a speed of 100 mV s^{-1}.

UV−vis absorption spectra were obtained using the Edinburgh Instruments Spectrofluorometer FS5. For these measurements, the stock solution of PbI_2 in GBL (0.003 M) was prepared, and TSC and FAc (95 wt % aq Sigma-Aldrich) were added in PbI_2/TSC 1:1, PbI_2/FAc 2:1, and PbI_2/TSC/FAc 1:1:1 M ratios. For UV−vis analysis of TSC, 0.67 mg/mL solutions of TSC in GBL were prepared and aged in ambient conditions. FAc was added in TSC/FAc 1:8 and 1:4 M ratios for standard and preconditioning methods, respectively.

Theoretical Methods. Structural optimization of molecular complexes were performed with density functional theory (DFT) using the Gaussian 09 software package,[33] employing the 6-31G* basis sets for C, H, N, O, and S atoms, the LANL2DZ basis sets together with the LANL2 pseudopotentials for Pb and I atoms, B3LYP as the exchange−correlation functional,[34,35] and polarizable continuum model[36] as the implicit solvation model.
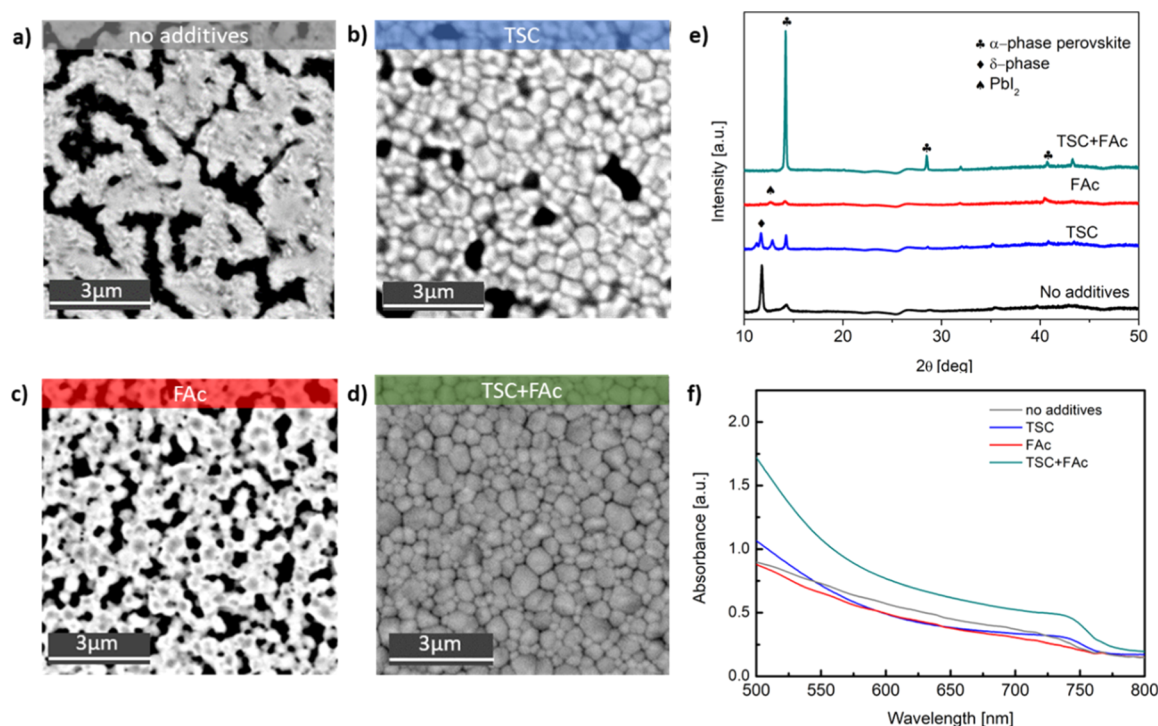
Figure 1. SEM images of perovskite thin films inkjet-printed from different ink formulations: (a) without additives, (b) with TSC additive, (c) with FAc additive, (d) with TSC and FAc additives; (e) XRD patterns and (f) UV−vis absorption spectrum corresponding to each printed layer.

RESULTS AND DISCUSSION

To formulate perovskite precursor ink composition based on mixed cations and nontoxic solvents, suitable for ink-jet printing in ambient conditions, we shortlisted solvents that could be potentially used. The choice of solvents affects the solution properties in many ways. In order to obtain the desired drop formation and continuous jetting, the ink must fit into viscosity, surface tension, and density range specified for the respective printhead. Additionally, the drying rate of the ink needs to be adjusted, not only for optimal perovskite crystallization but also to avoid nozzle clogging. Considering all these requirements, we selected GBL, which is one of the least hazardous solvent candidates with a high boiling point (T_B = 204 °C), suitable for ink-jet printing, and 2MP (T_B = 135 °C). In order to solubilize all the perovskite components, we also added DMSO (T_B = 189 °C) to the solvent mixture. We optimized the solvent ratios to obtain desired rheological properties, arriving with the following composition: GBL/2MP/DMSO 9.5:4.15:1 vol. After choosing the right solvent mixture, we composed 30 wt % of precursor ink, making up $Cs_{0.1}[(HC(NH_2)_2)_{0.83}(CH_3NH_3)_{0.17}]_{0.9}Pb(I_{0.83}Br_{0.17})_3$ perovskite composition, and adjusted printing parameters (including waveform optimization) to achieve continuous and stable jetting (see Figure S1, Supporting Information). Another fundamental property, which needs to be considered for a reliable printing process, is the substrate's surface energy, which must be higher than ink's surface tension to enable good spreading and subsequent layer formation.

In this study, we focused on flexible substrates, based on PET foil coated with IZO. We applied the p−i−n device architecture, with PEDOT:PSS used as a hole transport material. The contact angle was measured by forming a drop of perovskite ink on top of the PET/IZO/PEDOT:PSS substrate. We measured values below 5°, as we are showing in Figure S2,

Supporting Information. The surface did not require any pretreatment in order to be well covered. For the printing process, we used a semi-industrial LP50 ink-jet printer, equipped with a commercial printhead. The process was carried out at room temperature, in the air with a controlled relative humidity of 25%. In order to form perovskite polycrystalline films, we applied a postprinting drying step with nitrogen gas, followed by annealing in an oven at 100 °C.[37] At first, SEM images of the films obtained from the ternary solvent system ink showed a poor morphology and nonuniform coverage (Figure 1a). The XRD pattern of the layer indicates the favored formation of a hexagonal, nonperovskite δ-phase (Figure 1e).[38,39] In order to fabricate compact and uniform perovskite layers in ambient conditions, we applied the strategy of retarded crystallization by forming a semi-stable intermediate phase.[40] Formation of such preperovskite phases during the crystallization process was reported to be beneficial for obtaining uniform morphologies, with complete surface coverage.[41,42] This approach is based on the fact that lead iodide can be coordinated by electron-donating groups, forming Lewis acid−Lewis base adducts.[43] In a perovskite precursor solution, Pb^{2+} ions can be coordinated by I^- ions, creating iodoplumbate complexes with the general formula $[PbI_x]^{2-x}$, and by solvents containing electronegative polar groups, such as C=O or S=O, creating PbI_2−solvent or MAI−PbI_2−solvent complexes.[44,45] Perovskite formation is suspended until solvent molecules are released during annealing. The stability of such complexes is defined by the strength of the dative bonds created between the acceptor and donor. The higher the electron-donating strength of the donor ligand, the stronger the resulting bonding, thus more the stable complex and longer the crystallization process of perovskite grains. By slowing down the crystallization, more time is gained for effective post-treatment before undesired phases would start forming.[30,46] This way, enhanced control over the
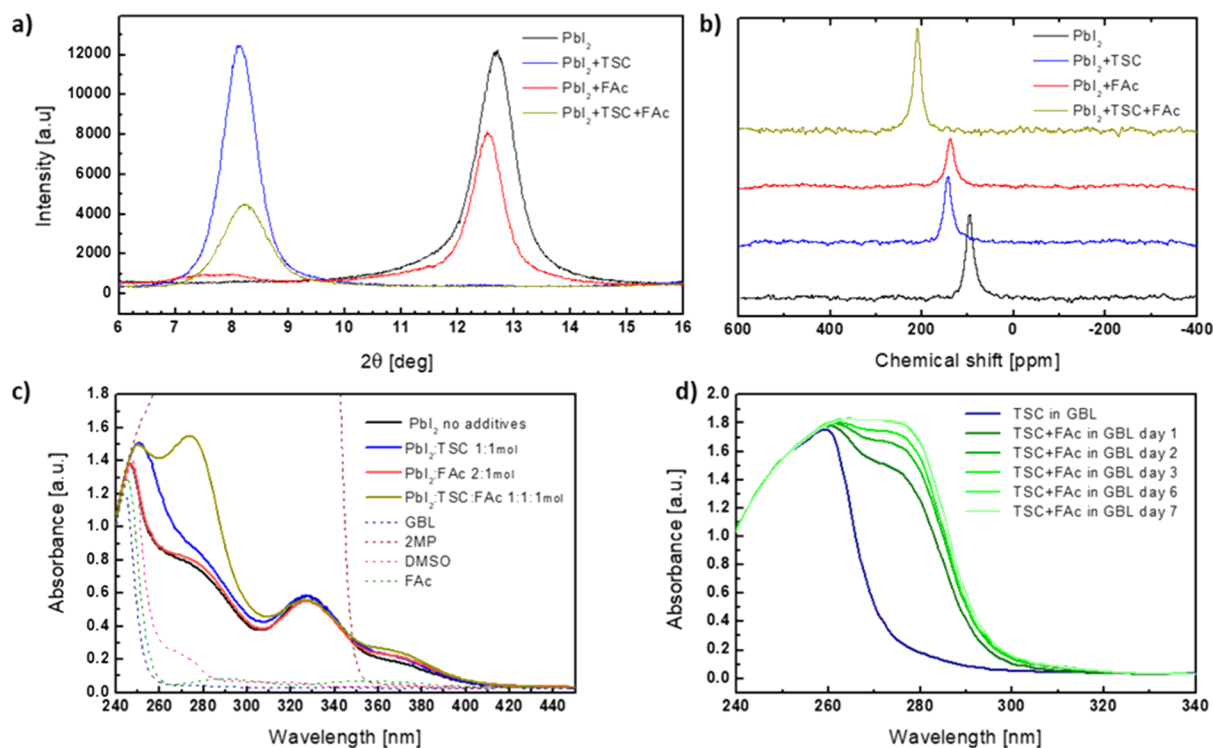
Figure 2. (a) XRD patterns of powders precipitated from different PbI_2 solutions in DMF (with and without additives); (b) ^{207}Pb NMR spectra of different PbI_2 solutions in DMSO-d_6 (with and without additives); (c) UV−vis spectra of solvents and PbI_2 solutions in GBL (with and without additives); (d) UV−vis spectra of TSC solution in GBL with the acid additive subjected to aging.

crystallization process can be obtained, which is particularly important for ambient processing conditions (additional moisture coordination).[28,46]

GBL used in our solvent system has a lower donor number (D_N = 18 kcal/mol) and lower intermolecular binding energy than commonly used DMF (D_N = 26.6 kcal/mol), meaning lower coordination tendency to Pb^{2+}. Even though we used it in conjunction with 2MP and DMSO (D_N = 30 kcal/mol), the mixture does not provide enough coordination strength to form stable $PbI_2(solvent)_x$ complexes.[46] The crystallization of the layer without any additives was fast and difficult to control, leading to noncompact layers, as pictured in SEM images in Figure 1a. To strengthen the intermediate phase and delay perovskite crystallization, we added a strongly coordinating compound to the precursor solution, which can form stable coordination complexes with Pb^{2+} and allow perovskite printing in ambient conditions. The coordination strength of Lewis base materials largely depends on the electron-donating atom having a lone electron pair. Typically, we distinguish O-donors, N-donors, and S-donors. It was shown that sulfur-containing molecules exhibit a very strong affinity to bind with Pb^{2+}, similarly to commonly used N-type donors.[43,47,48] We chose TSC, the compound containing both C=S and N−H groups, known in the literature as a good chelating agent for heavy metal ions, and also reported as a coordinating additive for perovskite precursor solution.[49−53] We note that non-volatile, solid additives remain in the film after the annealing process; hence, their impact on the electronic properties of the perovskite layer (e.g. the insulating character of an additive limiting carrier transport) must be taken into account.[52] Lead iodide clusters present in the precursor solution act as nucleation centers; thus, they affect the morphology, grain size, and crystallinity of the final perovskite layer.[29,54] We

observed a significant improvement in the thin film morphology upon TSC addition (see Figure 1b); however, the XRD pattern of this layer showed the coexistence of multiple nonperovskite phases (see Figure 1e). To overcome this issue, we carried out an additive engineering strategy. As reported by Han et al., using multiple additives can be a constructive way to modulate crystal growth.[52] The authors found that the addition of TSC has to be accompanied by methylammonium acetate to improve film quality and in turn solar cell performance. However, the underlying interaction remains unclear and needs further investigation.

In order to unveil the mechanism of this coordination, we introduced FAc, also having a carboxyl group, to the precursor solution. The combination of FAc and TSC in the precursor ink resulted in a compact layer formation (Figure 1d), with a distinct crystalline perovskite structure (Figure 1e). We note that solution with the FAc additive only produced films with nonuniform coverage (Figure 1c) and poor crystallinity (Figure 1e). This suggests that incorporation of both additives is necessary to obtain the desired perovskite phase. In Figure 1f, we show UV−vis absorption spectra of all the films produced with different combinations of additives. It further corroborates improved characteristics (higher intensity, sharper absorption onset) of the perovskite film printed from the precursor solution containing both additives.

Next, we applied XRD, ^{207}Pb NMR, and UV−vis spectroscopy to study the impact of acid addition on Pb coordination characteristics. In Figure 2a, we show XRD patterns of solid precipitates, isolated from PbI_2 solutions (in DMF) with different additive combinations: (i) TSC, (ii) FAc, and (iii) TSC + FAc. The Bragg peak at 2θ = 8.17°, assigned to the PbI_2−TSC complex, was recorded for the first solution (i). It shifts only slightly toward the higher angle (2θ = 8.23°) for
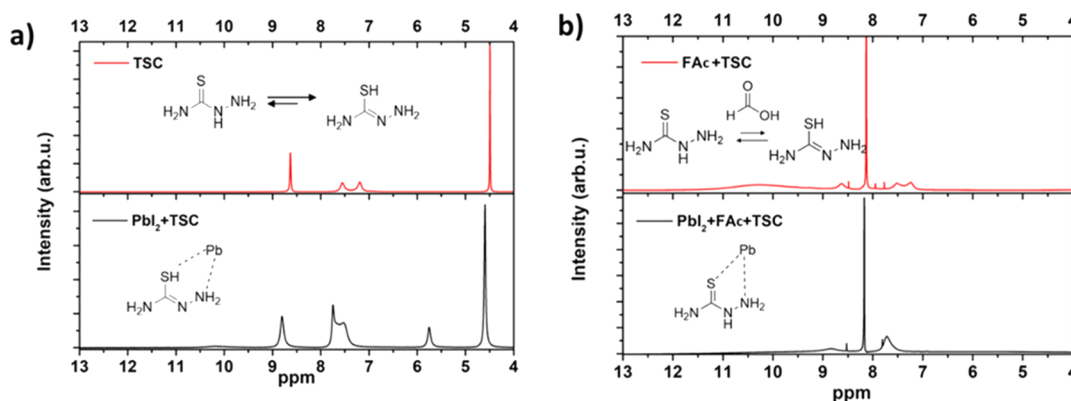
Figure 3. (a)^{1}H NMR spectra of pure TSC and TSC with PbI$_2$ in DMSO-d_6; (b) ^{1}H NMR spectra of the FAc/TSC mixture and with PbI$_2$ in DMSO-d_6.

solids prepared from the solution containing TSC and acid (iii). For the powder obtained from the solution with FAc (ii), the main diffraction peak appears at 12.56°, similarly to pure PbI$_2$ (12.65°). We conclude that FAc does not form a stable intermediate with Pb, but its presence affects the Pb−TSC complex structure. ^{207}Pb NMR spectroscopy analysis of neat lead iodide solution showed a chemical shift at 96.4 ppm, which shifts downfield upon the incorporation of additives, FAc (144.1 ppm) and TSC (137.9 ppm). When both additives are mixed into the solution, the lead resonance peak shifts even more downfield (210.1 ppm), as presented in Figure 2b. The above measurements confirmed that there is a change in lead coordination upon TSC and FAc addition. The UV−vis absorption spectrum of the solution containing both additives also differs compared to a single additive, showing a distinct new peak at 274 nm (Figure 2c). In order to understand the nature of this peak, we checked if it could arise from the interaction between the additives and the solvents. Interestingly, we found that the absorption spectrum of a simple solution of TSC in GBL shows the same peak upon acid addition (Figure 2d); thus, we assign it to the change in TSC or TSC−GBL interaction. Additionally, we noticed that this peak intensifies over time (green lines in Figure 2d). We note that the addition of acid to pure GBL did not induce a significant change in the absorption spectrum (Figure S3, Supporting Information). ^{1}H NMR of the solvents used in perovskite precursor ink (GBL, 2MP, and DMSO) with the FAc additive ruled out any chemical interactions between FAc and the solvent and did not indicate GBL hydrolysis (Figure S4, Supporting Information).

Next, we applied ^{1}H NMR spectroscopy to study potential chemical interactions between PbI$_2$ and additives (TSC, FAc), in order to understand how the presence of acid is affecting the coordination environment. We observed a structural change of TSC in the presence of FAc (Figure 3). The evolution suggests that upon acid incorporation, tautomerization of TSC takes place, from the thiol to thione form, which was also reported by Srinivasan et al.[55]

When the thiol form is present, four resonance peaks with a 1:1:1:2 integration ratio of the protons are visible, which upon addition to PbI$_2$ solution slightly shift downfield due to the coordination to the lead metal center (Figure 3a). When FAc and TSC are added to the solution, the resonance peaks at 4.5 and 12.6 ppm, assigned to the NH$_2$ and OH group, respectively, disappear (Figure 3b). Typically, OH and NH protons can exchange rapidly with each other, leading to a

single resonance peak at an average chemical shift of 8.1 ppm. Integration shows four protons at this position, which can be assigned to OH and CH protons of FAc and NH$_2$ protons of TSC. Additionally, the two resonance peaks at 7.2 and 7.5 ppm start to coalesce, which is likely to happen due to the equilibrium shift toward the thione form. If this mixture is added to the PbI$_2$ solution, the resonance peaks at 7.2 and 7.5 ppm coalesce to a single resonance signal, which we assign to the thione form.[55]

We suspect that TSC in its thione form, stabilized by the acidic environment, has a stronger coordination affinity to lead than its thiol tautomer, which thus forms different complex structures, which enable crystallization of the α-perovskite phase. In order to validate this, we compared the coordination strength of different coordinating molecules to Pb^{2+}, including TSC in thione and thiol forms, by applying DFT simulations. Specifically, we calculated the relative formation energy E_{rel}, defined as

$$E_{rel} = \frac{E_{tot} - E_{Pb} - E_{CM}*n}{n} \quad (1)$$

where E_{tot} is the total energy of the system, E_{Pb} and E_{CM} are the energies of unsolvated Pb^{2+} and the coordinating molecule, respectively, and n is the number of explicit coordinating molecules. Figure 4a illustrates the relative formation energy
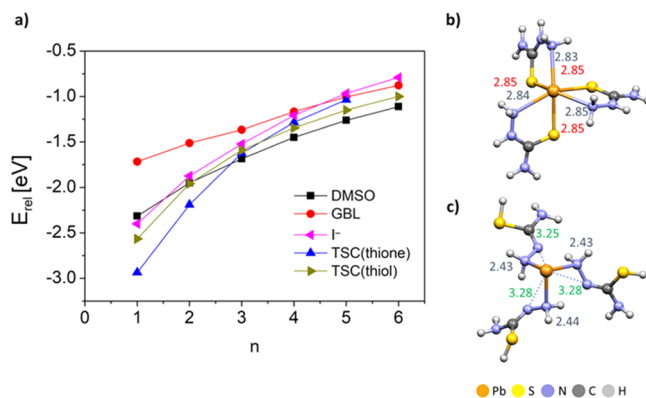

Figure 4. (a) Relative formation energy, E_{rel}, as a function of the number of coordinating molecules, n; graphical simulation of (b) Pb−thione (red/blue values refer to bond distances of Pb−S/Pb−N), and (c) Pb−thiol (blue/green values refer to bond distances of Pb−N from the NH$_2$ group/Pb−N bonded to NH$_2$) complex.
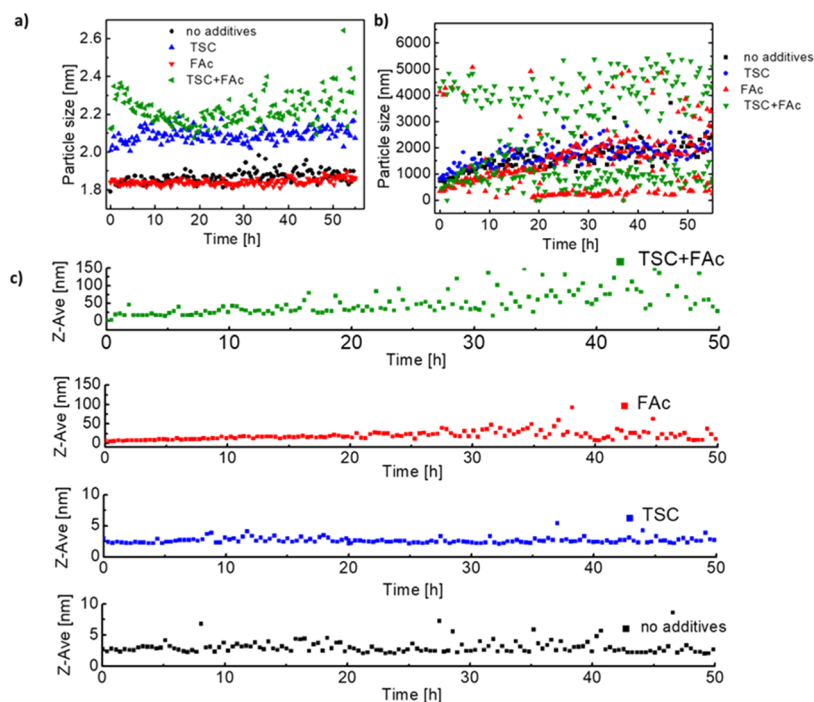
Figure 5. DLS study of particle size distribution in perovskite precursor inks, composed in the GBL/2MP/DMSO mixture with different combinations of additives. Each dot corresponds to a peak in the DLS spectrum fit, in the range of (a) 1.7−2.7, and (b) 0−6750 nm. (c) Average particle size (each dot) from all species identified in a single spectrum.

differences for $n \leq 6$. To compare the coordination ability of different species, we applied a simplified model where Pb atoms are coordinated by only one type of ligand. We note that in the real solution environment, the situation will be more complex, as multiple interactions between different components and varied concentrations of these species will affect the composition of Pb complexes. From the calculations shown in Figure 4a, it is evident that TSC molecules show the highest coordination affinity to Pb^{2+}. Interestingly, we note that Pb^{2+} preferentially binds one TSC tautomer or the other, depending on the n value. This is a consequence of the interactions that TSC establish with Pb^{2+}. The thione form can coordinate with the lead cation through a chelating interaction, thanks to the lone pair on S and N atoms. These interactions stabilize the thione up to $n = 3$, where the thermodynamically stable facial isomer shows similar average Pb−N and Pb−S distances of 2.83 and 2.84 Å, respectively (Figure 4b), suggesting strong chelation. These interactions are weaker but still retained for $n = 4$, with higher average bond distances (2.82 and 3.07 Å for Pb−N and Pb−S, respectively), while they partially get lost for $n = 5$, due to high steric hindrance.

Similarly, TSC in the thiol form tends to coordinate to Pb^{2+} with the lone pair of two bonded N atoms, with N from the NH_2 group being closer to lead. In the case of $n = 3$, the complex shows average bond distances of 3.27 and 2.43 Å (Figure 4c). Noteworthily, contrary to the case of the thione tautomer shown in Figure 4b, this complex shows a hemidirected configuration. It generally grants more free space to host more coordinating molecules. A fourth one ($n = 4$) can be easily accommodated, with only slightly higher average bond distances of 3.33 and 2.52 Å, when compared to $n = 3$. The same applies for $n = 5$, with distances of 3.33 and 2.61 Å. This explains why the thiol tautomer gives more stable complexes for the n values equal to 4 and 5. Overall, this suggests that TSC in the thione form preferentially binds with

Pb^{2+} until optimal hexacoordination is reached, after which the chelating interactions are getting weaker and leave the way for the thiol tautomer with higher n values. Pb−S bonds in a Pb−thione complex are less shielded in comparison to Pb−O and Pb−N, which could explain the downfield shift from 96.4 to 210.1 ppm, which was observed in ^{207}Pb-NMR (Figure 2b).[56,57] The thione tautomeric form of TSC, which is stabilized in the presence of FAc, leads to structurally different lead complexes in a precursor solution. This seems to facilitate the crystallization of the perovskite structure in the layer formation process, as shown in diffractograms in Figure 1e.

To understand the effect of additives on the colloids formation, we performed DLS analysis of full perovskite precursor solutions in the GBL/2MP/DMSO mixture, with different combinations of additives (no additives, only TSC, only FAc, TSC, and FAc combined). We are showing full spectra, taken at different time points for each solution, in Figure S5, Supporting Information, and graphical representation of size evolution in Figure 5.

In each perovskite solution, we observed at least two types of particles: small particles in a range of a few nm and bigger aggregates above 1 μm. Upon addition of the TSC, the average size of small particles increases from 1.87 to 2.09 nm and upon FAc incorporation, it decreases to 1.85 nm. Once TSC is present in the solution, the addition of acid causes an increase of the particle size (2.22 nm on average). Interestingly, small particles are initially dropping in size, and then around 20 h after acid addition, they start to grow again. The particle size of small species in the ink with both additives is evolving dynamically over time, while in the other inks, they remain almost constant during the whole measurement (Figure 5a). Apart from small particles (nanometer range), we also observe a population of large colloids (Figure 5b). In this case, we see a small and steady growth in a range of 500−2500 nm in all of the inks. Solutions with an acid additive display a pronounced
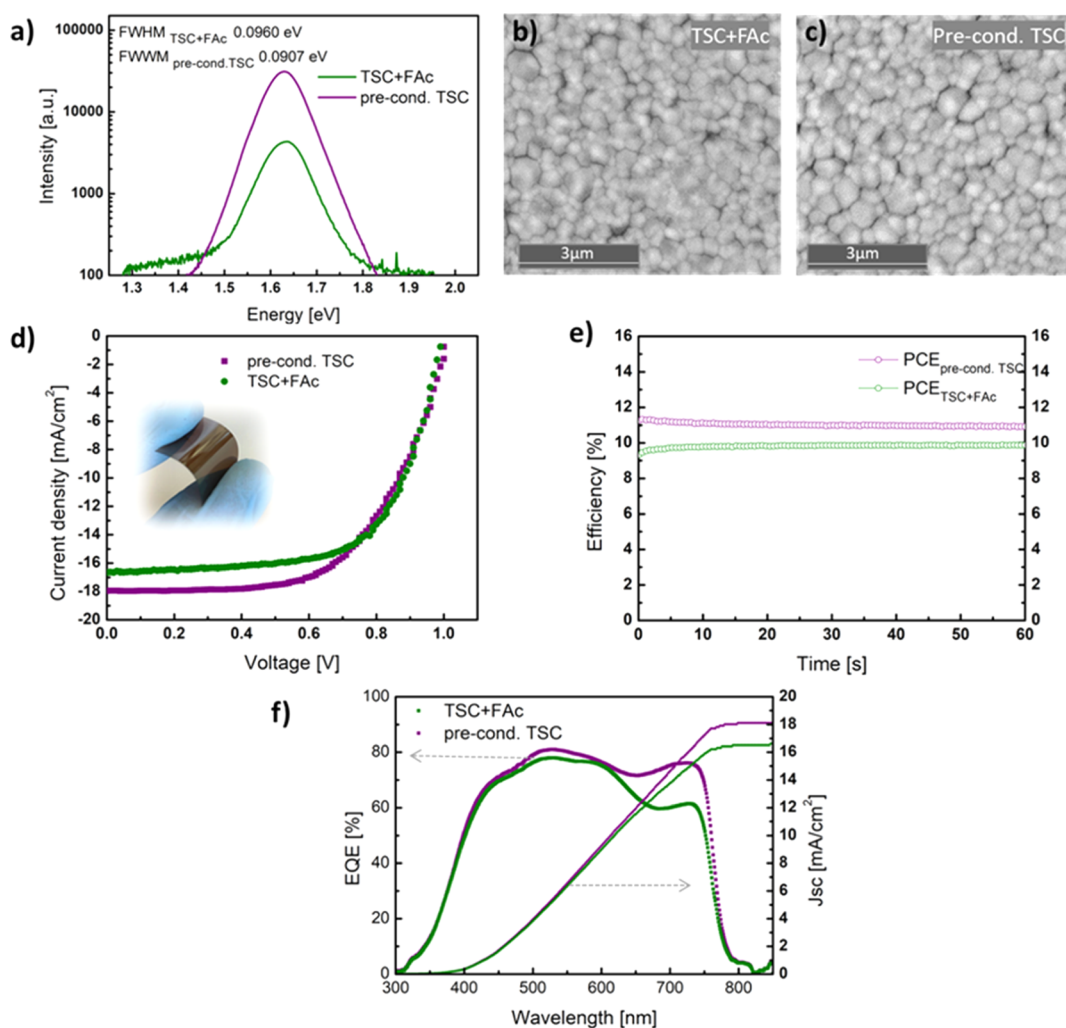
F

Figure 6. (a) ss-PL spectra and (b,c) SEM images of perovskite thin films printed on PET/IZO/PEDOT:PSS substrates, from the precursor solutions of different additive combinations (TSC + FAc, pre-conditioned TSC + FAc); (d) $J-V$ characteristics and (e) SPO of the best performing solar cells obtained for each perovskite precursor variation; (f) EQE spectra and integrated current densities of the same devices, measured in a spectral range from 300 to 850 nm.

third group of particles, with even larger colloids in the range of 3500−5000 nm. We plotted the weighted average of the particle size in Figure 5c to show a clear trend of particle size growth upon acid addition.

The observed phenomenon can be explained by a simple model considering the interactions that are established between two PbI_2 monomers in the presence of FAc. In particular, we speculate that the formate anion acts as a "bridge" between two PbI_2/TSC_x complexes, owing to its two coordinating oxygen atoms. The same mechanism can apply to the $PbI_2/DMSO$ complex, explaining the presence of some large particles in the solution with acid only.[41] To assess these theories, we derived the dimerization energy for the two PbI_2/TSC_x (with TSC in thione form) and two $PbI_2/DMSO_x$ units, considering $x = 2$, with and without incorporation of a formate anion linking the two lead centers. We found that the formation of such dimers is a spontaneous process (greater stabilization in the case of TSC ligand), and the inclusion of the formate anion further reduces the formation energy; thus, possibly explaining the increased particle size trend, we observed in the DLS result. In Figure S6, Supporting Information, we report a graphical representation of these results, including the dimer structures considered in our

estimations of formation energies. Similar to acid, the formation of large oligomers can also be triggered by water molecules, originating from an aqueous solution of FAc. This process referred to as the "zipping mechanism" was reported by Zhang et al. and was proved to have a significant influence on perovskite crystallization.[41]

We constructed planar heterojunction devices in p−i−n configuration embodying the following structure: PET/IZO/PEDOT:PSS/perovskite/C_{60}/BCP/Ag. All the photovoltaic devices reported in this work were fabricated on flexible substrates (PET foil), with over 1 cm^2 device active area. We selected polymer foils as a substrate choice due to the large commercial prospects of flexible perovskite photovoltaics.[6] We analyzed the impact of particle size in the ink on the solar cell performance by printing the formulation containing TSC and FAc at different times after solution preparation. We found that the evolution of particle size in the ink has a direct impact on the perovskite crystallization characteristics. Film morphologies are heavily affected by the colloid growth, triggered by FAc addition. It was reported before that large colloids present in the precursor solutions can act as perovskite nucleation centers. A high density of large colloidal clusters can significantly impact the nucleation rate, affecting optoelec-

-40-

Table 1. Photovoltaic Parameters PCE, Short-Circuit Current, J_{SC}, Open-Circuit Voltage, V_{OC}, and Fill Factor, FF (Average, avg, $\pm$ Standard Deviation, SD, and Maximum, max, Values) Extracted from the Current–Voltage Characterization Measurements of Solar Cells Fabricated with Two Optimized Additive Strategies for Perovskite Precursor Formulation

ink	number of cells	SPO of the best device [%]	$PCE^{avg \pm SD \, (max)}$ [%]	$J_{SC}^{avg \pm SD \, (max)}$ [mA/cm²]	$V_{OC}^{avg \pm SD \, (max)}$ [V]	$FF^{avg \pm SD \, (max)}$ [%]
TSC + FAc	15	9.9	9.27 ± 1.2 (10.94)	14.66 ± 1.75 (16.67)	0.98 ± 0.03 (1.01)	64.65 ± 3.82 (70.01)
pre-cond. TSC	24	10.9	10.39 ± 0.41 (11.4)	18.05 ± 0.68 (19.00)	0.96 ± 0.04 (1.00)	60.11 ± 4 (69.2)

tronic properties of perovskite polycrystalline films.[54] There is an optimum time after solution preparation (up to 30 h after acid addition) when the ink can still produce compact layers. Longer solution aging leads to deterioration of the perovskite morphology as well as the photovoltaic performance of the fabricated solar cells. In Figure S7, Supporting Information, we present SEM images of perovskite films printed from precursor inks of different ages. Figure S8, Supporting Information, displays current density–voltage (J–V) characteristics of the respective devices. Printing 24 h after solution preparation (acid addition) resulted in the best quality of perovskite thin films, delivering 10.90% of PCE, with a minimal hysteresis and stabilized power output (SPO) of 9.9%. J–V curves in both scan directions as shown in Figure S9, Supporting Information, and SPO measurement in Figure 6e.

The addition of acid causes a change in the TSC structure, which is beneficial for α-phase crystallization, but the formation of big clusters is undesirable and difficult to control. In order to limit the influence of acid on colloid growth and shorten the ink preparation procedure, we predissolved TSC in GBL and 2MP, added a small amount of acid (molar ratio of TSC to FAc reduced from 1:8 to 1:2.65), and stirred the mixture for 1 h with a moderate heating (80 °C). We noticed that warming up TSC with FAc in GBL induces a qualitatively similar change in the UV–vis spectrum as the aging shown in Figure 2d, suggesting that the changes in the TSC structure are accelerated by temperature (Figure S10, Supporting Information). Subsequently, the preconditioned mixture of additives was incorporated into the precursor solution. In this case, even a reduced amount of FAc was sufficient to obtain a desirable morphology (SEM image shown in Figure 6c) and improved crystallinity (higher intensity of dominant diffraction peaks when compared to the "TSC + FAc" sample, see Figure S11, Supporting Information) when coated immediately after solution preparation. In Figure S12, we show atomic force microscopy images of printed perovskite layers ("preconditioned TSC" and "TSC + FAc") and their cross-section images taken by focused ion beam SEM. Both films show similar average thickness (220–250 nm, "preconditioned TSC" is slightly thicker), but the sample fabricated from the "preconditioned TSC" ink formulation displays a smoother surface (Ra of only 5.8 nm, a two-fold reduction compared to the "TSC + FAc"), with larger and more uniform grain domains. Importantly, significantly reduced acid content in the precursor ink prevented the growth of large colloids, as we document with DLS analysis shown in Figure S13, Supporting Information. All these findings corroborate well with the observation that the change of the TSC structure facilitates crystallization of the pure perovskite phase. In Table 1, we listed photovoltaic parameters obtained for the PSCs prepared using both methods. J–V curves and SPOs of the champion devices for each ink variation are shown in Figures 6d,e, respectively. Scans in both directions are provided in Figures S9 and S14, Supporting Information. The ink with

preconditioned TSC produced devices of improved photovoltaic performance. A PCE of 11.4% was obtained from J–V characterization and 10.9% from the SPO measurement. The observed increase in current density values was corroborated by external quantum efficiency (EQE) measurements, where better charge extraction in the red part of the spectrum was recorded for the "preconditioned TSC" formulation (see Figure 6f). Such a difference in the long wavelength region (650–750 nm) of the EQE spectra can partially originate from the slightly thicker perovskite layer, but it also implies improved carrier extraction at the interface further away from the illumination source (perovskite/C_{60} interface) for the "preconditioned TSC" sample.[58,59] We postulate that a smoother surface (more uniform crystallite domains and fewer cavities between grain boundaries) can improve the quality of that electronic contact, reduce the energy barrier, and result in an increase of extraction efficacy. Furthermore, the "preconditioned TSC" sample exhibits improved crystallinity (Figure S11), which can also contribute to the improved transport properties through the bulk of the perovskite layer. This ink variation also improved the reproducibility and reduced a spread in photovoltaic performance parameters (standard deviation for each parameter shown in Table 1).

To gain more insights into the optoelectronic properties of printed layers, we measured ss-PL spectra of each perovskite type, processed on PET/IZO/PEDOT:PSS substrates. The spectra are shown in Figure 6a. We observe the same peak position for both samples, centered at 761 nm, with the "preconditioned TSC" sample displaying a higher intensity and reduced full width at half maximum. This implies reduced nonradiative recombination channels (bulk and surface recombination), potentially due to lower defect density in this sample. On the other hand, we do not observe any distinguishable difference in the recorded V_{OC} values of respective solar cells for these two types of perovskite films (see Figure 6d and Table 1). This might imply that dominant voltage losses in the applied device configuration originate from the perovskite interfaces, rather than the material's bulk. Particularly, the interface between perovskite and PEDOT:PSS was widely reported as the origin of significant nonradiative recombination losses, which limit the achievable V_{OC} of these devices.[60–62]

■ CONCLUSIONS

In summary, we have formulated perovskite precursor ink formulation for a reliable ink-jet printing process of mixed-cation perovskite thin films. Our solution is based on nontoxic solvents and it fulfills industrial manufacturing requirements (compatibility with industrial printheads). In the ink design, we have applied a Lewis base-type coordinating additive, TSC, to enable good quality of perovskite printed layers when processed in ambient conditions via the formation of a stable intermediate phase. We have shown that the TSC molecule can exist in two different tautomeric forms (thione or thiol),

H

which affects the coordination chemistry with perovskite precursor components. Due to controlled preconditioning of TSC in a mildly acidic environment, we were able to induce preferred complexation with lead species and obtain stable precursor formulation, which crystallizes into a pure perovskite phase. We have demonstrated planar heterojunction PSCs utilizing ink-jet printed perovskite layers, which were fabricated on flexible substrates. We obtained promising performance, reaching 11.4% of PCE with a large device active area (1 cm^2). This work significantly improves our understanding of the complex colloidal chemistry occurring in a perovskite precursor solution, which has a significant impact on the properties of deposited polycrystalline films. We note that there is a large scope for further improvement of a solar cell performance with this formulation, particularly by engineering the device architecture (interface modification of the hole transport layer−perovskite interface, PEDOT:PSS replacement).

■ ASSOCIATED CONTENT

ⓢ Supporting Information

The Supporting Information is available free of charge at https://pubs.acs.org/doi/10.1021/acssuschemeng.0c09208.

> additional solution (inkjet drop analysis, contact angle measurements, and DLS measurements); thin film and device characterization data (UV−vis, NMR, AFM, SEM, and *JV* curves); and DFT modeling details (PDF)

■ AUTHOR INFORMATION

Corresponding Author

Konrad Wojciechowski − *Saule Research Institute, Wrocław 54-130, Poland; Saule Technologies, Wrocław 54-130, Poland;* ⓘ orcid.org/0000-0002-7664-801X; Email: konrad.wojciechowski@sauletech.com

Authors

Barbara Wilk − *Saule Research Institute, Wrocław 54-130, Poland; Department of Semiconductor Materials Engineering, Wroclaw University of Science and Technology, Wrocław 50-370, Poland*

Senol Öz − *Saule Technologies, Wrocław 54-130, Poland*

Eros Radicchi − *Department of Chemistry, Biology and Biotechnology, University of Perugia, Perugia 06123, Italy; Computational Laboratory for Hybrid/Organic Photovoltaics (CLHYO), Istituto CNR di Scienze e Tecnologie Chimiche "Giulio Natta" (CNR-SCITEC), 06123 Perugia, Italy*

Feray Ünlü − *Department of Chemistry, Inorganic Chemistry, University of Cologne, Cologne D-50939, Germany*

Taimoor Ahmad − *Saule Technologies, Wrocław 54-130, Poland;* ⓘ orcid.org/0000-0001-9922-9603

Artur P. Herman − *Department of Semiconductor Materials Engineering, Wroclaw University of Science and Technology, Wrocław 50-370, Poland;* ⓘ orcid.org/0000-0002-1393-0317

Francesca Nunzi − *Department of Chemistry, Biology and Biotechnology, University of Perugia, Perugia 06123, Italy; Computational Laboratory for Hybrid/Organic Photovoltaics (CLHYO), Istituto CNR di Scienze e Tecnologie Chimiche "Giulio Natta" (CNR-SCITEC), 06123 Perugia, Italy;* ⓘ orcid.org/0000-0003-0995-1497

Sanjay Mathur − *Department of Chemistry, Inorganic Chemistry, University of Cologne, Cologne D-50939, Germany;* ⓘ orcid.org/0000-0003-2765-2693

Robert Kudrawiec − *Department of Semiconductor Materials Engineering, Wroclaw University of Science and Technology, Wrocław 50-370, Poland;* ⓘ orcid.org/0000-0003-2593-9172

Complete contact information is available at:
https://pubs.acs.org/10.1021/acssuschemeng.0c09208

Author Contributions

The manuscript was written through the contributions of all authors. All authors have given approval to the final version of the manuscript.

Notes

The authors declare no competing financial interest.

■ REFERENCES

(1) http://www.nrel.gov/ncpv/ (accessed 17 Dec 2020).

(2) Yin, W.-J.; Shi, T.; Yan, Y. Unique Properties of Halide Perovskites as Possible Origins of the Superior Solar Cell Performance. *Adv. Mater.* **2014**, *26*, 4653−4658.

(3) Yang, Z.; Surrente, A.; Galkowski, K.; Bruyant, N.; Maude, D. K.; Haghighirad, A. A.; Snaith, H. J.; Plochocka, P.; Nicholas, R. J. Unraveling the Exciton Binding Energy and the Dielectric Constant in Single-Crystal Methylammonium Lead Triiodide Perovskite. *J. Phys. Chem. Lett.* **2017**, *8*, 1851−1855.

(4) Stranks, S. D.; Eperon, G. E.; Grancini, G.; Menelaou, C.; Alcocer, M. J. P.; Leijtens, T.; Herz, L. M.; Petrozza, A.; Snaith, H. J. Electron-Hole Diffusion Lengths Exceeding 1 Micrometer in an Organometal Trihalide Perovskite Absorber. *Science* **2013**, *342*, 341−344.

(5) Snaith, H. J. Perovskites: The Emergence of a New Era for Low-Cost, High-Efficiency Solar Cells. *J. Am. Chem. Soc.* **2013**, *4*, 3623−3630.

(6) Wojciechowski, K.; Forgács, D.; Rivera, T. Industrial Opportunities and Challenges for Perovskite Photovoltaic Technology. *Sol. RRL* **2019**, *3*, 1900144.

(7) Reese, M. O.; Glynn, S.; Kempe, M. D.; McGott, D. L.; Dabney, M. S.; Barnes, T. M.; Booth, S.; Feldman, D.; Haegel, N. M. Increasing Markets and Decreasing Package Weight for High-Specific-Power Photovoltaics. *Nat. Energy* **2018**, *3*, 1002−1012.

(8) Vidal, R.; Alberola-Borràs, J.-A.; Joaquín-Luis, G.-M.; Habisreutinger, S. N.; Moore, D. T.; Schloemer, T. H.; Mora-Seró, I.; Berry, J. J.; Luther, J. M. Assessing Health and Environmental Impacts of Solvents for Producing Perovskite Solar Cells. *Nat. Sustain.* **2020**, DOI: 10.1038/s41893-020-00645-8.

(9) Saliba, M.; Nazeeruddin, K.; Zakeeruddin, S. M. Cesium-Containing Triple Cation Perovskite Solar Cells : Improved Stability , Reproducibility and High Efficiency. *Energy Environ. Sci.* **2016**, *9*, 1989.

(10) Öz, S.; Burschka, J.; Jung, E.; Bhattacharjee, R.; Fischer, T.; Mettenbörger, A.; Wang, H.; Mathur, S. Protic Ionic Liquid Assisted Solution Processing of Lead Halide Perovskites with Water, Alcohols and Acetonitrile. *Nano Energy* **2018**, *51*, 632−638.

(11) Wang, J.; Di Giacomo, F.; Brüls, J.; Gorter, H.; Katsouras, I.; Groen, P.; Janssen, R. A. J.; Andriessen, R.; Galagan, Y. Highly Efficient Perovskite Solar Cells Using Non-Toxic Industry Compatible Solvent System. *Sol. RRL* **2017**, *1*, 1700091.

(12) Gardner, K. L.; Tait, J. G.; Merckx, T.; Qiu, W.; Paetzold, U. W.; Kootstra, L.; Jaysankar, M.; Gehlhaar, R.; Cheyns, D.; Heremans, P.; Poortmans, J. Nonhazardous Solvent Systems for Processing Perovskite Photovoltaics. *Adv. Energy Mater.* **2016**, *6*, 1670084.

(13) Huang, S.-H.; Tian, K.-Y.; Huang, H.-C.; Li, C.-F.; Chu, W.-C.; Lee, K.-M.; Huang, Y.-C.; Su, W.-F. Controlling the Morphology and Interface of the Perovskite Layer for Scalable High-Efficiency Solar Cells Fabricated Using Green Solvents and Blade Coating in an Ambient Environment. *ACS Appl. Mater. Interfaces* **2020**, *12*, 26041−26049.

(14) Sveinbjörnsson, K.; Kyi Thein, N. K.; Saki, Z.; Svanström, S.; Yang, W.; Cappel, U. B.; Rensmo, H.; Boschloo, G.; Aitola, K.; Johansson, E. M. J. Preparation of Mixed-Ion and Inorganic Perovskite Films Using Water and Isopropanol as Solvents for Solar Cell Applications. *Sustainable Energy Fuels* **2018**, *2*, 606−615.

(15) Jung, J. W.; Williams, S. T.; Jen, A. K.-Y. Low-Temperature Processed High-Performance Flexible Perovskite Solar Cells via Rationally Optimized Solvent Washing Treatments. *RSC Adv.* **2014**, *4*, 62971−62977.

(16) Mathies, F.; List-Kratochvil, E. J. W.; Unger, E. L. Advances in Inkjet-Printed Metal Halide Perovskite Photovoltaic and Optoelectronic Devices. *Energy Technol.* **2019**, *8*, 1900991.

(17) Wei, Z.; Chen, H.; Yan, K.; Yang, S. Inkjet Printing and Instant Chemical Transformation of a CH3NH3PbI3/Nanocarbon Electrode and Interface for Planar Perovskite Solar Cells. *Angew. Chem., Int. Ed.* **2014**, *53*, 13239−13243.

(18) Li, S.-G.; Jiang, K.-J.; Su, M.-J.; Cui, X.-P.; Huang, J.-H.; Zhang, Q.-Q.; Zhou, X.-Q.; Yang, L.-M.; Song, Y.-L. Inkjet Printing CH3NH3PbI3 on Mesoscopic TiO2 Film for Highly Efficient Perovskite Solar Cells. *J. Mater. Chem. A* **2014**, *3*, 9092−9097.

(19) Mathies, F.; Eggers, H.; Richards, B. S.; Hernandez-Sosa, G.; Lemmer, U.; Paetzold, U. W. Inkjet-Printed Triple Cation Perovskite Solar Cells. *ACS Appl. Energy Mater.* **2018**, *1*, 1834−1839.

(20) Liang, C.; Li, P.; Gu, H.; Zhang, Y.; Li, F.; Song, Y.; Shao, G.; Mathews, N.; Xing, G. One-Step Inkjet Printed Perovskite in Air for Efficient Light Harvesting (Solar RRL 2/2018). *Sol. RRL* **2018**, *2*, 1770150.

(21) Ahmad, T.; Wilk, B.; Radicchi, E.; Fuentes Pineda, R.; Spinelli, P.; Herterich, J.; Castriotta, L. A.; Dasgupta, S.; Mosconi, E.; De Angelis, F.; Kohlstädt, M.; Würfel, U.; Di Carlo, A.; Wojciechowski, K. New Fullerene Derivative as an N-Type Material for Highly Efficient, Flexible Perovskite Solar Cells of a P-i-n Configuration. *Adv. Funct. Mater.* **2020**, *30*, 2004357.

(22) Eggers, H.; Schackmar, F.; Abzieher, T.; Sun, Q.; Lemmer, U.; Vaynzof, Y.; Richards, B. S.; Hernandez-Sosa, G.; Paetzold, U. W. Inkjet-Printed Micrometer-Thick Perovskite Solar Cells with Large Columnar Grains. *Adv. Energy Mater.* **2020**, *10*, 1903184.

(23) Jeon, N. J.; Noh, J. H.; Kim, Y. C.; Yang, W. S.; Ryu, S.; Seok, S. I. Solvent Engineering for High-Performance Inorganic-Organic Hybrid Perovskite Solar Cells. *Nat. Mater.* **2014**, *13*, 897−903.

(24) Radicchi, E.; Mosconi, E.; Elisei, F.; Nunzi, F.; De Angelis, F. Understanding the Solution Chemistry of Lead Halide Perovskites Precursors. *ACS Appl. Energy Mater.* **2019**, *2*, 3400−3409.

(25) Yan, K.; Long, M.; Zhang, T.; Wei, Z.; Chen, H.; Yang, S.; Xu, J. Hybrid Halide Perovskite Solar Cell Precursors: Colloidal Chemistry and Coordination Engineering behind Device Processing for High Efficiency. *J. Am. Chem. Soc.* **2015**, *137*, 4460−4468.

(26) Dutta, N. S.; Noel, N. K.; Arnold, C. B. Crystalline Nature of Colloids in Methylammonium Lead Halide Perovskite Precursor Inks Revealed by Cryo-Electron Microscopy. *J. Phys. Chem. Lett.* **2020**, *11*, 5980−5986.

(27) Li, Z.; Sun, Y.; Yao, H.; Zhao, J.; Wang, Q.; Ding, L.; Jin, Z. Intermediates Transformation for Efficient Perovskite Solar Cells. *J. Energy Chem.* **2021**, *52*, 102−114.

(28) Li, B.; Li, M.; Fei, C.; Cao, G.; Tian, J. Colloidal Engineering for Monolayer CH3NH3PbI3 Films toward High Performance Perovskite Solar Cells. *J. Mater. Chem. A* **2017**, *5*, 24168−24177.

(29) Pratap, S.; Schlipf, J.; Bießmann, L.; Müller-Buschbaum, P. Hierarchical Structures from Nanocrystalline Colloidal Precursors within Hybrid Perovskite Thin Films: Implications for Photovoltaics. *ACS Appl. Nano Mater.* **2020**, *3*, 11701.

(30) Lee, J.-W.; Kim, H.-S.; Park, N.-G. Lewis Acid-Base Adduct Approach for High Efficiency Perovskite Solar Cells. *Acc. Chem. Res.* **2016**, *49*, 311−319.

(31) Singh, R. K.; Kumar, R.; Kumar, A.; Jain, N.; Singh, R. K.; Singh, J. Novel Synthesis Process of Methyl Ammonium Bromide and Effect of Particle Size on Structural, Optical and Thermodynamic Behavior of CH3NH3PbBr3 Organometallic Perovskite Light Harvester. *J. Alloys Compd.* **2018**, *743*, 728−736.

(32) Zhang, Y.; Ma, Y.; Shin, I.; Jung, Y. K.; Lee, B. R.; Wu, S.; Jeong, J. H.; Lee, B. H.; Kim, J. H.; Kim, K. H.; Park, S. H. Lead Acetate Assisted Interface Engineering for Highly Efficient and Stable Perovskite Solar Cells. *ACS Appl. Mater. Interfaces* **2020**, *12*, 7186−7197.

(33) Frisch, M. J.; Trucks, G. W.; Schlegel, H. B.; Scuseria, G. E.; Robb, M. A.; Cheeseman, J. R.; Scalmani, G.; Barone, V.; Petersson, G. A.; Nakatsuji, H.; Caricato, M.; Marenich, A.; Bloino, J.; Janesko, B. G.; Gomperts, R.; Mennucci, B.; Hratchian, H. P.; Fox, D. J. *Gaussian 09*, Revision D. 01; Gaussian, Inc.: Wallingford CT 2016.

(34) Becke, A. D. Density-Functional Thermochemistry. III. The Role of Exact Exchange. *J. Chem. Phys.* **1993**, *98*, 5648−5652.

(35) Stephens, P. J.; Devlin, F. J.; Chabalowski, C. F.; Frisch, M. J. Ab Initio Calculation of Vibrational Absorption and Circular Dichroism Spectra Using Density Functional Force Fields. *J. Phys. Chem.* **1994**, *98*, 11623−11627.

(36) Cossi, M.; Rega, N.; Scalmani, G.; Barone, V. Energies, Structures, and Electronic Properties of Molecules in Solution with the C-PCM Solvation Model. *J. Comput. Chem.* **2003**, *24*, 669−681.

(37) Babayigit, A.; D'Haen, J.; Boyen, H.-G.; Conings, B. Gas Quenching for Perovskite Thin Film Deposition. *Joule* **2018**, *2*, 1205−1209.

(38) Fateev, S. A.; Petrov, A. A.; Khrustalev, V. N.; Dorovatovskii, P. V.; Zubavichus, Y. V.; Goodilin, E. A.; Tarasov, A. B. Solution Processing of Methylammonium Lead Iodide Perovskite from γ-Butyrolactone: Crystallization Mediated by Solvation Equilibrium. *Chem. Mater.* **2018**, *30*, 5237−5244.

(39) Stoumpos, C. C.; Malliakas, C. D.; Kanatzidis, M. G. Semiconducting Tin and Lead Iodide Perovskites with Organic Cations: Phase Transitions, High Mobilities, and near-Infrared Photoluminescent Properties. *Inorg. Chem.* **2013**, *52*, 9019−9038.

(40) Li, B.; Binks, D.; Cao, G.; Tian, J. Engineering Halide Perovskite Crystals through Precursor Chemistry. *Small* **2019**, *15*, 1903613.

(41) Zhang, K.; Wang, Z.; Wang, G.; Wang, J.; Li, Y.; Qian, W.; Zheng, S.; Xiao, S.; Yang, S. A Prenucleation Strategy for Ambient Fabrication of Perovskite Solar Cells with High Device Performance Uniformity. *Nat. Commun.* **2020**, *11*, 1006.

(42) Wang, M.; Cao, F.; Deng, K.; Li, L. Adduct Phases Induced Controlled Crystallization for Mixed-Cation Perovskite Solar Cells with Efficiency over 21%. *Nano Energy* **2019**, *63*, 103867.

(43) Wharf, I.; Gramstad, T.; Makhija, R.; Onyszchuk, M. Synthesis and Vibrational Spectra of Some Lead(II) Halide Adducts with O-, S-, and N-Donor Atom Ligands. *Can. J. Chem.* **1976**, *54*, 3430−3438.

(44) Yang, W. S.; Noh, J. H.; Jeon, N. J.; Kim, Y. C.; Ryu, S.; Seo, J.; Seok, S. I. Il. High-Performance Photovoltaic Perovskite Layers

Fabricated through Intramolecular Exchange. *Science* **2015**, *348*, 1234−1237.

(45) Ahn, N.; Son, D. Y.; Jang, I. H.; Kang, S. M.; Choi, M.; Park, N. G. Highly Reproducible Perovskite Solar Cells with Average Efficiency of 18.3% and Best Efficiency of 19.7% Fabricated via Lewis Base Adduct of Lead(II) Iodide. *J. Am. Chem. Soc.* **2015**, *137*, 8696.

(46) Hamill, J. C.; Schwartz, J.; Loo, Y.-L. Influence of Solvent Coordination on Hybrid Organic-Inorganic Perovskite Formation. *ACS Energy Lett.* **2018**, *3*, 92−97.

(47) Liu, C.; Cheng, Y.-B.; Ge, Z. Understanding of Perovskite Crystal Growth and Film Formation in Scalable Deposition Processes. *Chem. Soc. Rev.* **2020**, *49*, 1653−1687.

(48) Hamill, J. C.; Romiluyi, O.; Thomas, S. A.; Cetola, J.; Schwartz, J.; Toney, M. F.; Clancy, P.; Loo, Y.-L. Sulfur-Donor Solvents Strongly Coordinate Pb^{2+} in Hybrid Organic-Inorganic Perovskite Precursor Solutions. *J. Phys. Chem. C* **2020**, *124*, 14496−14502.

(49) Ahamed, M. A. R.; Jeyakumar, D.; Burkanudeen, A. R. Removal of Cations Using Ion-Binding Terpolymer Involving 2-Amino-6-Nitro-Benzothiazole and Thiosemicarbazide with Formaldehyde by Batch Equilibrium Technique. *J. Hazard. Mater.* **2013**, *248-249*, 59−68.

(50) Li, M.; Zhang, Z.; Li, R.; Wang, J. J.; Ali, A. Removal of Pb(II) and Cd(II) Ions from Aqueous Solution by Thiosemicarbazide Modified Chitosan. *Int. J. Biol. Macromol.* **2016**, *86*, 876−884.

(51) Ahmad, M.; Ahmed, S.; Swami, B. L.; Ikram, S. Preparation and Characterization of Antibacterial Thiosemicarbazide Chitosan as Efficient Cu(II) Adsorbent. *Carbohydr. Polym.* **2015**, *132*, 164−172.

(52) Wu, Y.; Xie, F.; Chen, H.; Yang, X.; Su, H.; Cai, M. Thermally Stable $MAPbI_3$ Perovskite Solar Cells with Efficiency of 19 . 19 % and Area over 1 Cm^2 Achieved by Additive Engineering. *Adv. Mater.* **2017**, *29*, 1701073.

(53) Ishikawa, R.; Ueno, K.; Shirai, H. Highly Crystalline Large-Grained Perovskite Films Using Two Additives without an Antisolvent for High-Efficiency Solar Cells. *Thin Solid Films* **2019**, *679*, 27−34.

(54) McMeekin, D. P.; Wang, Z.; Rehman, W.; Pulvirenti, F.; Patel, J. B.; Noel, N. K.; Johnston, M. B.; Marder, S. R.; Herz, L. M.; Snaith, H. J. Crystallization Kinetics and Morphology Control of Formamidinium−Cesium Mixed-Cation Lead Mixed-Halide Perovskite via Tunability of the Colloidal Precursor Solution. *Adv. Mater.* **2017**, *29*, 1607039.

(55) Srinivasan, B. R.; Raghavaiah, P.; Nadkarni, V. S. Reinvestigation of Growth of Urea Thiosemicarbazone Monohydrate Crystal. *Spectrochim. Acta, Part A* **2013**, *112*, 84−89.

(56) Wrackmeyer, B. *Annual Reports on NMR Spectroscopy*; Elsevier, 2002; Vol. *47*.

(57) Wrackmeyer, B.; Horchler, K. *Annual Reports on NMR Spectroscopy*; Elsevier, 1990; Vol. *22*, p 249.

(58) Bu, T.; Wu, L.; Liu, X.; Yang, X.; Zhou, P.; Yu, X.; Qin, T.; Shi, J.; Wang, S.; Li, S.; Ku, Z.; Peng, Y.; Huang, F.; Meng, Q.; Cheng, Y. B.; Zhong, J. Synergic Interface Optimization with Green Solvent Engineering in Mixed Perovskite Solar Cells. *Adv. Energy Mater.* **2017**, *7*, 1770111.

(59) Tong, G.; Son, D. Y.; Ono, L. K.; Liu, Y.; Hu, Y.; Zhang, H.; Jamshaid, A.; Qiu, L.; Liu, Z.; Qi, Y. Scalable Fabrication of >90 Cm^2 Perovskite Solar Modules with >1000 h Operational Stability Based on the Intermediate Phase Strategy. *Adv. Energy Mater.* **2021**, 202003712.

(60) Wolff, C. M.; Caprioglio, P.; Stolterfoht, M.; Neher, D. Nonradiative Recombination in Perovskite Solar Cells: The Role of Interfaces. *Adv. Mater.* **2019**, *31*, 1902762.

(61) Wang, J.; Fu, W.; Jariwala, S.; Sinha, I.; Jen, A. K.-Y.; Ginger, D. S. Reducing Surface Recombination Velocities at the Electrical Contacts Will Improve Perovskite Photovoltaics. *ACS Energy Lett.* **2019**, *4*, 222−227.

(62) Khadka, D. B.; Shirai, Y.; Yanagida, M.; Ryan, J. W.; Miyano, K. Exploring the Effects of Interfacial Carrier Transport Layers on Device Performance and Optoelectronic Properties of Planar Perovskite Solar Cells. *J. Mater. Chem. C* **2017**, *5*, 8819−8827.

-44-

5.Inkjet printing of 2D perovskite

Barbara Wilk contribution:

- Adjusting the ink composition to meet inkjet criteria, solvents base ink modification;
- Characterization of rheological properties of the inks;
- Optimization of the printing process: waveform design; printing parameters adjustment;
- Performing the printing process;
- Optimization of the post-treatment methods;
- Experiments design, data analysis;
- Supporting the characterization and measurement of full solar cells;
- Manuscript writing.

Inkjet Printing of Quasi-2D Perovskite Layers with Optimized Drying Protocol for Efficient Solar Cells

Barbara Wilk, Sylvester Sahayaraj, Marcin Ziółek, Vivek Babu, Robert Kudrawiec, and Konrad Wojciechowski*

Metal halide perovskites of reduced dimensionality constitute an interesting subcategory of the perovskite semiconductor family, which attract a lot of attention, primarily due to their excellent moisture resistance and peculiar optoelectronic properties. Specifically, quasi-2D materials of the Ruddlesden–Popper (RP) type, are intensely investigated as photoactive layers in perovskite solar cells. Here, a scalable deposition of quasi-2D perovskite thin films, with a nominal composition of 4F-PEA$_2$MA$_4$Pb$_5$I$_{16}$ (4-FPEA$^+$-4-fluorophenethylammonium, applied as a spacer cation), using an inkjet printing technique, is developed. An optimized precursor formulation, and appropriate post-printing treatment, which enable good control over nucleation and crystal growth steps, result in highly crystalline and uniform perovskite layers. Particularly, vacuum with nitrogen flushing provides an optimal drying treatment, which produces a more uniform distribution of low dimensional phases, and a high level of vertical (out-of-plane) alignment, which is beneficial for charge carrier transport. Solar cells reaching 13% of power conversion efficiency for the rigid, and 10.6% for the flexible, large area (1 cm^2) devices are presented.

1. Introduction

Metal halide perovskite solar cells have shown remarkable progress in recent years, reaching a certified power conversion efficiency (PCE) of 25.7%.[1] With such prolific technological advancements, largely obtained at the academic level, the technology is moving towards the commercialization phase.[2] However, the inherent environmental sensitivity of hybrid perovskites remains one of the main challenges, adding risk to the long-term reliability of these devices.[3]

Recently, perovskite compositions, which induce structures of reduced dimensionality, were reported as an interesting family of compounds, exhibiting promising environmental stability and effective photovoltaic performance parameters.[4,5] Within that category, Ruddlesden–Popper perovskite types were most often used in thin-film solar cells. Such layered structures, also referred to as quasi-2D perovskites, are described by the empirical formula of (LC)$_2$(SC)$_{n-1}$Pb$_n$I$_{3n+1}$, where LC is a cation with a large ionic radius (usually an aromatic or aliphatic alkyl ammonium halide), SC is a small cation (typically, methylammonium – MA$^+$, or formamidinium – FA$^+$), and n is the number of confined lead halide octahedral layers.[5] When the perovskite film is processed from a precursor solution, bulky cations organize in a specific way, separating the 3D-like phases, and forming a layered structure. The unique arrangement of the lattice brings certain properties, which can be further tuned with appropriate compositional engineering.[6–8] Many compounds of different chain lengths and chemical structures were found to fit the role of the bulky cation.[9,10] Commonly, these large organic cations provide hydrophobic character, enhancing the water resistance of the perovskite layers.[11] The large cation can also passivate various electronic defects in the perovskite structure, and limit ion migration, which in turn provides better photostability.[12] As a result, the quasi-2D perovskites provide an interesting avenue for reaching improved structural robustness and enhanced operational stability when compared to the more conventional 3D counterparts, making them particularly suitable for terrestrial applications. As the large organic cation is electrically insulating, the orientation of perovskite grains needs to be carefully adjusted. In order to enable efficient charge carrier transport through the photoactive layer, low dimensional perovskite sheets need to be oriented perpendicularly to the substrate.[13] Various strategies of inducing preferential vertical alignment of 2D perovskite crystallites have been explored, including coordinating additives, or specific processing conditions, inducing preferential dynamics of the initial crystallization stages.[14,15] Recent advancements in this topic resulted in PCEs exceeding 20%, highlighting the large application potential for these materials. [16]

B. Wilk, S. Sahayaraj, K. Wojciechowski
Saule Research Institute
Wrocław Technology Park, 11 Duńska, Wrocław 54-427, Poland
E-mail: konrad.wojciechowski@sauletech.com

B. Wilk, V. Babu, K. Wojciechowski
Saule Technologies
Wrocław Technology Park, 11 Duńska, Wrocław 54-427, Poland

B. Wilk, R. Kudrawiec
Department of Semiconductor Materials Engineering
Wrocław University of Science and Technology
Wrocław 50-370, Poland

M. Ziółek
Faculty of Physics
Adam Mickiewicz University
Uniwersytetu Poznańskiego 2, Poznań, Wrocław 61-614, Poland

The ORCID identification number(s) for the author(s) of this article can be found under https://doi.org/10.1002/admt.202200606.

DOI: 10.1002/admt.202200606

Another technical challenge related to the commercialization of the perovskite PV technology is proving scalability of the manufacturing methods, and demonstration of reliable, large-area PV units of highly efficient operation. Many deposition techniques used in laboratories cannot be transferred to larger substrates. For example, spin-coating, anti-solvent technique, or hot-casting method constitute deposition protocols, which are commonly used for manufacturing perovskite thin films of various compositions, and cannot be implemented into an industrial processing scheme.[4,17,18] Scalable fabrication methods, together with the re-optimized ink formulations and developed processing routines need to be employed to obtain uniform layers over large-area substrates. A good understanding of precursor chemistry is needed to be able to control film formation dynamics.[19,20] Various solution-based coating techniques have been explored for perovskite thin film deposition, including spray-coating, slot-die coating, blade-coating, gravure or inkjet printing (IJP).[21–26] The latter technique is particularly interesting from an industrial point of view. IJP has been known in the field of graphics and electronics for over 50 years.[27] This digital, contactless technique recently gained a lot of interest in the perovskite community, as a versatile, reliable and cost-effective deposition method.[28] The IJP process enables customized production, with good control over film formation. The most commonly used system is a piezo-driven drop on demand printhead. Such systems enable the use of both, aqueous and organic solvent-based inks, with a wide range of viscosities, making it an attractive tool for perovskite solar cell production.[29,30] To achieve good jetting characteristics, and in turn satisfactory printout quality, there are a few important aspects to be considered. First, appropriate drop formation has to be ascertained. Rheological properties of the solution, often described by Reynolds (Re), Ohnesorge (Oh), and inverse of Ohnesorge (Z) numbers, have to meet the requirements, which are specific for a given printhead type.[31] Then, by adjusting the voltage applied to the transducer, a drop with a modulated volume and velocity is being ejected at the orifice. Once the ink is released, the second aspect of the printing process has to be considered, which is the ink-substrate interaction. The ink's surface tension, which defines the cohesion of the droplet and its adhesion to the substrate surface, needs to be balanced. Apart from providing good spreading, the surface energy will also affect nucleation, hence the crystallization of the perovskite material.[32] The wetting behavior can be tuned by applying surface activation treatments, like UV-ozone, or plasma.[33] The third aspect of the perovskite thin film formation is the control of a crystallization process. An ambient atmosphere can strongly affect crystallite growth, thus finding optimal conditions, adjusted for a specific formulation of a particular solvent system, provides the scope of the development work.

In this work, we optimized the composition of a quasi-2D perovskite precursor solution to meet the rheological criteria of inkjet printing and customized the waveform parameters to obtain uniform coatings. Special attention was given to the relation between drying dynamics and crystallite orientation in printed perovskite layers, which we analyzed with a range of spectroscopic and crystallographic characterization methods. We demonstrate that fast nucleation rate, obtained with a combined drying effect of vacuum and nitrogen flushing, and slow perovskite crystallite growth, produces a more uniform distribution of low dimensional phases, and a high level of vertical (out-of-plane) alignment, which is beneficial for the effective charge carrier transport. With the optimized processing conditions, we were able to fabricate inkjet-printed perovskite solar cells, reaching 13% efficiency on glass and 10.6% on PET substrates.

2. Results and Discussion

As a starting point, we applied a quasi-2D perovskite precursor composition based on our recently published work, where 4-fluoro-phenethylammonium iodide (4F-PEAI) was used as a spacer cation, and thiosemicarbazide (TSC) was incorporated as a coordinative additive to yield-oriented growth of perovskite crystallites.[14] We further optimized the formulation, particularly by fine-tuning the ratios of perovskite-forming components (methylammonium iodide, MAI; lead iodide, PbI_2; 4F-PEAI). Additionally, we added lead chloride ($PbCl_2$), which was shown to induce a vertical growth of the quasi-2D perovskite layer via in-situ formation of MACl.[34] The n-value, referring to the nominal number of inorganic octahedral units, $[PbI_6]^{4-}$, positioned between the spacer cations, was kept at 5. Optimized perovskite thin films, processed by spin-coating, were used for fabricating solar cells of a p–i–n configuration. The following device structure was applied: glass/indium tin oxide (ITO)/poly(triarylamine) (PTAA)/quasi-2D perovskite/fullerene (C_{60})/bathocuproine (BCP)/Ag. Current density–voltage (J–V) curves with a stabilized power output (SPO), and morphological, optical and crystallographic characterizations of perovskite films are displayed in **Figure 1**. We obtained a champion power conversion efficiency (PCE) of 14.6%, with negligible hysteretic effects (Figure 1a). The perovskite film appears dense and compact with no pinholes on the surface, as evidenced by the SEM image in Figure 1b. The white spots visible on the layer's surface at the first instance could be associated with unreacted PbI_2 (heavier components appear brighter in the backscatter electron detection mode), as it is often used in an over stoichiometric amount in the perovskite precursor solutions, and such assignments can be found in different 3D perovskite reports.[35,36] However, detailed crystallographic analysis (including grazing-incidence measurements that are primarily sensitive to the surface), which we carried out in our previous work, did not show any correlation between the presence of these features in top-view SEM images and the intensity of PbI_2 reflections[14]. Such white features have been observed in other reports addressing quasi-2D perovskite thin films. They were typically assigned to morphological characteristics, and specifically protuberances of small grains. [34,37,38] The UV–vis absorption spectrum in Figure 1c shows the existence of different low dimensional phases, with peaks at 570, 610, and 646 nm. These values are assigned to low dimensional phases of n equal 2, 3, and 4, respectively. The absorption onset at 770 nm, which relates to the 3D-like bulk phase, matches the peak position recorded in the photoluminescence spectrum of the same film (Figure 1c). Overall, the layer consists of a mixture of the 3D phase ($MAPbI_3$) and several low n phases. The X-ray diffraction (XRD) pattern (Figure 1d) confirms preferred

**ADVANCED
SCIENCE NEWS**
www.advancedsciencenews.com

**ADVANCED
MATERIALS
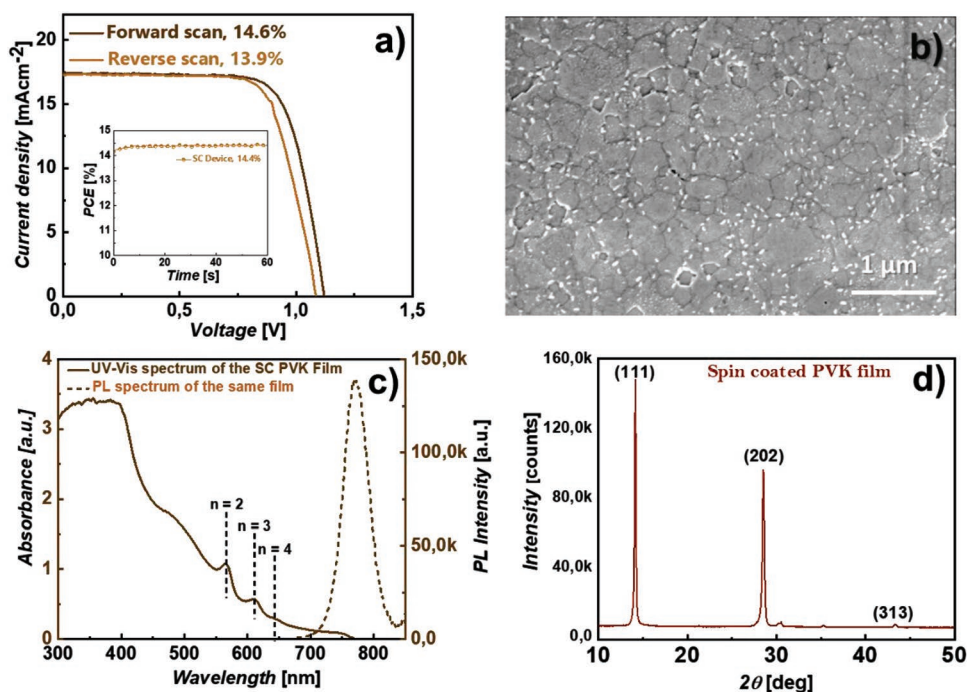TECHNOLOGIES**
www.advmattechnol.de

Figure 1. a) Current density–voltage curves in forward and reverse scan directions, and stabilized power output (inset) of the best device incorporating optimized quasi-2D perovskite thin film, prepared by spin-coating; b–d) a range of characterization measurements of the same perovskite layer, including b) top-view SEM image, c) photoluminescence and UV–vis absorption spectra, and d) X-ray diffractogram.

crystallite orientation, with two dominating reflections, at 14° and 28°, which are assigned to (111) and (202) planes.[39] The (111) plane represents the tilted orientation, whereas the (202) plane defines the out-of-plane orientation of the lead iodide inorganic sheets.[40,41] These reflections originate from the repeating unit of one octahedra (for lead-iodide based structures) being in line with the layers and are observed when the layers are perpendicular to the substrate.[42] In our case, since we have a mixture of low and high *n* phases in the film, we cannot assign its origin to only one particular phase.

Having obtained promising results with the spin-coating process, we applied the same precursor formulation to the scalable deposition, which we carried out by inkjet printing technique. The printing was executed in an ambient cleanroom atmosphere, with a controlled relative humidity of 25%. At first, ink's rheological properties were not optimized for the printing process, thus the jetting was suboptimal (Figure S1, Supporting Information). We observed undesired satellite drop formation, which can cause an off-target deposition and deviations in drop volumes. However, we were able to print perovskite layers and applied the drying conditions similar to the spin-coating process (samples were transferred to the glovebox after printing). Printed deposits displayed significantly faster crystallization, characterized by the appearance of brown color starting at the edges, a few seconds after printing. As a result, the perovskite formation took place even before any controlled drying atmosphere could be applied. This was reflected in the solar cell performance. Devices embodying these layers exhibited poor efficiency, reaching only up to 4.6%. Physical properties of perovskite films printed in such conditions are shown in Figure S2 (Supporting Information).

It is quite evident that both, ink's rheological properties and crystallization characteristics of the printed layer need to be modified for a reliable fabrication process in air. First, we adjusted the solvent system by adding dimethylsulfoxide (DMSO). The aim of this strategy was to suppress rapid perovskite crystallization, which takes place after exposing a wet film to humid air, and to enhance the stability of forming intermediate phases, which are based on DMSO-coordinating Pb complexes. [43,44] We characterized the rheological parameters of the precursor solution to find the optimal DMSO concentration. We tested three solutions, containing 5, 10, and 15 vol% of DMSO. The inverse (Z) of the Ohnesorge number (Oh), which relates to the viscosity, surface tension and density of a fluid, describes the printability of a given ink. The Z is given by (Equation (1))[45]

$$Z = \frac{1}{Oh} = \frac{\sqrt{\rho \sigma d}}{\eta} \tag{1}$$

where η is the viscosity of the ink [Pa s], ρ is the density of the ink [kg m^{-3}], σ is the surface tension of the ink [N m^{-1}], and d is the nozzle diameter [m].

The theoretical range of printability is defined by Z values in the range of $4 \leq Z \leq 14$.[31] Z values above 14 result in satellite formation, and values below 4 cause long-tail drops. The previous ink, based on only dimethylformamide (DMF) solvent, had the Z number of 15.13, explaining observed jetting behavior. The addition of DMSO caused the change in the rheological parameters, reducing the Z number. We obtained the following Z values for the DMF:DMSO solvent mixtures: 14.49, 13.81, and 13.99, relating to the 5, 10, and 15 vol% of DMSO,

**ADVANCED
SCIENCE NEWS**
www.advancedsciencenews.com

**ADVANCED
MATERIALS
TECHNOLOGIES**
www.advmattechnol.de

respectively. The ink with 10 vol% DMSO showed the best drop formation and stable jetting (Figure S3, Supporting Information), hence we kept this composition for the rest of the study. Detailed values of rheological properties for the formulated inks we provide in Table S1 (Supporting Information). The surface of the PTAA-coated substrates was treated by oxygen plasma to enable good spreading of the ink after printing. Contact angles of the printing solution for different surface activation methods are shown in Figure S4 (Supporting Information).

With the DMSO modification, the crystallization onset was slowed down, which allowed us to have better control over this process. The drying characteristics and rate of this process can significantly affect the specific orientation of different quasi-2D perovskite phases, which in turn is critical for the effective charge carrier transport in the photoactive layer, and ensuing photovoltaic performance of respective devices.[20] We applied a series of post-printing drying methods to find optimal conditions for the early-stage perovskite nucleation and crystallite growth. First, we carried out the drying process in the air to see the impact of an uncontrolled environment on perovskite crystallization. We applied two simple post-treatments: a fast-drying approach, where the printed film was placed directly on a hot plate ("HP_AIR"), and a second method with slower drying, where the printed sample was allowed to dry in air at room temperature before annealing on a hot plate ("AIR"). In both cases, the layers showed poor morphologies, characterized by nonuniform and noncompact large domains, as evidenced by top-view SEM images (**Figure 2**a,b).

In Figure 2c, we present X-ray diffraction patterns of perovskite films formed by fast and slow crystallization, both methods carried out in ambient air. The first sample shows two peaks, at 14°

and 28°, which are assigned to (111) and (202) planes, revealing a dominant out-of-plane growth of perovskite crystallites.[41] The presence of many additional peaks in the sample dried fast suggests more random orientations of perovskite grains. The full width at half maximum (FWHM) of (111) and (202) peaks is reduced, and the intensities are higher for the fast-drying sample ("HP_AIR"), which implies larger crystallite sizes in this variant. Fast crystallization directly on the hot plate resulted in the crystalline film with large grains, but with random orientations. Prolonged drying favors vertical growth, but the overall crystallinity of this film is low, which could be influenced by the presence of moisture in the air.[46] In Figure 2d we show the $J–V$ characteristics of the solar cells made with these films. The performance turned out to be very low, primarily due to poor morphologies and not enough level of grain orientation.

In order to exclude the impact of moisture and improve the nucleation characteristics, we decided to focus on a moisture-free drying environment. We designed a range of post-treatment protocols, where temperature and pressure were varied to provide conditions of varying solvent evaporation rates. We investigated the following methods:

1) hot plate annealing inside the nitrogen-filled glove box (HP_GB) – printed samples transferred directly to the hot plate inside the glovebox;
2) glovebox drying (GB) – printed samples transferred to the glovebox, and dried there at room temperature;
3) nitrogen drying outside of the glovebox (N_2) – printed samples dried under a stream of N_2;
4) vacuum drying (Vac) – printed samples placed in the glove box antechamber (pressure of about 10^{-3} bar);
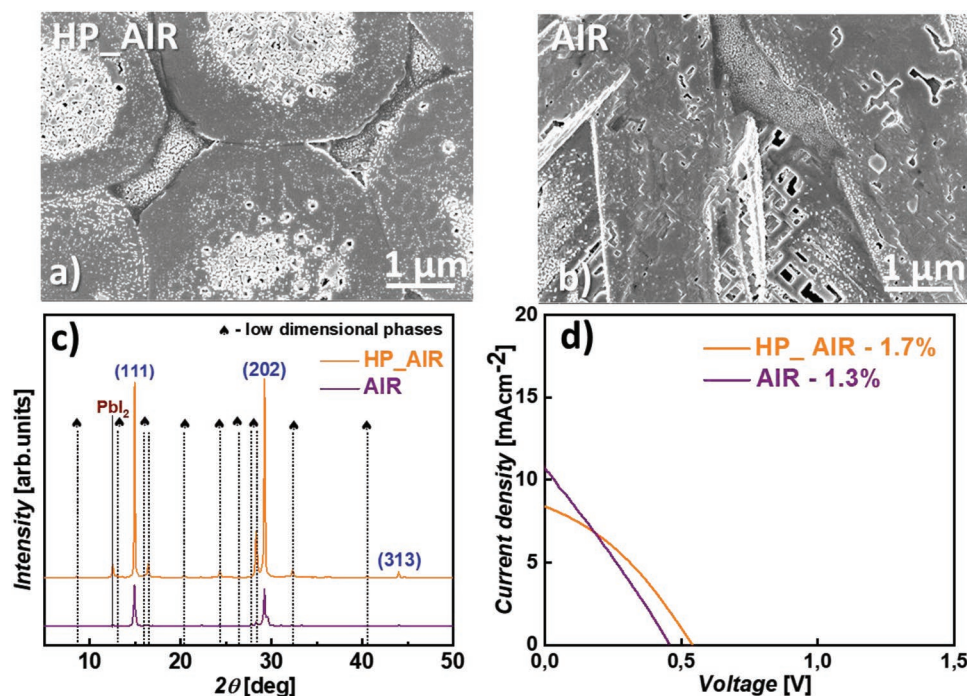

Figure 2. a,b) top-view SEM images of inkjet-printed perovskite layers, where (a) was annealed on a hot plate in ambient atmosphere, directly after printing, and (b) was dried in air for a few minutes, before hot plate annealing; c) X-ray diffractograms of both perovskite films; d) current density–voltage characteristics of solar cells embedding these two types of perovskite films.

**ADVANCED
SCIENCE NEWS**

www.advancedsciencenews.com

**ADVANCED
MATERIALS
TECHNOLOGIES**

www.advmattechnol.de

5) vacuum and nitrogen flushing in cycles (Vac+N$_2$) – printed samples placed in the glove box antechamber, which was evacuated and refilled with N$_2$, with a few repeating cycles.

In the first two methods ("HP_GB" and "GB") we varied the solvent evaporation rate by simply changing the temperature of drying, while the pressure was kept constant. Nitrogen blowing ("N$_2$") additionally speeds up solvent removal. Gas blowing is a widely used method of perovskite drying that provides high nucleation rates, with high density, leading to more compact perovskite layers.[47] In the next two methods, we applied reduced pressure for faster drying. The last protocol combined under pressure and nitrogen flushing to yield the fastest solvent removal, without changing the thermal budget of the deposit.

All the samples, which were dried under different conditions, were subsequently annealed at 100 °C on a hot plate, inside the glovebox, to obtain fully crystallized perovskite thin films. In **Figure 3**a–e, we show top-view SEM images of quasi-2D perovskite layers prepared with the described methods.

We observed that the layer crystallized very fast inside the glovebox ("HP_GB"), without a drying step, displayed quite similar morphology to the one dried outside ("HP_AIR"). Perovskite domains showed different shapes, but they were equally nonhomogenous and noncompact. Slow and steady solvent evaporation in the "GB" sample led to big domains and nonuniform layers, suggesting not sufficient nucleation density. Nitrogen blowing turned out to be an efficient way to accelerate evaporation, increasing the nucleation rate and leading to better coverage. These films still had numerous pinholes, which got reduced with the vacuum-based drying process. The most uniform and compact morphologies were obtained when the N$_2$ flow and vacuum treatments were combined. It is evident that in order to produce a dense perovskite layer,

high enough nucleation density and fast solvent removal need to be provided before the process of crystallite growth begins (thermal annealing).

Next, we carried out a detailed crystallographic analysis to understand the grain orientations in the studied quasi-2D perovskite thin film. The XRD patterns are shown in Figure 3f. We did not observe diffraction peaks in the region of $2\theta < 10°$ in the studied samples. This is the region where signature peaks of $(0k0)$ planes, which represent low n perovskite phases grown parallel to the substrate, are found.[48] We noticed that the perovskite film, which was annealed directly on the hot plate, shows multiple peaks in the diffractogram, which is an indication of random crystallite orientation (Figure 3f). In the other samples, only the two main reflections, (111) plane at 14° and (202) at 28° with varying intensities, are observed. This is an indication of preferred crystallite alignment in these films. In order to calculate the degree of preferred orientation, we first calculated the texture coefficient, specific for a particular set of planes. The texture coefficient is expressed by Equation (2)[49]

$$C_{hkl} = \frac{\frac{I_{(hkl)}}{I_{r(hkl)}}}{\frac{1}{z}\sum\frac{I_{(hkl)}}{I_{r(hkl)}}} \tag{2}$$

where $I_{(hkl)}$ is the peak intensity of the (hkl) plane of interest, $I_{r(i)}$ represents the intensity of the same peak in the reference spectrum from the XRD database, which we used to index the peaks in the patterns, and z stands for the number of (hkl) planes being taken into consideration for the calculation of the texture coefficient.

Diffraction patterns in Figure 3f show only three well-defined peaks, thus the z in the formula equals 3. We calculated
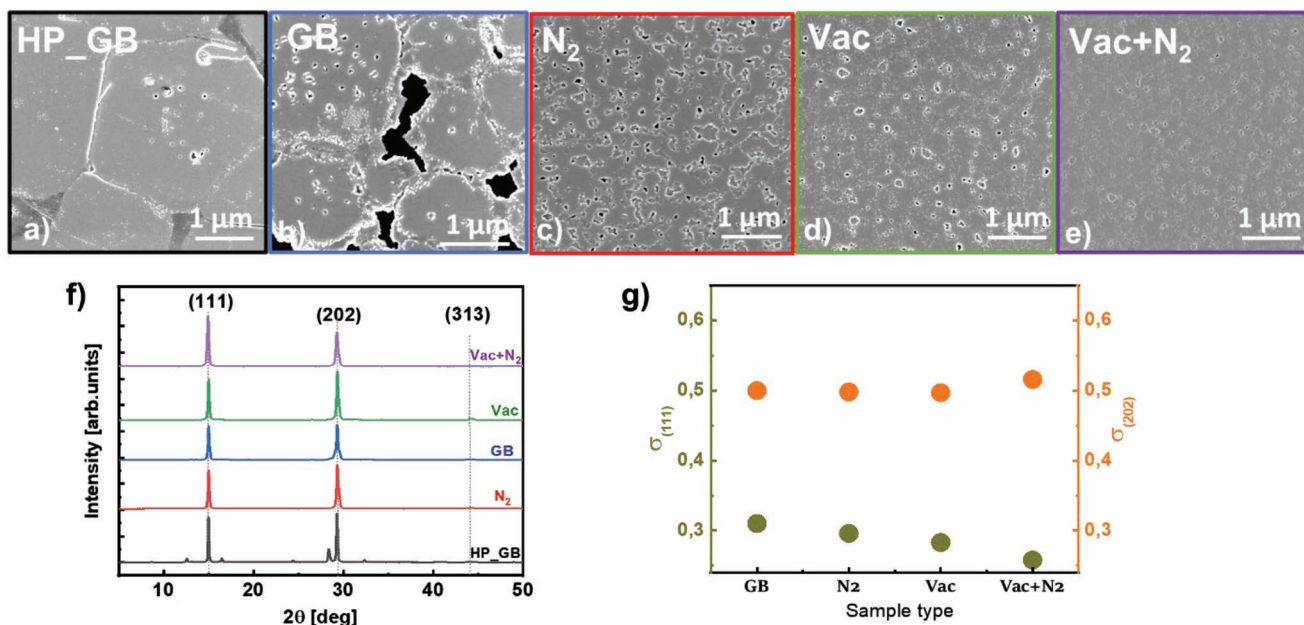
Figure 3. a–e) top-view SEM images of inkjet-printed perovskite layers, where a) was annealed on a hot plate inside the glove box, directly after printing, b) was dried at room temperature in the glove box before hot plate annealing, c) was dried under a stream of nitrogen, d) was dried under vacuum, and e) was dried under vacuum interrupted by nitrogen flushing; f) X-ray diffractograms of the listed types of perovskite films; g) degrees of preferred orientation for ⟨111⟩ and ⟨202⟩ directions, plotted for different drying methods of quasi-2D perovskite films.

**ADVANCED
SCIENCE NEWS**

www.advancedsciencenews.com

**ADVANCED
MATERIALS
TECHNOLOGIES**

www.advmattechnol.de

the texturing coefficients $C_{(111)}$ and $C_{(202)}$ for the (111) and (202) planes. Subsequently, we calculated the degree of preferred orientation of each film, given by Equation (3)[49]

$$\sigma = \sqrt{\frac{1}{z}\sum_z (C_{hkl} - 1)^2} \qquad (3)$$

The lowest possible value for σ is zero, which happens when $C_{(hkl)}$ equals one. This is the case when the studied sample shows completely random orientation. The value of σ increases with the higher degree of preferred orientation. Values of the texture coefficient and the degree of orientation purely depend on the number and intensity of peaks recorded in the XRD pattern. In Figure 3g we display the σ values, corresponding both, to the [111] and [202] directions, plotted for all the different perovskite films. We have excluded the "HP_GB" sample, which shows random crystallite orientation since this calculation is only applicable for the films with three reflections. The σ values for all the four samples processed in a controlled atmosphere show similar magnitudes for both directions. These results suggest that all the post-treatment strategies we applied turned out to be effective in inducing the out-of-plane alignment of the inorganic slabs. Within the plotted sample set, the "GB" variation shows the highest σ for the (111) plane and compared to other types, slightly lower value for the (202). Conversely, the film dried with the applied vacuum displays lower σ in the [111] direction. Moreover, the sample dried with both, N₂

and vacuum, has the lowest σ in the [111] and the highest in the [202] directions. This implies that the combined drying method results in the highest degree of crystallite growth perpendicularly to the substrate (straight out-of-plane orientation).

To get more insight into the influence of the drying conditions on the film formation principles, we employed different optoelectronic characterization techniques to study the properties of fabricated perovskite films. In Figure S5 (Supporting Information) we show UV–vis absorption spectra of all the samples. The absorption onset at around 760 nm, assigned to the bulk phase signal, is visible in all the cases. There are also observed higher energy peaks at 570, 610, and 646 nm, which relate to quasi-2D phases of n equal 2, 3, and 4, respectively.[50] The "HP_GB" sample is the only one showing qualitative differences, with a large contribution of the $n = 2$ phase at 568 nm. The higher n phases are not discernible in the spectrum. We also note that vacuum-based samples ("Vac" and "Vac+N₂") exhibit significantly enhanced absorptivity in the blue region, below 500 nm. It could be a result of improved morphology and higher crystallinity of all the phases in the film.[51] The PL spectra of the studied samples, applying perovskite-side and glass-side illumination, are shown in **Figure 4**a,b.

With our measurement setup, we were able to probe only the 3D-like bulk phase, which is centered around 770 nm in all the films. We can see from Figure 4a that the sample crystallized rapidly on the hot plate ("HP_GB") produced the lowest PL signal, which is in line with the lower crystallinity observed in
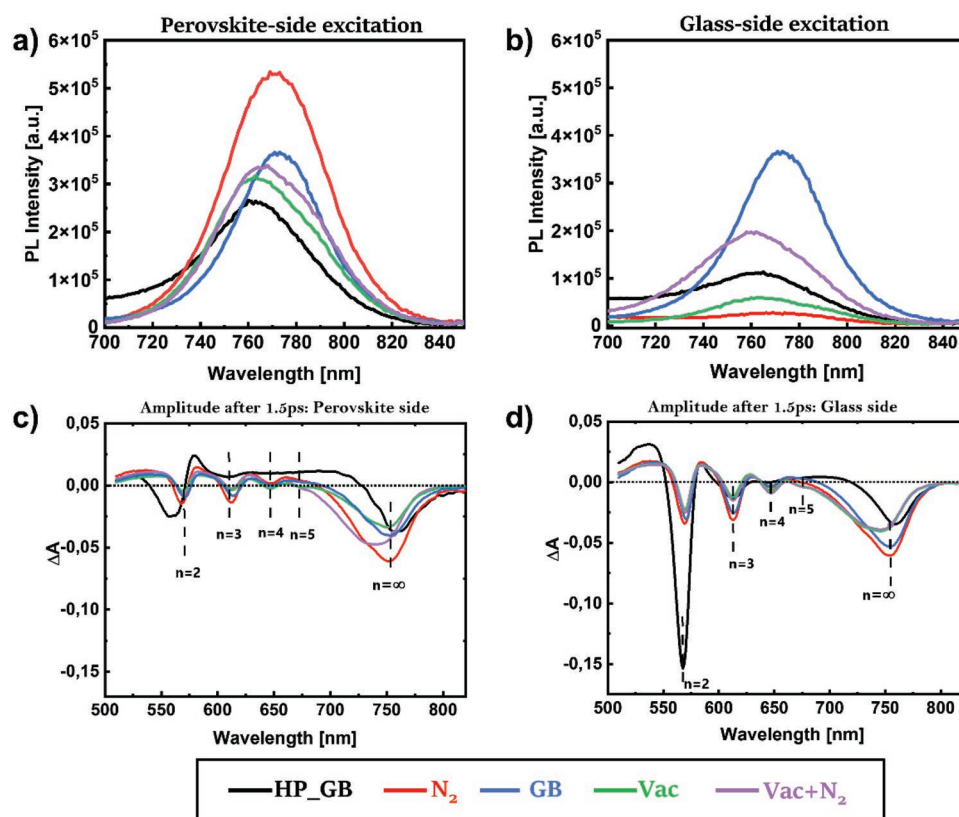

Figure 4. a,b) PL spectra of the inkjet-printed perovskite films, fabricated with different drying methods, where samples were excited a) through the perovskite-side, and b) through the glass-side; c,d) transient absorption spectra of the same perovskite sample types, measured at a time delay of 1.5 ps, with the c) perovskite-side, and d) glass-side excitation.

ADVANCED
SCIENCE NEWS

www.advancedsciencenews.com

ADVANCED
MATERIALS
TECHNOLOGIES

www.advmattechnol.de

XRD. The PL signal of the samples with the controlled drying (nitrogen flow, nitrogen atmosphere or vacuum) is enhanced at the perovskite-side excitation. Additionally, the signals from the "HP_GB", "Vac," and "Vac+N$_2$" samples are slightly blueshifted in respect to the rest, suggesting stronger contributions from different low dimensional phases.[34] When the same sample set was probed from the substrate (glass) side, most of the emission signals were much smaller (Figure 4b), which could indicate the nonuniform distribution of phases across the film or an effective hole extraction at the PTAA interface (PL quenching). In the "GB" sample, poor perovskite morphology (visible on the SEM image) and/or lower degree of vertical alignment could influence the efficacy of hole extraction by PTAA, which in turn results in a higher PL signal in the glass-side excitation. The sample dried by nitrogen flow shows the largest difference in the PL signal between perovskite-side and glass-side excitations, possibly due to the 3D-like phases predominantly forming at the surface and/or very effective quenching effect at the PTAA side.[24] Interestingly, the "Vac+N$_2$" sample shows a similar PL signal for both excitation sides, which could suggest a more even distribution of phases in this film, similarly to the observations reported by Zhang et al.[34] The lack of discernible low dimensional phases for either excitation side could be a result of low laser excitation power employed for these measurements (excitation wavelength: 405 nm, intensity: 5 mW cm^{-2}). Additionally, when 2D phases are well intermixed with 3D phases, there can be an effective PL quenching mechanism due to carrier (electrons and holes) transfer from a low n phase (higher energy gap) to a large n phase (lower energy gap). Evidences of this process taking place, indicating type I (straddling gap) heterojunction predominantly forming between perovskite domains of different energy gaps, were recently reported.[52,14] In order to gain more information about the presence of specific phases (low- and 3D-like phases) and their distribution in the layer, depending on the chosen drying method, we performed transient absorption spectroscopy (TAS) characterization. Again, the measurements were carried out with both, perovskite-side and glass-side excitations. The spectra for all the samples show several distinct photobleaching (PB) peaks, at 568, 610, 644, and 760 nm, which correspond to the phases of n equal 2, 3, 4, and ∞ (bulk, 3D-like phase), respectively.[50] The bleach corresponding to the $n = 5$ should be around 675 nm, but it cannot be clearly distinguished, as the signal partially overlaps with the tail of the bulk phase bleach. Charge carrier cooling to the conduction and valence band edges takes place on a sub-ps timescale, so due to a band-filling in the bulk phase, a sharp bleach signal appears after ≈1.5 ps.[53] We observe that the bleaches corresponding to the low n phases are more intense when probed from the glass side in comparison to the perovskite-side measurement (Figure 4c,d). Conversely, the bulk phase bleach is more intense when probed from the perovskite side for all the films. Such graded distribution, where low dimensional phases are most concentrated at the substrate, and their content reduces toward the film's surfaces, were often reported in the literature.[24,54] We calculated the proportion of each phase from the contribution of its corresponding bleach, using the method described by Quan et al.[55] The distribution analysis for all the studied samples is shown in Figure S6 (Supporting Information). The "HP_GB" sample

shows the largest gradient, with the $n = 2$ phase forming predominantly at the substrate/PTAA interface. For the other drying methods, the concentration of phases of n equal 3 and 4 shows the largest difference between the top and bottom parts of the layer. We also note that the application of vacuum in the drying process results in a higher percentage of high n phases ($n = 4$ and 5) in the film, which was reported to be beneficial for the transport of charges.[56] Furthermore, these high n phases are visible from both sides, suggesting an even distribution across the layer. This is observable for both, "Vac" and "Vac+N$_2$" sample types. A combination of nitrogen flushing and vacuum drying results in a slightly higher content of a 3D-like phase at the surface when compared to the vacuum-only protocol. Similarly to the PL data, there is a distinct blueshift of the bulk phase bleach for samples treated by vacuum, indicating a larger contribution of reduced dimensionality phases.[56]

The crystallization process can be divided into two stages: nucleation and crystallite growth. The nuclei formation is triggered by reaching a supersaturation state of a solid precursor, which subsequently leads to crystallite growth upon reaching the critical radius of the nucleus.[57] Perovskite thin-film crystallization typically occurs via heterogeneous nucleation, where foreign surfaces assist the process of phase transformation by decreasing the total free energy for forming a critical nucleus size.[58] Solvent evaporation increases the concentration of precursor solids, triggering the nucleation step. The concentration is then balanced by crystallite growth, which consumes the solids, lowering the supersaturation level. The rates of nucleation and crystal growth steps define the size and distribution of crystallites in the final layer. The competition between both processes is influenced by the size of colloids, their interactions, solvents, applied drying conditions (temperature, pressure), which drives the solvent evaporation, and thermal budget required to form crystalline phases.[59] In quasi-2D perovskite systems, the nucleation typically originates at the air-liquid interface, and the resulting phase distribution across the layer is influenced by the composition of Pb-based complexes in the precursor solution and solubility differences of the constituent iodides.[15,60] In our previous work, we demonstrated that 4F-PEAI has higher solubility in DMF than MAI. At the initial stage of nucleation, Pb-solvent complexes crash from the supersaturated solution and serve as nucleation centers.[48] During the subsequent crystal growth step, there are more MA$^+$ cations available to build the perovskite lattice, as they precipitate earlier from the solution. Then, with fewer MA$^+$ and more 4F-PEA$^+$ cations, the stoichiometry of grown crystals favors the low n phase composition. Overall, this results in a higher content of bulk phases at the surface.[15] The rate of solvent removal will impact the competition between small and large cations, and in turn phase composition across the film. More rapid nucleation should result in a more even distribution. We speculate that the application of vacuum enables selective and efficient DMF removal, promoting large nucleation density, without triggering a crystallization onset. At the pressure of 10^{-3} bar (used in this study), DMF evaporation at room temperature is quite rapid (DMF vapor pressure at 25 °C is 3.5×10^{-3} bar), whereas DMSO (vapor pressure of 8×10^{-4} bar) largely stays in the film.[61] This induces high supersaturation but does not lead to rapid crystallization. DMSO, due to

**ADVANCED
SCIENCE NEWS**

www.advancedsciencenews.com

**ADVANCED
MATERIALS
TECHNOLOGIES**

www.advmattechnol.de

its high coordination affinity, forms strong Lewis acid-base adducts with Pb, which constitutes an intermediate phase, and slows down the perovskite formation.[62] Zhang et al. reported a similar process, where vacuum-assisted drying was applied for the quasi-2D perovskite film formation.[34] It was shown that such a method led to a uniform distribution of phases across the film thickness, which improved charge carrier transport properties. Using vacuum was also reported to be beneficial for obtaining pinhole-free 3D perovskite layers.[62] The combination of vacuum and nitrogen flushing ("Vac+N$_2$") seems to provide optimal conditions for effective nucleation and controlled crystallite growth. This is reflected in the most uniform morphology, high level of texture in the out-of-plane orientation, and more uniform distribution of phases across the layer (moderate gradient, with larger content of high n phases). We note that the same post-annealing strategy was successfully applied for the 3D perovskite formation.[63] The beneficial effect of gas flow-assisted vacuum drying on perovskite nucleation, pointed out by the authors, is in agreement with our results for quasi-2D perovskite formation.

Having explored the properties of the printed quasi-2D perovskite thin films, in the next step, we fabricated photovoltaic devices with these layers and evaluated their PV performance. We utilized the same solar cell architecture, as used before, i.e., p–i–n configuration of the following stack: glass-ITO/PTAA/perovskite/C$_{60}$/BCP/Ag. We show J–V curves of the best cells of each type in **Figure 5**a. Statistics of the performance parameters, extracted from J–V curves, for a batch of devices prepared for each drying variation, we show in **Table 1** and Figure S7 (Supporting Information) (box plots).

The cells showed a large influence of the fabrication protocol (drying method) on the PCE values. Direct annealing on the hot plate and rapid crystallization ("HP_GB") resulted in the worst performance. As we showed above, introducing a drying step provides controlled crystal growth, and stimulates a high degree of vertical orientation (perpendicular to the substrate). This effect is reflected in significantly improved charge carrier transport characteristics, which in turn enables larger current densities and fill factor values. Morphological aspects, such as surface coverage, and layer uniformity, have also a critical influence on the performance parameters. Accelerated nucleation rates with the N$_2$ flow or vacuum, produced reasonably high PCE values, with the best performance obtained for the method combining these two techniques. Improved transport characteristics are also visible in external quantum efficiency (EQE) spectra, which were measured for the representative cells of each type. The spectra are shown in Figure S8 (Supporting Information). The "Vac+N$_2$" device exhibits the highest EQE, which is in good agreement with the highest J_{SC} values derived from the J–V measurements. In Figure S8 (Supporting Information) we provide integrated J_{SC} values, which are in good agreement with the J–V curves for all the device types.

To better understand differences in the charge carrier transport characteristics through the perovskite layers prepared with different drying conditions, we measured J_{SC} values as a function of the incident light intensity (varied from 1 sun to 0.01 sun by using optical density filters). The J_{SC} of a solar cell follows the power-law defined by $J_{sc} \propto P^{\alpha}$.[64] Therefore, a log–log plot

of the J_{sc} versus light intensity provides the exponent α, which reflects the magnitude of a photocurrent loss in the device.[65,66] In the ideal case, where there is no recombination loss (efficient carrier transport and collection), α equals 1. In a more realistic scenario, bimolecular recombination, space charge effects, or variations in carrier mobilities reduce α values below 1.[67] In Figure 5c we show the plots and α values for all the processing methods. Among the studied sample variations, the α parameter follows the same trend as the average J_{sc} values (see Table 1). The "Vac+N$_2$" and "Vac" samples display the highest α (0.98 and 0.97, respectively), which can be translated to a high carrier collection efficiency and good transport properties. The "GB" sample shows the lowest value ($\alpha = 0.88$), indicating significant carrier recombination before they can be efficiently extracted. The "N$_2$" device, with $\alpha = 0.92$, is positioned in the middle of the trend. These results clearly demonstrate that vacuum applied in the post-printing drying procedure results in the low dimensional perovskite phase formation, which gives the best transport characteristics through these layers. We also measured open-circuit voltage of the same devices, as a function of the incident light intensity (also varied from 1 sun to 0.01 sun) multiplied by J_{SC}. The results are given in Figure 5d. The slope of the linear fit is expressed as: $n_{ID}kT/q$, where k is Boltzmann constant, T is temperature, and q is the elementary charge. Dividing this number by the magnitude of kT/q at room temperature (0.026 mV) gives the ideality factor (n_{ID}) of a solar cell. For PSCs, ideality factors close to 1 often imply strong first-order nonradiative losses at the interface.[68] We obtained n_{ID} values between 1.65 and 1.78 for all the devices, which suggests a reduction of interfacial losses, and possibly higher contribution of the Shockley–Read–Hall (SRH) bulk recombination. The lowest n_{ID} value was recorded for the "Vac+N$_2$" cell type, which correlates well with higher average V_{OC} values measured for these devices, implying fewer nonradiative losses. We note that, except for the "GB" variant, the differences are rather small, which suggests a similar recombination profile in these solar cells. Overall, the best photovoltaic performance, which we obtained for the "Vac+N$_2$" sample, we attribute to the improved layer morphologies (the most uniform and compact films), high level of texture in the out-of-plane direction, and more uniform phase distributions, with the presence of low dimensional phases characterized by higher n values.

To demonstrate the attractiveness and versatility of the developed methodology, we applied the optimized quasi-2D perovskite processing (vacuum with N$_2$ flushing for post-printing drying method) to flexible devices, with large active areas (1 cm^2). As a substrate, we used polyethylene terephthalate (PET) foil, coated with the ITO electrode. In Figure S9 (Supporting Information) we show a top-view SEM image of such perovskite thin film. The morphology is very similar to the layers coated on a rigid substrate. We obtained comparable efficiency values to the glass-based cells. The champion device reached a PCE of 10.6%. The J–V curve of the best cell is shown in Figure 5e. The statistics of performance parameters for a batch of devices we show in Figure S10 (Supporting Information). Performance parameter values (best and average) are listed in the last row of Table 1.

Lastly, we investigated the reliability of inkjet printed quasi-2D perovskite solar cells. For this reason, we selected the best

ADVANCED
SCIENCE NEWS
www.advancedsciencenews.com

ADVANCED
MATERIALS
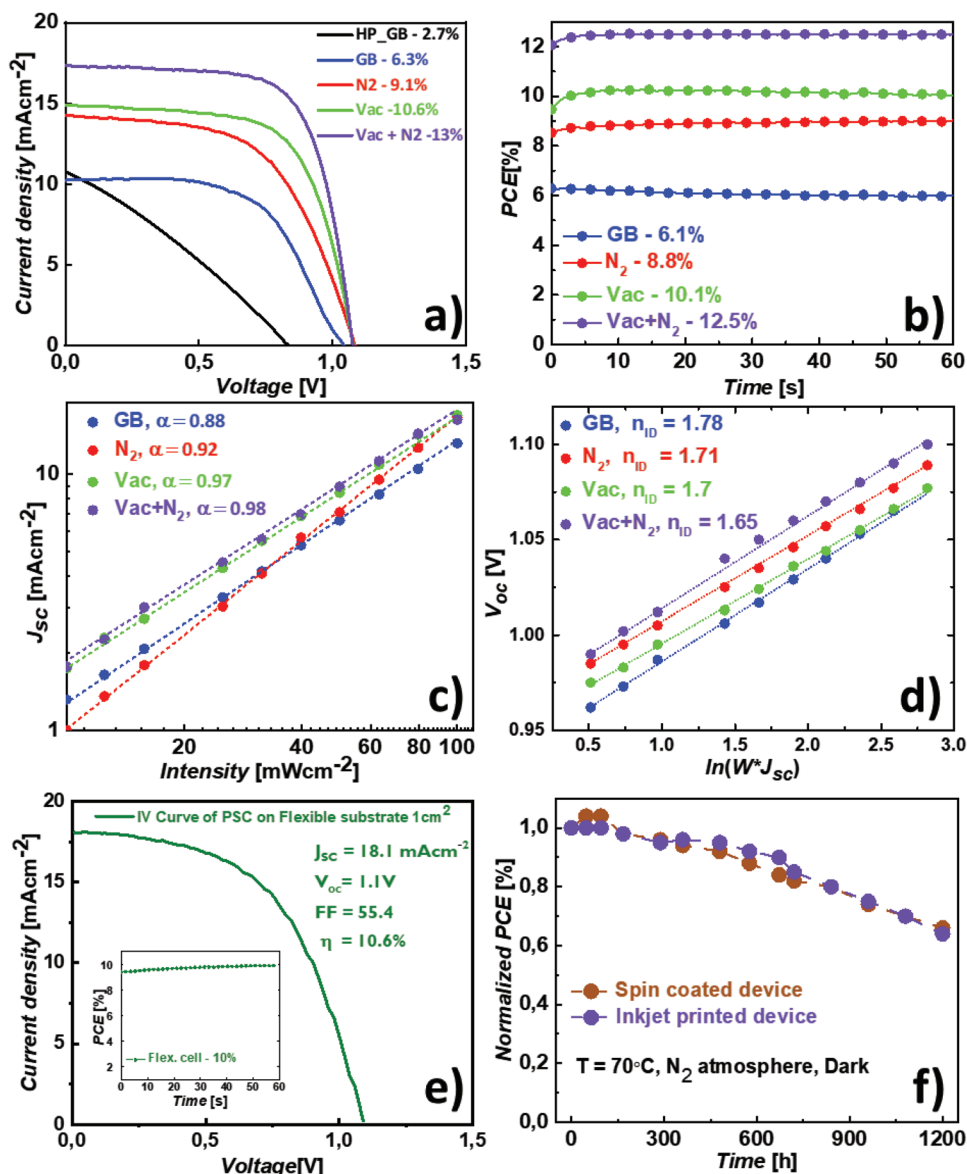TECHNOLOGIES
www.advmattechnol.de

Figure 5. a) Current density–voltage curves of the best quasi-2D perovskite solar cells, incorporating perovskite layers prepared with different post-printing drying methods; b) stabilized power output measurements of the same devices; c) J_{SC} and d) V_{OC} as a function of light intensity for the same devices; e) Current density–voltage curve and stabilized power output measurement (inset) of the best quasi-2D perovskite solar cell, prepared on a flexible substrate, with the large active area (1 cm^2); f) thermal stability test (70 °C ageing) of quasi-2D perovskite solar cells, with perovskite layers made by optimized spin coating and inkjet printing methods.

cells, fabricated with the optimized printing and drying protocols, and subjected them to the thermal stress at 70 °C, on a hot plate in the N$_2$ atmosphere. For comparison, we also added the best cell utilizing the spin-coated quasi-2D perovskite layer, which was described above. For this experiment, we modified a device architecture by replacing the BCP buffer layer with the SnO$_X$ film, which was deposited by atomic layer deposition (ALD). The ALD technique is capable of producing very thin, extremely dense, conformal, and pinhole-free coatings. For this reason, ALD-SnO$_X$ can act as an effective barrier, preventing ion migration between perovskite and metallic contact, which is a common device failure mechanism, reported for many different perovskite devices.[69] The time evolution of normalized

PCE values along the ageing test is plotted in Figure 5d. Both devices show comparable stability at 70 °C, retaining about 65% of their initial performance after 1200 h.

3. Conclusions

In summary, we have developed a precursor formulation, suitable for the inkjet printing process of quasi-2D perovskite thin films, with a general formula of 4F-PEA$_2$MA$_4$Pb$_5$I$_{16}$. We explored the influence of the post-printing drying conditions on the perovskite film characteristics. We found that high nucleation rates with simultaneously hampered crystallite growth

Table 1. Photovoltaic parameters extracted from the current density–voltage characterization measurements of quasi-2D perovskite solar cells, where inkjet-printed perovskite layers were prepared with different drying methods. The cells were made on glass (all variations) and PET (best drying protocol, large active area) substrates.

Cell type	$J_{sc}^{avg\pm SD}$(max) [mA cm^{-2}]	$FF^{avg\pm SD}$(max) [%]	$V_{OC}^{avg\pm SD}$(max) [V]	$PCE^{avg\pm SD}$(max) [%]
HP_GB	8.2 ± 0.9 (10.8)	33.8 ± 3.8 (36.9)	0.81 ± 0.01 (0.84)	2.3 ± 0.4 (2.7)
GB	10.2 ± 0.5 (10.1)	55.1 ± 1.8 (31.6)	0.97 ± 0.01 (1.03)	6.0 ± 0.4 (6.3)
N$_2$	12.7 ± 1.3 (15.9)	63.1 ± 2.5 (68.0)	1.00 ± 0.01 (1.11)	7.7 ± 0.9 (9.1)
Vac	15.0 ± 0.9 (15.9)	66.8 ± 6.0 (70.5)	1.05 ± 0.03 (1.10)	9.5 ± 0.7(10.5)
Vac+N$_2$	16.2 ± 1.5 (17.4)	68.4 ± 5.8 (73.0)	1.05 ± 0.03 (1.10)	12.4 ± 0.7 (13.0)
Vac+N$_2$ 1 cm^2 flex	17.13 ± 0.8 (18.1)	47.2 ± 5.6 (55.4)	1.06 ± 0.02 (1.10)	8.6 ± 1.2 (10.6)

can produce dense and uniform layers of the high level of out-of-plane alignment and more uniform distribution of low dimensional phases. We obtained this by applying vacuum and nitrogen flushing as a drying treatment, which triggered fast solvent evaporation. The presence of DMSO in the precursor solution, which forms stable Pb-based intermediates upon drying, enables subsequent, controlled crystallization of well-oriented perovskite phases. This optimized processing was applied to perovskite solar cells, which yielded PCEs of up to 13%. We also implemented the printing process to large-area (1 cm^2), flexible devices, reaching a PCE of 10.6% – one of the highest results for the quasi-2D perovskite thin films, which were processed on flexible substrates with a scalable technique. This study provides a valuable understanding of the formation principles of quasi-2D perovskite thin films and demonstrates inkjet as a feasible technique for a scalable coating of perovskite layers.

4. Experimental Section

Materials: All chemicals were used as received without any other refinement unless otherwise specified. Methylammonium iodide (MAI) and 4-fluoro-phenethylammonium iodide (4F-PEAI) were purchased from Lumtec, ammonium chloride (NH$_4$Cl), thiosemicarbazide (TSC), lead iodide (PbI$_2$, beads), fullerene C$_{60}$, and bathocuproine (BCP) were purchased from Sigma Aldrich. The prepatterned substrates with indium tin oxide (ITO) (<15 Ohms square^{-1}) were obtained from Lumtec. Poly[bis(4-phenyl)(2,4,6-trimethylphenyl)amine (PTAA) was purchased from Ossila. Silver (Ag) pellets were purchased from Kurt J. Lesker.

Device Fabrication and Film Processing: For spincoating, perovskite precursor solutions were prepared by mixing PbI$_2$, 4F-PEAI, and MAI in a stoichiometric ratio of 5.25:2:4.4, with a concentration of 0.7 M in DMF. The additives NH$_4$Cl and TSC were added in 20 mol% ratio and 5 mol% ratio with respect to PbI$_2$. The precursor solution was subjected to continuous stirring overnight at 70 °C.

For printing, perovskite precursor solutions were prepared by mixing PbI$_2$, PbCl$_2$, 4F-PEAI, and MAI in a stoichiometric ratio of 4.75:0.25:2:4.4, with a concentration of 0.7 M in a solvent mixture of DMF and DMSO (9:1 vol. ratio). TSC was added in 5 mol% ratio with respect to PbI$_2$. The precursor solution was subjected to continuous stirring overnight at 70 °C.

For spincoating, devices were prepared on conductive ITO-coated glass substrates. The substrates were cleaned extensively by deionized water, acetone and isopropanol in the mentioned order, for 10 min in each solvent. The hole transport layer solution was prepared by dissolving PTAA (20 mg) in anhydrous toluene (1 mL). The PTAA solution was spin-coated inside the glove box at 5000 rpm for 30 s at an acceleration of 1667 rpm s^{-1}. The spin-coated PTAA layer was then annealed inside the glove box at 100 °C for 10 min. Before perovskite processing, the

ITO/glass substrates were subjected to UV-ozone treatment for 15 min. 50 µL of the 2D perovskite precursor solution was spin-coated on top of the PTAA layer at 5000 rpm for 45 s, at an acceleration of 1000 rpm s^{-1}. After spincoating, the samples were allowed to dry inside the glovebox environment for about 15 min. After this, the dried layers were annealed at 100 °C for 15 min. 35 nm of C$_{60}$ was deposited on top of the perovskite films by thermal evaporation, followed by thermally evaporated 5 nm of BCP. Finally, 140 nm of Ag was deposited on top of BCP completing the device fabrication.

Inkjet printing of perovskite layers was performed at room temperature in the cleanroom conditions, with 25% relative humidity. The substrates and PTAA layers were prepared following the same procedure as for spin-coated devices. Before printing, O$_2$ plasma was used to treat the PTAA surface for about 45 s. A semi-industrial printer equipped with a commercial printhead with 512 nozzles was used, with all the nozzles active during deposition. The resolution of printing for all the samples was kept at 360 × 360 dots per inch (dpi). Right after deposition, printed films were subjected to drying and annealing procedures, which were described in the results section. The rest of the layers in the device structure was made according to the protocol described for the spincoated cells.

The ALD deposition of SnOx for samples subjected to ageing was carried out in a Beneq TFS-200 ALD reactor at 60 °C using tetrakis(dimethylamido)tin(IV) (TDMASn, Strem, 99%, heated to 45 °C) and water (at room temperature). The base pressure of the process was 1.2 mbar. The TDMA Sn pulsing of 1 s, TDMA Sn purging of 59 s, water pulsing of 100 ms and water purging of 35 s was used.

Characterization: Contact angle and surface tension of the inks were measured using optical tensiometer Theta Lite (TL100) equipped with One Attention software.

Viscosity measurements were carried out on Brookfield DV3T viscosimeter.

Measurement procedure was carried out as follows: 1 mL of ink was placed in the sample cup with the spindle. The speed of spindle rotation was adjusted to fit in the viscosity range of studied inks. In this work, the speed for all the inks was 70 rpm. The machine was equipped with a cooling system. The temperature of the ink (container) was set to 20 °C during the whole measurement.

UV–vis absorption spectra were obtained using the Edinburgh Instruments Spectrofluorometer FS5.

Current density–voltage characteristics and stabilized power output measurements were performed using a Keithley 2461 source measure unit (SMU) under simulated AM1.5G irradiation (100 mW cm^{-2}), using an AAA-rated solar simulator (Abet Technologies, sun 2000) calibrated against an RR-208-KG5 silicon reference cell (Abet Technologies). Solar cells on glass were masked to 0.06 cm^2. J–V measurements were performed in two scan directions, from −0.2 to 1.5 V (forward scan), and from 1.5 to −0.2 V (reverse scan). The scanning rate was set at 113 mV s^{-1}. The stabilized power output (SPO) was measured at the maximum power point voltage for a duration of 60 s.

Steady-state photoluminescence (ss-PL) measurements were performed with the Edinburgh Instruments FS5 Spectrofluorometer, equipped with a time-correlated single-photon counting (TCSPC) unit.

Samples were excited with a 405 nm laser diode (60 ps pulse, intensity: 5 mW cm^{-2}).

For transient absorption, ultrafast dynamics were determined using a broad-band transient absorption (TA) setup (Helios spectrometer, Ultrafast Systems, and Spectra-Physics laser system). The IRF (pump–probe cross-correlation function) was about 200 fs (full width at half-maximum), and transient absorption measurements were performed in the time range of up to 3 ns. One excitation wavelength was used: 490 nm and the spectra were probed in the range of 520–830 nm.

In scanning electron microscopy, top view images were obtained by employing a focus ion beam scanning electron microscope, FIB-SEM (FEI Helios 600), with an accelerating voltage of 2 kV. The samples were prepared by depositing carbon and platinum films on top of a sample.

XRD patterns were obtained using a Rigaku MiniFlex diffractometer

Supporting Information

Supporting Information is available from the Wiley Online Library or from the author.

Acknowledgements

Conflict of Interest

B.W., V.B., and K.W. are employees of Saule Technologies, a company commercializing flexible perovskite photovoltaic technology.

Data Availability Statement

The data that support the findings of this study are available from the corresponding author upon reasonable request.

Keywords

[1] National Renewable Energy Laboratory, Best Research- Cell Efficiencies, http://www.nrel.gov/ncpv/images/efficiency_chart.jpg (accessed: April 2022).

[2] H. Wang, Y. Wang, Z. Xuan, T. Chen, J. Zhang, X. Hao, L. Wu, I. Constantinou, D. Zhao, *Materials* **2021**, *14*, 6569.

[3] S. Zhang, G. Han, *Prog. Energy* **2020**, *2*, 022002,

[4] H. Tsai, W. Nie, J.-.C. Blancon, C. C. Stoumpos, R. Asadpour, B. Harutyunyan, A. J. Neukirch, R. Verduzco, J. J. Crochet, S. Tretiak, L. Pedesseau, J. Even, M. A. Alam, G. Gupta, J. Lou, P. M. Ajayan, M. J. Bedzyk, M. G. Kanatzidis, A. D. Mohite, *Nature* **2016**, *536*, 312.

[5] L. N. Quan, M. Yuan, R. Comin, O. Voznyy, E M. Beauregard, S. Hoogland, A. Buin, A. R. Kirmani, K. Zhao, A. Amassian, D. H. Kim, E. H. Sargent, *J. Am. Chem. Soc.* **2016**, *138*, 2649,

[6] R. Quintero-Bermudez, A. Gold-Parker, A. H. Proppe, R. Munir, Z. Yang, S. O. Kelley, A. Amassian, M. F. Toney, E. H. Sargent, *Nat. Mater.* **2018**, *17*, 900.

[7] F. Zhang, D. H. Kim, H. Lu, J.-S. Park, B. W. Larson, J. Hu, L. Gao, C. Xiao, O. G. Reid, X. Chen, Q. Zhao, P. F. Ndione, J. J. Berry, W. You, A. Walsh, M. C. Beard, K. Zhu, *J. Am. Chem. Soc.* **2019**, *141*, 5972.

[8] S. Maheshwari, T. J. Savenije, N. Renaud, F. C. Grozema, *J. Phys. Chem. C* **2018**, *122*, 17118.

[9] I. C. Smith, E. T. Hoke, D. Solis-Ibarra, M. D. Mcgehee, H. I. Karunadasa, *Angew. Chem., Int. Ed.* **2014**, *53*, 11232.

[10] S. Ramos-Terrón, C. Verdugo-Escamilla, L. Camacho, G. Miguel, *Adv. Opt. Mater.* **2021**, *9*, 2100114.

[11] X. Lian, J. Chen, Y. Zhang, S. Tian, M. Qin, J. Li, T. R. Andersen, G. Wu, X. Lu, H. Chen, *J. Mater. Chem. A* **2019**, *7*, 18980.

[12] Y. Wei, P. Audebert, L. Galmiche, J.-.S. Lauret, E. Deleporte, *Materials* **2014**, *7*, 4789.

[13] N. R. Venkatesan, J. G. Labram, M. L. Chabinyc, *ACS Energy Lett.* **2018**, *3*, 380.

[14] S. Sahayaraj, E. Radicchi, M. Ziółek, M. Ścigaj, M. Tamulewicz-Szwajkowska, J. Serafińczuk, F. De Angelis, K. Wojciechowski, *J. Mater. Chem. A* **2021**, *9*, 9175.

[15] W. L. Tan, N. M. Kirby, Y.-B. Cheng, C. R. Mcneill, *Nano Energy* **2020**, *83*, 105818, 2021.

[16] Y. Zhang, N. Park, *ACS Energy Lett.* **2022**, *7*, 757.

[17] J. W. Jung, S. T. Williams, A. K.-Y. Jen, *RSC Adv.* **2014**, *4*, 62971.

[18] B. Xia, Z. Wu, H. Dong, J. Xi, W. Wu, T. Lei, K. Xi, F. Yuan, B. Jiao, L. Xiao, Q. Gong, X. Hou, *J. Mater. Chem. A* **2016**, *4*, 6295.

[19] S. Rahimnejad, A. Kovalenko, S. M. Forés, C. Aranda, A. Guerrero, *ChemPhysChem 17*, **2016**, 2795.

[20] A. Z. Chen, M. Shiu, X. Deng, M. Mahmoud, D. Zhang, B. J. Foley, S.-.H. Lee, G. Giri, J. J. Choi, *Chem. Mater.* **2019**, *31*, 1336.

[21] J. E. Bishop, J. A. Smith, C. Greenland, V. Kumar, N. Vaenas, O. S. Game, T. J. Routledge, M. Wong-Stringer, C. Rodenburg, D. G. Lidzey, *ACS Appl. Mater. Interfaces* **2018**, *10*, 39428.

[22] Z. Liu, G. Liu, C. Xu, C. Xie, *Org. Electron.* **2021**, *102*, 106440, 2022.

[23] C. Zuo, A. D. Scully, D. Vak, W. Tan, X. Jiao, C. R. Mcneill, D. Angmo, L. Ding, M. Gao, *Adv. Energy Mater.* **2019**, *9*, 1803258.

[24] G. Wu, N. Ahmad, Y. Zhang, *J. Mater. Chem. C* **2021**, *9*, 9851.

[25] Y. Y. Kim, T.-.Y. Yang, R. Suhonen, A. Kemppainen, K. Hwang, N. J. Jeon, J. Seo, *Nat. Commun.* **2020**, *11*, 5146.

[26] B. Wilk, S. Öz, E. Radicchi, F. Ünlü, T. Ahmad, A. P. Herman, F. Nunzi, S. Mathur, R. Kudrawiec, K. Wojciechowski, *ACS Sustainable Chem. Eng.* **2021**, *9*, 3920.

[27] R. G. Sweet, *Rev. Sci. Instrum.* **1965**, *36*, 131.

[28] F. Mathies, E. J. W. List-Kratochvil, E. L. Unger, *Energy Technol.* **2019**, *8*, 1900991

[29] M. Singh, H. M. Haverinen, P. Dhagat, G. E. Jabbour, *Adv. Mater.* **2010**, *22*, 673.

[30] Y.-.L. S. Shao-Gang Li, K.-J. Jiang, M.-J. Su, X.-P. Cui, J.-H. Huang, Q.-Q. Zhang, X.-Q. Zhou, L.-M. Yang, *J. Mater. Chem. A* **2014**, *3*, 9092.

[31] D. Jang, D. Kim, J. Moon, *Langmuir* **2009**, *25*, 2629.

[32] A. Gheno, Y. Huang, J. Bouclé, B. Ratier, A. Rolland, J. Even, S. Vedraine, *Sol. RRL* **2018**, *2*, 1800191.

[33] H. Y. Park, B. J. Kang, D. Lee, J. H. Oh, *Thin Solid Films* **2013**, *546*, 162.

[34] J. Zhang, J. Qin, M. Wang, Y. Bai, H. Zou, J. K. Keum, R. Tao, H. Xu, H. Yu, S. Haacke, B. Hu, *Joule* **2019**, *3*, 3061.

[35] J. Euvrard, O. Gunawan, D. B. Mitzi, *Adv. Energy Mater.* **2019**, *9*, 1902706.

[36] B. Roose, K. Dey, Y.-H. Chiang, R. H. Friend, S. D. Stranks, *J. Phys. Chem. Lett.* **2020**, *11*, 6505.

**ADVANCED
SCIENCE NEWS**

www.advancedsciencenews.com

**ADVANCED
MATERIALS
TECHNOLOGIES**

www.advmattechnol.de

[37] Y. Chen, J. Hu, Z. Xu, Z. Jiang, S. Chen, B. Xu, X. Xiao, X. Liu, K. Forberich, C. J. Brabec, Y. Mai, F. Guo, *Adv. Funct. Mater.* **2022**, *32*, 2112146.

[38] Z. Li, Z. Chen, Y. Yang, Q. Xue, H.-.L. Yip, Y. Cao, *Nat. Commun.* **2019**, *10*, 1027.

[39] International Centre for Diffraction Data, https://www.icdd.com/ (accessed: December 2021).

[40] Y. Chen, Y. Sun, J. Peng, J. Tang, K. Zheng, Z. Liang, *Adv. Mater.* **2018**, *30*, 1703487.

[41] D. H. Cao, C. C. Stoumpos, O. K. Farha, J. T. Hupp, M. G. Kanatzidis, *J. Am. Chem. Soc.* **2015**, *137*, 7843.

[42] X. Li, J. M. Hoffman, M. G. Kanatzidis, *Chem. Rev.* **2021**, *121*, 2230.

[43] N. J. Jeon, J. H. Noh, Y. C. Kim, W. S. Yang, S. Ryu, S. Il. Seok, *Nat. Mater.* **2014**, *13*, 897.

[44] N. Ahn, D.-.Y. Son, I.-H. Jang, S. M. Kang, M. Choi, N.-.G. Park, *J. Am. Chem. Soc.* **2015**, *137*, 8696.

[45] G. H. Mckinley, M. Renardy, *Phys. Fluids* **2011**, *23*, 127101.

[46] M. K. Gangishetty, R. W. J. Scott, T. L. Kelly, *Nanoscale* **2016**, *8*, 6300.

[47] H. Hu, Z. Ren, P. W. K. Fong, M. Qin, D. Liu, D. Lei, X. Lu, G. Li, *Adv. Funct. Mater.* **2019**, *29*, 1900092.

[48] J. Wang, S. Luo, Y. Lin, Y. Chen, Y. Deng, Z. Li, K. Meng, G. Chen, T. Huang, S. Xiao, H. Huang, C. Zhou, L. Ding, J. He, J. Huang, Y. Yuan, *Nat. Commun.* **2020**, *11*, 1.

[49] G. Zoppi, K. Durose, S. J. C. Irvine, V. Barrioz, *Semicond. Sci. Technol.* **2006**, *21*, 763.

[50] H. Li, J. Lu, T. Zhang, Y. Shen, M. Wang, *ACS Energy Lett.*. **2018**, *3*, 1815.

[51] A. R. Pascoe, S. Meyer, W. Huang, W. Li, I. Benesperi, N. W. Duffy, L. Spiccia, U. Bach, Y.-B. Cheng, *Adv. Funct. Mater.* **2016**, *26*, 1278.

[52] A. Fakharuddin, M. Franckevičius, A. Devižis, A. Gelžinis, J. Chmeliov, P. Heremans, V. Gulbinas, *Adv. Funct. Mater.* **2021**, *31*, 2010076.

[53] T. C. Sum, N. Mathews, G. Xing, S. S. Lim, W. K. Chong, D. Giovanni, H. A. Dewi, *Acc. Chem. Res.* **2016**, *49*, 294.

[54] Y. Lin, Y. Fang, J. Zhao, Y. Shao, S. J. Stuard, M. M. Nahid, H. Ade, Q. Wang, J. E. Shield, N. Zhou, A. M. Moran, J. Huang, *Nat. Commun.* **2019**, *10*, 1008.

[55] L. N. Quan, Y. Zhao, F. P García De Arquer, R. Sabatini, G. Walters, O. Voznyy, R. Comin, Y. Li, J. Z. Fan, H. Tan, J. Pan, M. Yuan, O. M. Bakr, Z. Lu, D. H. Kim, E. H. Sargent, *Nano Lett.* **2017**, *17*, 3701.

[56] J. Cho, J. T. Dubose, P. V. Kamat, *J. Phys. Chem. Lett.* **2020**, *11*, 2570.

[57] M. Jung, S.-.G. Ji, G. Kim, S. Il. Seok, *Chem. Soc. Rev.* **2019**, *48*, 2011.

[58] S. Chen, X. Xiao, B. Chen, L. L. Kelly, J. Zhao, Y. Lin, M. F. Toney, J. Huang, *Sci. Adv.* **2021**, *7*, 26.

[59] A. Khaleghi, S. M. Sadrameli, M. Manteghian, *Rev. Inorg. Chem.* **2020**, *40*, 167.

[60] J. Hu, I. W. H. Oswald, H. Hu, S. J. Stuard, M. M. Nahid, L. Yan, Z. Chen, H. Ade, J. R. Neilson, W. You, *ACS Mater. Lett.* **2019**, *1*, 171.

[61] Sigma-Aldrich manufacturer, www.sigma-aldrich.com (accessed: April 2022).

[62] X. Li, D. Bi, C. Yi, J.-.D. Décoppet, J. Luo, S. M. Zakeeruddin, A. Hagfeldt, M. Grätzel, *Science* **2016**, *353*, 58.

[63] F. Mathies, E. R. Nandayapa, G. Paramasivam, M. F. Al Rayes, V. R. F. Schröder, C. Rehermann, E. J. W. List-Kratochvil, E. L. Unger, *Mater. Adv.* **2021**, *2*, 5365.

[64] V. D. Mihailetchi, J. Wildeman, P. W. M. Blom, *Phys. Rev. Lett.* **2005**, *94*, 126602.

[65] D. Bi, L. Yang, G. Boschloo, A. Hagfeldt, E M. J. Johansson, *J. Phys. Chem. Lett.* **2013**, *4*, 1532.

[66] L. J. A. Koster, V. D. Mihailetchi, H. Xie, P. W. M. Blom, *Appl. Phys. Lett.* **2005**, *87*, 203502.

[67] S. R. Cowan, A. Roy, A. J. Heeger, *Phys. Rev. B: Condens. Matter Mater. Phys.* **2010**, *82*, 245207.

[68] P. Caprioglio, C. M. Wolff, O. J. Sandberg, A. Armin, B. Rech, S. Albrecht, D. Neher, M. Stolterfoht, *Adv. Energy Mater.* **2020**, *10*, 2000502.

[69] K. O. Brinkmann, J. Zhao, N. Pourdavoud, T. Becker, T. Hu, S. Olthof, K. Meerholz, L. Hoffmann, T. Gahlmann, R. Heiderhoff, M. F. Oszajca, N. A. Luechinger, D. Rogalla, Y. Chen, B. Cheng, T. Riedl, *Nat. Commun.* **2017**, *8*, 13938.

6.Inkjet printing of functional layer for highly efficient perovskite solar cells

Barbara Wilk contribution:

- Adjusting the solution to meet the inkjet printing criteria. Optimization of ink concentration and solvents composition;
- Optimization of the printing process: waveform design; adjustment of printing parameters and post-processing;
- Performing the printing process;
- Supporting data analysis, layers characterization and I-V measurement of solar cells;
- Supporting manuscript writing.

New Fullerene Derivative as an n-Type Material for Highly Efficient, Flexible Perovskite Solar Cells of a p-i-n Configuration

Taimoor Ahmad, Barbara Wilk, Eros Radicchi, Rosinda Fuentes Pineda, Pierpaolo Spinelli, Jan Herterich, Luigi Angelo Castriotta, Shyantan Dasgupta, Edoardo Mosconi, Filippo De Angelis, Markus Kohlstädt, Uli Würfel, Aldo Di Carlo, and Konrad Wojciechowski*

Metal halide perovskites have raised huge excitement in the field of emerging photovoltaic technologies. The possibility of fabricating perovskite solar cells (PSCs) on lightweight, flexible substrates, with facile processing methods, provides very attractive commercial possibilities. Nevertheless, efficiency values for flexible devices reported in the literature typically fall short in comparison to rigid, glass-based architectures. Here, a solution-processable fullerene derivative, [6,6]-phenyl-C61 butyric acid *n*-hexyl ester (PCBC6), is reported as a highly efficient alternative to the commonly used n-type materials in perovskite solar cells. The cells with the PCBC6 layer deliver a power conversion efficiency of 18.4%, fabricated on a polymer foil, with an active area of 1 cm². Compared to the phenyl-C61-butyric acid methyl ester benchmark, significantly enhanced photovoltaic performance is obtained, which is primarily attributed to the improved layer morphology. It results in a better charge extraction and reduced nonradiative recombination at the perovskite/electron transporting material interface. Solution-processed PCBC6 films are uniform, smooth and displayed conformal capping of perovskite layer. Additionally, a scalable processing of PCBC6 layers is demonstrated with an ink-jet printing technique, producing flexible PSCs with efficiencies exceeding 17%, which highlights the prospects of using this material in an industrial process.

1. Introduction

Perovskite solar cells (PSCs) garnered a lot of attention within the scientific community over the last couple of years, thanks to their attractive commercial prospects.[1] The power conversion efficiency (PCE) reported for lab-scale devices recorded unprecedented progress, improving within one decade from a mere 3% to over 25%.[2,3] One of the great advantages of the perovskite technology over conventional photovoltaics (PV) is the possibility to fabricate PSCs on lightweight and flexible substrates.[4] This allows to attain very high specific powers and enables versatile, low-cost manufacturing methods.[5] New value propositions available for PSCs position this technology as a tangible solution for the emerging and rapidly growing PV markets, such as building-integrated PV (facades, windows, rooftops), automotive (vehicle integration), or internet-of-things (autonomous sensors, Industry 4.0).[6,7]

As PSCs are rapidly moving toward the industrial phase, there are still open questions about the prevailing architecture, choice of materials (including charge selective layers) and processing methodologies. In a commonly employed planar heterojunction perovskite solar cell architecture, perovskite film is sandwiched between two charge selective contacts—electron transporting material (ETM) and hole transporting material. Detrimental defects tend to form at both of these interfaces

T. Ahmad, Dr. R. Fuentes Pineda, Dr. P. Spinelli, Dr. K. Wojciechowski
Saule Technologies
Wroclaw Technology Park
Dunska 11, Sigma Building, Wroclaw 54-130, Poland
E-mail: konrad.wojciechowski@sauletech.com

T. Ahmad, L. A. Castriotta, Prof. A. Di Carlo
Centre for Hybrid and Organic Solar Energy (CHOSE)
Department of Electronics Engineering
University of Rome "Tor Vergata"
via del Politecnico 1, Roma 00133, Italy

The ORCID identification number(s) for the author(s) of this article can be found under https://doi.org/10.1002/adfm.202004357.

DOI: 10.1002/adfm.202004357

B. Wilk, S. Dasgupta, Dr. K. Wojciechowski
Saule Research Institute
Wroclaw Technology Park, Dunska 11, Sigma Building,
Wroclaw 54-130, Poland

E. Radicchi, Prof. F. De Angelis
Department of Chemistry, Biology and Biotechnology
University of Perugia
Via Elce di Sotto 8, Perugia 06123, Italy

E. Radicchi, Dr. E. Mosconi, Prof. F. De Angelis
Istituto CNR di Scienze e Tecnologie Chimiche "Giulio Natta"
(CNR-SCITEC)
Via Elce di Sotto 8, Perugia 06123, Italy

J. Herterich, Dr. M. Kohlstädt, Dr. U. Würfel
Fraunhofer Institute for Solar Energy Systems ISE
Heidenhofstraße 2, Freiburg 79110, Germany

with the perovskite layer, which leads to an increase of nonradiative recombination losses and deterioration of a solar cell performance.[8] Suitable chemical functionalization of perovskite's surface (different groups of ionic or covalent character) can eliminate or passivate some of these interfacial defects.[9] Additionally, interface chemistry can trigger various degradation mechanisms and it thus may affect device long term stability.[10] Therefore, charge selective contacts can be seen as pivotal PSC ingredients and their appropriate chemical design and layer formation are of fundamental importance for the optimal device operation and stability. So-called "inverted" PSC architecture (planar heterojunction of p-i-n configuration) is a popular option for fabricating devices on flexible, polymeric substrates.[11,12] This is primarily due to possibility of facile, solution-based processing, without high temperature annealing steps, and wide range of available charge selective materials. A range of different organic and inorganic materials have been used for electron extraction in PSCs.[13–15] Fullerene (C_{60}) and various fullerene derivatives were widely applied in efficient p-i-n devices due to their demonstrated effective electron extraction from the perovskite layer. Additionally, these organic materials allow low temperature thin film processing from solution on top of perovskite material, without causing any damage to the active layer. It was also reported that fullerene derivatives can play a passivating role in iodide-rich trap sites on the surface of perovskite layer.[16] Solution-processed fullerenes conformally cover the surface and permeate into the perovskite layer through the pinholes and grain boundaries, effectively reducing surface recombination. Xu et al. showed that mobile ions can interact with fullerene moiety and form a fullerene-halide adduct, which is thought to suppress the field-induced anion migration in the perovskite film.[17]

Phenyl-C61-butyric acid methyl ester (PCBM) is the most commonly used ETM in the perovskite solar cells of p-i-n configuration.[18] However, the PCBM-based contact can still limit the device performance, due to nonradiative recombination processes at the perovskite/ETM interface, and difficulties in smooth film formation, often resulting in a nonuniform layer morphology.[19–21] Several strategies of improving the PCBM film quality with different additives and dopants added to the fullerene solution were reported.[22,23] Particularly, insulating polymers, such as polystyrene (PS), poly(ethylene oxide), or poly(methyl methacrylate), when blended with PCBM at small weight percentage, lead to smoother morphologies and enhanced solar cell performance.[24–27] The caveat of this approach is limited carrier transport and extraction properties due to nonconductive character of the added polymer, which could result in another type of losses. Therefore, a more effective approach is highly desirable, where solution-processed, smooth, and inexpensive fullerene coating of high optoelectronic properties could be fabricated.

To solve these issues, in this work, we are reporting a fullerene derivative, [6,6]-phenyl-C61 butyric acid *n*-hexyl ester (PCBC6), employed as an effective electron transport material in perovskite solar cells of p-i-n configuration. PCBC6 exhibits higher solubility in nonpolar solvents due to the presence of a long alkyl chain group, which results in a more uniform and smoother film formation. Interfacial characteristics of perovskite solar cells employing different fullerene ETMs (PCBC6,

PCBM, and C_{60}) were analyzed and compared. Devices with PCBC6 exhibit improved power conversion efficiency, reaching 18.4% on flexible substrates, with an active area of 1 cm^2. This is exceeding the current state-of-the-art large area (above 1 cm^2) flexible PSC performance. To the best of our knowledge the highest PCE reported up to date for this type of devices is 20.01% (0.09 cm^2 active area) and 17.04% (1.08 cm^2 active area).[28,29] We found that the incorporation of PCBC6 leads to the reduction of nonradiative recombination losses at the interface with perovskite, as evidenced by transient photovoltage (TPV) decay measurements and determination of quasi-Fermi level splitting of perovskite layer brought in contact with different ETMs. Reduced interfacial losses result in open-circuit voltage (V_{OC}) improvement for the PCBC6 devices. Significantly, the newly developed material and processing method allow us to demonstrate scalable processing of flexible PSCs, reaching 17% with an ink-jet printed PCBC6. The overall concept paves the way for industrial upscaling of this technology.

2. Results and Discussion

Planar heterojunction thin-film solar cell architectures require an intimate contact between charge selective layer and a photoabsorber. In order to investigate the layer formation ability of different fullerene derivatives (PCBC6 and PCBM), we prepared chlorobenzene solutions and employed spin-coating as a deposition technique to fabricate thin films on the surface of a metal halide perovskite material. We investigated the morphologies of obtained layers with the atomic force microscopy (AFM) imaging and derived the root-mean-square (RMS) roughness of the studied films. PCBC6 sample shows the smoothest surface (RMS = 8 nm), significantly lower than the perovskite itself (RMS = 18.7 nm). Furthermore, the roughness of the PCBM sample processed in the same manner is considerably higher (RMS = 30.8 nm). The 3D surface topography images and cross-section focused ion beam scanning electron microscopy (FIB-SEM) images are shown in **Figure 1**. It is evident that the PCBC6 displays more conformal and uniform coverage over the perovskite surface than the PCBM sample. For the comparison, we also include images of the C_{60} layer thermally evaporated on top of perovskite surface. The roughness of this sample (RMS = 17.7 nm) is comparable to the bare perovskite, and cross-section FIB-SEM image depicts very uniform fullerene's coating, with complete coverage of perovskite surface. This is characteristic for a physical vapor deposition process, and such layer morphology should be beneficial for the device performance.

The PCBC6 ability to form smoother, more uniform layers could be a result of a higher tendency to form a more ordered and stable films, and more optimal precipitation dynamics during the spin-coating process. We compared the solubility of the two fullerene derivatives in a host solvent. The PCBM concentration of 50 mg mL^{-1}, both in chlorobenzene and 1,2-dichlorobenzene, resulted in an oversaturated solution (literature values for PCBM solubility: 40 mg mL^{-1} in chlorobenzene and 35 mg mL^{-1} in dichlorobenzene),[30] whereas PCBC6 exhibited solubility higher than 115 mg mL^{-1} in chlorobenzene. The pictures of both solutions are shown in Figure S1 in the

**ADVANCED
SCIENCE NEWS**

www.advancedsciencenews.com
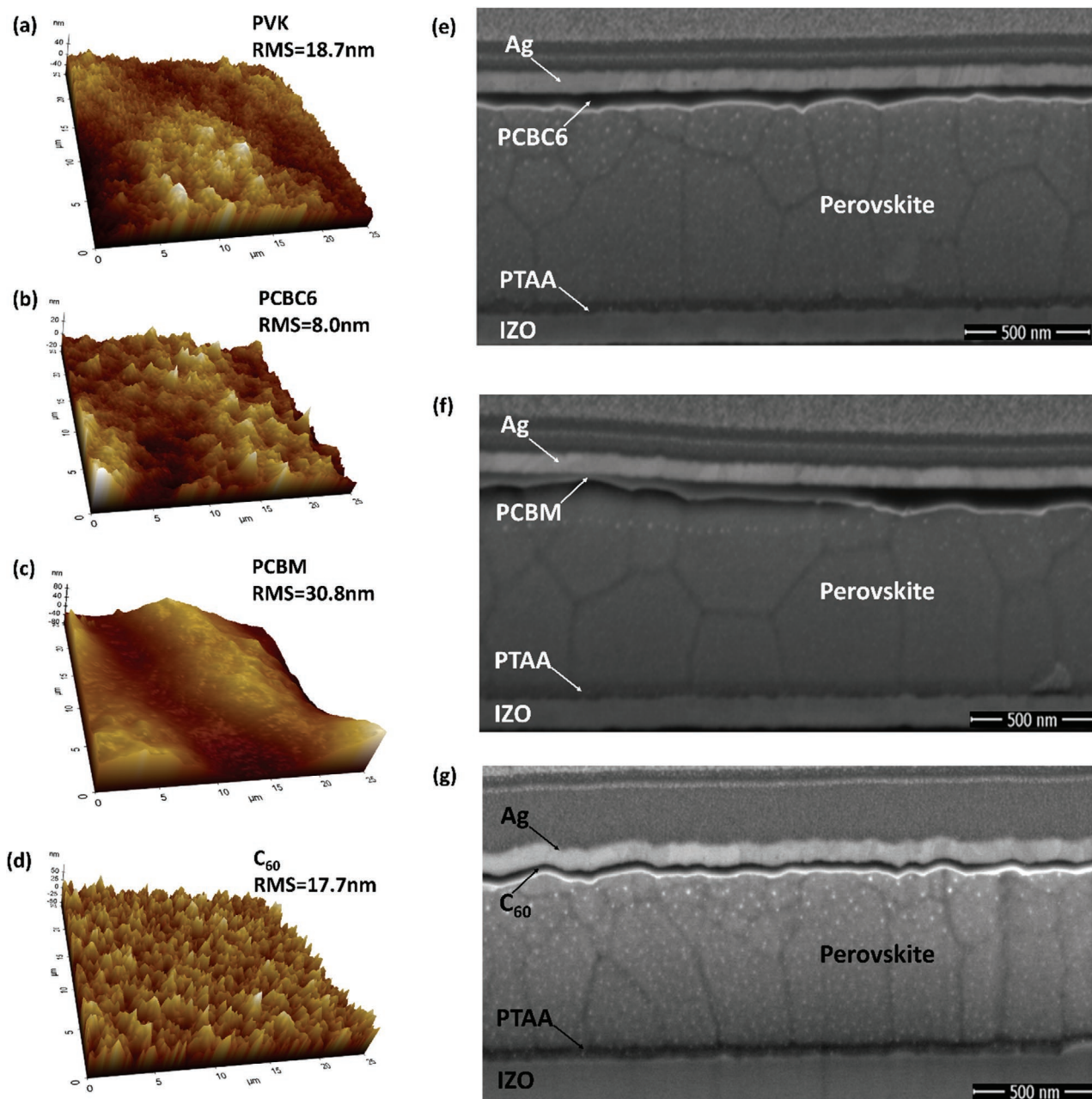
**ADVANCED
FUNCTIONAL
MATERIALS**

www.afm-journal.de

Figure 1. a–d) AFM 3D surface topography images (scanning range: 25 × 25 μm²) of a perovskite layer and perovskite coated with PCBC6, PCBM, or C$_{60}$ films. e–g) Cross-section FIB-SEM images of a perovskite layer coated with PCBM, PCBC6 or C$_{60}$ film.

Supporting Information. PCBC6 differs from the PCBM by a longer alkyl chain in the ester group. The structures of both molecules are shown in **Figure 2**. The hexyl group present in the PCBC6 results in a large increase of a solubilization ability in nonpolar solvents.[31] Additionally, it might increase the quality of the films in terms of stability, crystallinity, and homogeneous growth.

To gain insight into the packing properties of PCBM and PCBC6, we carried out first principles density functional theory (DFT) simulation to evaluate the intermolecular interaction characteristics of the two materials. We modeled the solid state

bulk phase of PCBM and PCBC6 molecules, employing periodic boundary conditions based on a 4-molecule unit cell (see Figure 2). As a starting point in both cases, we considered a structure that is available for PCBM from X-ray diffraction data, and we performed relaxation of cell parameters and atomic positions.[32] As we can see in Table S2 in the Supporting Information, the calculated cell parameters of PCBM are in excellent agreement with the experimental measurements confirming the reliability of the method. To evaluate the thermodynamic tendency of forming compact and homogenous film, we calculated aggregation energy between molecules in the bulk
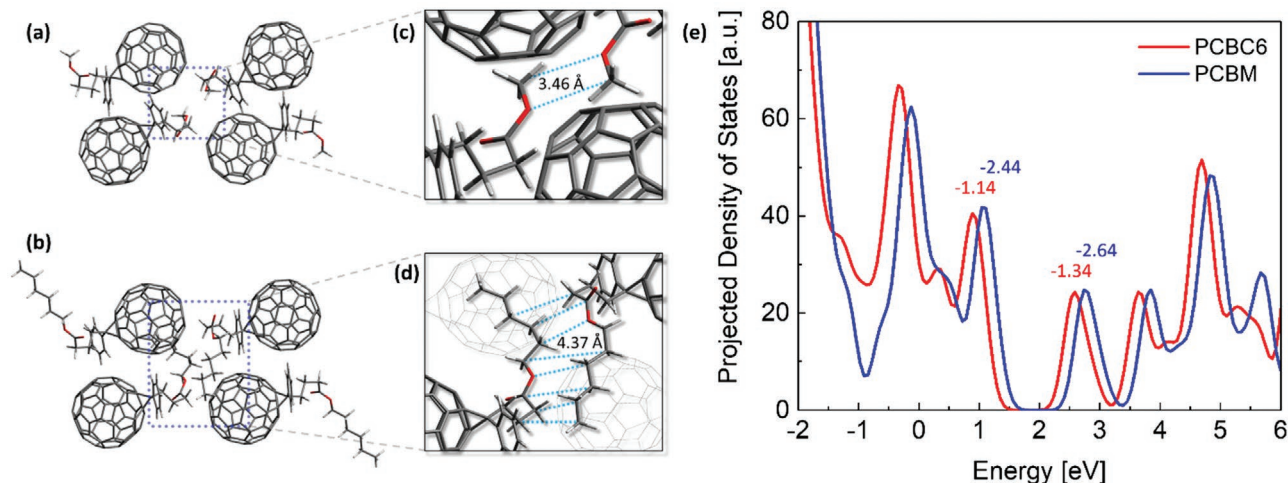
ADVANCED
SCIENCE NEWS
www.advancedsciencenews.com

ADVANCED
FUNCTIONAL
MATERIALS
www.afm-journal.de

Figure 2. Optimized geometry structure of a bulk a) PCBM and b) PCBC6 materials. Overview of the intermolecular interaction between the alkyl chains for c) PCBM and d) PCBC6 molecule along with the average distances in Å. e) Projected density of states of optimized bulk PCBM (in blue) and PCBC6 (in red) phases. The numbers in the inset indicate HOMO and LUMO energy values in eV.

by considering total energy of the system with respect to the energy of a single molecule, following the equation:

$$\Delta E = \frac{E_{\text{total}} - 4 E_{\text{single-molecule}}}{4} \tag{1}$$

where E_{total} is the total energy of the simulated system (consisting of four PCBM or PCBC6 molecules) and $E_{\text{single-molecule}}$ is the energy of the PCBM or PCBC6 molecule simulated in the same theoretical conditions.

We found that aggregation is preferentially favored for PCBC6, which gains additional 0.32 eV when compared to PCBM (see Table S2, Supporting Information). Stronger intermolecular interactions found for PCBC6 are related to its structure, where long alkyl chains are interacting through dispersion forces, as shown in Figure 2c,d. Specifically, as reported in Table S2 in the Supporting Information, these interactions completely drive the aggregation of our systems and imply preferred packing of PCBC6 with respect to PCBM (ΔE of −2.35 and −2.76 eV for PCBM and PCBC6, respectively). If only the electronic contributions were considered, it would give the opposite result (ΔE of 0.12 and 0.21 eV for PCBM and PCBC6, respectively). The higher aggregation tendency calculated for PCBC6 with respect to PCBM we associate with a tendency to form more uniform, smoother, and more stable film, due to the stronger intermolecular dispersion interactions that optimize its growth, as it was proposed by Benetto et al.[33]

Having established a rational interpretation of the different film morphologies for the investigated molecules, we move to analyze the electronic properties of both ETMs. The role of an ETM in perovskite solar cells is to extract photogenerated electrons and reflect holes. The electrons subsequently need to be efficiently transported to the electrode contact. The position of ETM's energy levels provides insights on the efficiency of electron extraction process. Therefore, we evaluated the projected density of states for both, PCBM and PCBC6 optimized bulk phase, as shown in Figure 2e. After the alignment of energetic levels to the lowest energy band, we can clearly see that the highest occupied molecular orbital (HOMO) and lowest

unoccupied molecular orbital (LUMO) levels of bulk PCBC6 are slightly lower than those of PCBM. In both cases, the distribution of states is nearly the same in the innermost levels of valence band; however, those of PCBM are slightly shifted to the higher energies. Conversely, for the isolated molecules we found almost no differences in the HOMO/LUMO energies between PCBM and PCBC6, as shown in Table S3 in the Supporting Information. This suggests that the modification of the electronic properties are not due to different chemical structures of both ETMs, but can be rather ascribed to the geometrical distortion induced by the molecular packing. Therefore, PCBC6 is well suited to selectively extract electrons from the perovskite layer from energetic point of view. In order to investigate the PCBC6 charge carrier transport properties, we performed electrical conductivity measurements. We prepared in-plane samples of fullerene layers processed on the polyethylene naphthalate (PEN)/indium tin oxide (ITO) substrates, where a 100 mm wide trench in the ITO layer was scribed with a laser. We extracted conductivity values from current–voltage curves (shown in Figure S3, Supporting Information). The PCBC6 conductivity of 6.58×10^{-5} S cm^{-1} is at the same range as the value obtained for PCBM, 4.68×10^{-5} S cm^{-1}. This is consistent with the PCBM conductivities reported in literature.[34]

2.1. Photovoltaics Devices

After demonstrating the basic feasibility of PCBC6 to be used as an ETM in perovskite solar cells, we constructed planar heterojunction devices of the p-i-n configuration, using different fullerenes as the n-type layers. We applied the following solar cell structure: Polyethylene terephthalate (PET)/indium doped zinc oxide (IZO)/poly[bis(4-phenyl)(2,4,6-trimethylphenyl) amine] (PTAA)/perovskite/ETM (varied)/bathocuproine (BCP)/ Ag. All the photovoltaic devices reported in this work, we fabricated on flexible substrates (PET foil), with 1 cm^2 device area. We chose to work with the polymer foils due to broad and attractive commercial prospects of flexible photovoltaics,
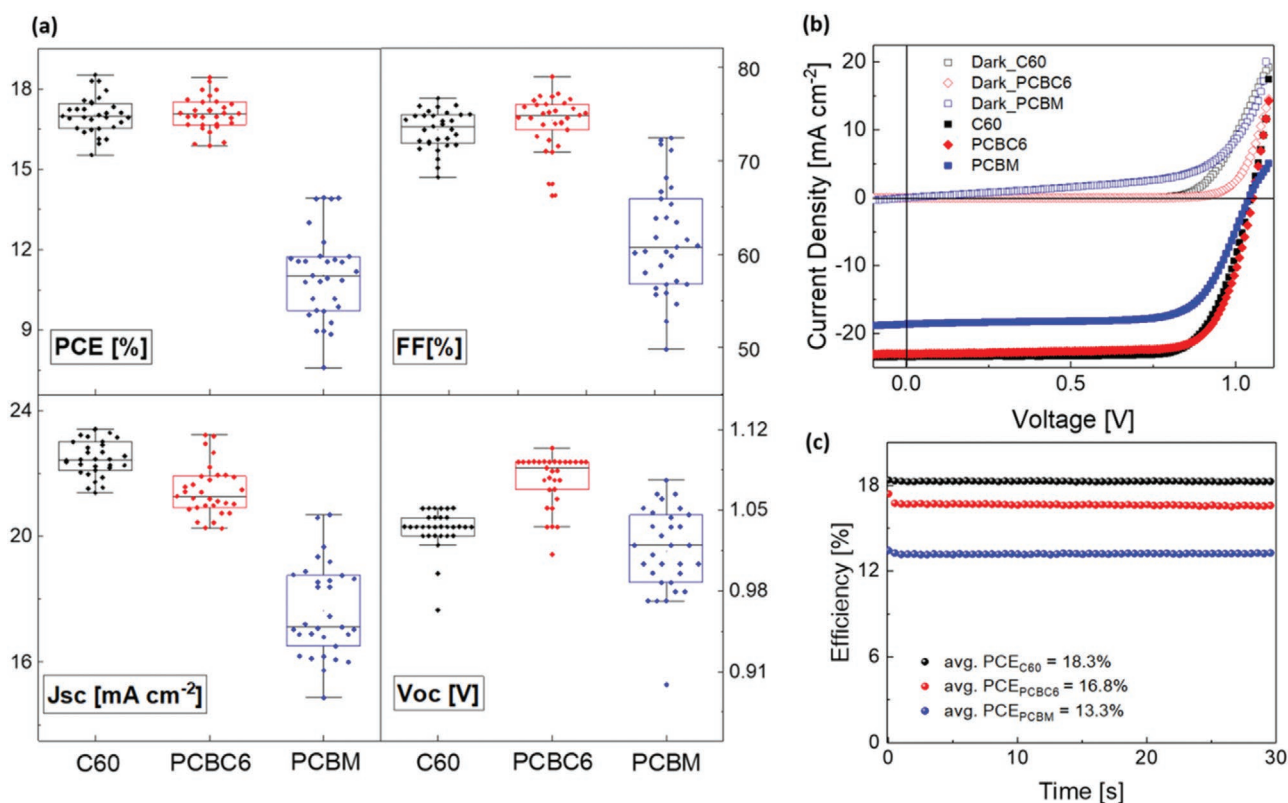
**ADVANCED
SCIENCE NEWS**
www.advancedsciencenews.com

**ADVANCED
FUNCTIONAL
MATERIALS**
www.afm-journal.de

Figure 3. a) Statistics of the photovoltaic performance parameters measured for the perovskite solar cells with different ETMs: evaporated C_{60} (black), solution-processed PCBC6 (red), and solution-processed PCBM (blue), b) current density–voltage characteristics (light and dark) of the best PSCs with different ETMs, and c) stabilized power output measurement of the same devices.

and particularly flexible perovskite PV. We employed a perovskite layer of the mixed cation and mixed halide composition, $Cs_{0.04}(MA_{0.17}FA_{0.83})_{0.96}Pb(I_{0.83}Br_{0.17})_3$, which we fabricated with a solvent engineering strategy, modifying a method reported before.[35] All the solution-based depositions were carried out by the spin-coating process inside the nitrogen-filled glovebox. In Figure S4 in the Supporting Information, we demonstrate the scheme of the device architecture with corresponding energy levels for each layer in the stack. Additionally, we show the cross-section FIB-SEM image of the solar cell, documenting all the materials in the device, and their thicknesses. For the reference, we fabricated perovskite solar cells with the two commonly used ETMs, evaporated fullerene C_{60}, and spin coated PCBM layer (processed from a dichlorobenzene solution).

We present the current density–voltage curves (J–V) and stabilized power output (SPO) of the most efficient devices employing different ETMs in **Figure 3**. The external quantum efficiency (EQE) spectra and integrated current density

values for each solar cell type are shown in Figure S5 in the Supporting Information. All the studied devices displayed minimal hysteresis effects. We present J–V curves in both scan directions for the representative cells in Figure S6 in the Supporting Information. In **Table 1** we report average values of the photovoltaic parameters extracted from the J–V curves, based on measurements of 31 independent cells, the parameters for the champion devices are given in brackets. The graphical representation of the statistics is shown in Figure 3a. The new fullerene derivative delivered the J–V-measured PCE of 18.4%. We observe that the SPO efficiency, measured at close to maximum power point, is lower, reaching 16.6%. For the reference device, employing solution-processed PCBM, we measured the PCE of 13.9%, and 13.3% SPO. The cell with the evaporated C_{60} yielded the PCE of 18.5%, and 18.3% SPO. Lower SPO value for the PCBC6 sample could be a result of pertaining areas with thinner PCBC6, or even noncomplete coverage where rougher perovskite surface structures occur (see Figure 1e).

Table 1. Photovoltaic parameters extracted from the current–voltage characterization measurements of the perovskite solar cells fabricated with different ETMs.

ETM	$J_{sc}^{avg \pm SD}$($J_{sc\ Best}$) [mA cm^{-2}]	FF $^{avg \pm SD}$(FF$_{Best}$) [%]	$V_{oc}^{avg \pm SD}$($V_{oc\ Best}$) [V]	PCE $^{avg \pm SD}$(PCE$_{Best}$) [%]
PCBC6	21.44 ± 0.78 (23.22)	73.98 ± 2.80 (76.14)	1.07 ± 0.02 (1.050)	17.08 ± 0.62 (18.41)
PCBM	17.63 ± 1.43 (20.59)	60.72 ± 5.83 (72.40)	1.01 ± 0.04 (1.035)	11.05 ± 1.59 (13.93)
C_{60}	22.48 ± 0.56 (23.42)	73.30 ± 2.03 (75.82)	1.03 ± 0.02 (1.043)	17.03 ± 0.68 (18.53)

The optimized PCBC6 thickness, which resulted in the highest J_{SC}, is relatively low, and local drop of charge selectivity and increased recombination can reflect in higher hysteresis and reduced SPO value.[36,37] In comparison, C_{60} layer is very thin, but highly conformal and uniform, with no thickness variations (see Figure 1g), as it was deposited by thermal evaporation process. Therefore, the SPO value shows a good match with the J–V-derived efficiency for this device.

It is evident that the cells with the solution-processed PCBC6 deliver higher V_{OC} than the C_{60} and PCBM-based devices. This observation points at the reduction of the nonradiative losses in this cell type. It can either originate from the more effective perovskite surface passivation by the fullerene moiety of PCBC6 molecules, or from suppressed recombination rates across the perovskite/ETM interface (without changing defect density on the perovskite side). The reduction of the perovskite trap state density by the fullerene-halide complex formation was reported before.[38] To investigate this hypothesis, we performed space charge limited current (SCLC) measurements of electron only devices. From the J–V curves, we extracted defect densities of perovskite devices with different ETMs processed on top (the curves are shown in Figure S7, Supporting Information). We estimated the smallest value of 1.01×10^{16} cm^{-3} for PCBC6, which compares to 1.91×10^{16} and 1.40×10^{16} cm^{-3} derived for C_{60} and PCBM, respectively. This is consistent with the reports of stronger perovskite passivation effect imposed by solution-processed fullerene molecules, which can possibly penetrate deeper into the film structure through the grain boundaries.[16] We note that these defect density values should be rather used for a comparative analysis, rather than precise quantitative determination of trap state population. It was recently reported that due to perovskite's ionic nature, the precise onset voltage where a device changes its operation mode can largely depend on the experimental conditions (voltage scan rate, scan direction, and temperature).[39] Nevertheless, considering that the perovskite fabrication process and SCLC measuring protocol in all three analyzed cases were exactly the same, observed differences we assign to surface phenomena caused by perovskite's interaction with different fullerene molecules. Surface passivation effects should have significant impact on nonradiative recombination processes occurring at that interface. We are providing further analysis of these processes with spectroscopic and electrical characterizations in the following sections.

Referring to the photovoltaic data compared in Table 1, we also point out higher short-circuit current-densities obtained for the C_{60} cells. The evaporated C_{60} layer is conformal and more uniform, with lower thickness variations across the sample than the solution-processed fullerene derivatives (PCBM and PCBC6), which are more affected by the perovskite surface roughness. This could influence the carrier extraction ability. The cells with the PCBM layer significantly lag behind the other two types. This is expected considering the poor layer formation of the PCBM film, as we showed with the AFM and FIB-SEM imaging. Highly nonuniform morphology results in a poor quality of the interface with the perovskite film. Thus, the efficacy of carrier extraction and carrier transport through the PCBM layer can be affected.

Furthermore, we point out a good reproducibility of the solar cell results, showing relatively low standard deviation of the performance parameters for the PCBC6 and C_{60} cell types. We highlight that our devices had larger active areas than typically reported in literature, and they were processed on a PET foil. It is significantly more challenging from the reproducibility and layer formation point of view.

2.2. Inkjet Printed PCBC6 Devices

In order to show the scalability of the PCBC6 processing, we employed an ink-jet printing technique for the fullerene deposition and applied it to the flexible perovskite solar cells of the same architecture as described above. We used PixDro LP50 printer, equipped with the Konica Minolta printhead. The printing settings we optimized with the resolution of 360 dots per inch (dpi). To deposit a fullerene layer with the ink-jet process, we adjusted an ink composition to obtain optimal drying profile and appropriate rheological properties (viscosity and surface tension) of the solution. The best drop formation and most uniform film quality of a desired thickness we obtained for the PCBC6 solution in chlorobenzene, with a small addition of octane. Cross-section and 3D surface topography images of the printed layers we are showing in Figure S8 in the Supporting Information.

Perovskite solar cells (flexible substrate, 1 cm^2 active area) with the optimized ink-jet printed ETM showed a very good photovoltaic performance, surpassing 17% PCE for the best device. We are showing the J–V curves (both scan directions) and steady-state measurement in **Figure 4**. We can observe negligible hysteresis in these cells, with a small difference between J–V and SPO-derived PCE values. Optimized ink-jet printed PCBC6 layers are thicker than spin-coated films, which result in a complete coverage of all the perovskite roughness (see Figure S8c, Supporting Information), and therefore hysteretic effects are minimized. The statistics of photovoltaic parameters of 15 devices using printed PCBC6 are shown in Figure S8a and Table S5 in the Supporting Information.

In the next step, within the range of studied fullerenes, we compare their ability to extract photogenerated electrons from the perovskite film, and the amount of interfacial nonradiative recombination occurring at that contact.

2.3. Interface Study

2.3.1. Quasi-Fermi Level Splitting

Determination of a QFLS in the photoactive layer was recently demonstrated as an effective way to assess the recombination losses at the perovskite interface with different charge selective materials. The QFLS can be derived from the photoluminescence quantum yield (PLQY) measurements.[40,41] The PLQY is generally influenced by all the different nonradiative recombination channels and rate constants of each of these processes in respect to a radiative recombination rate.[42] To probe the loss processes at the n-type contact, we measured the PLQY of perovskite films deposited directly on a glass substrate, and coated with different ETMs (bare perovskite, perovskite/PCBC6, perovskite/PCBM, and perovskite/C_{60}).
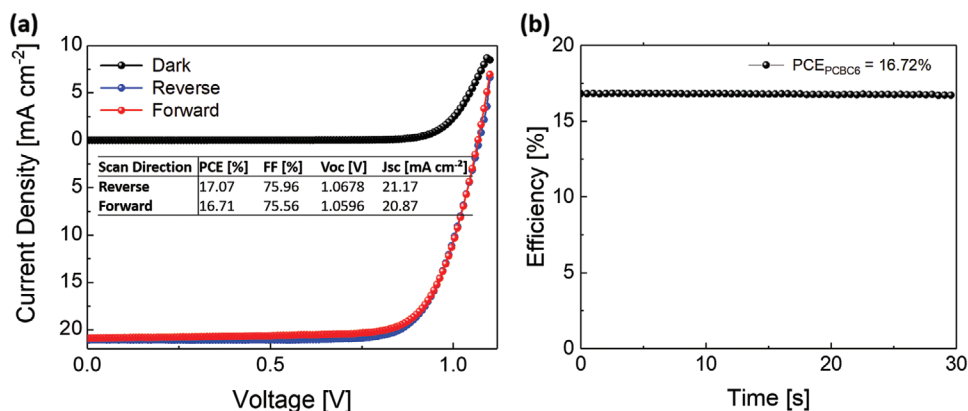
Figure 4. a) Current density–voltage characteristics of the flexible perovskite solar cell employing ink-jet printed PCBC6 (1 cm² active area) and b) steady-state power output measurement of the same device.

We are showing the measured photoluminescence (PL) spectra in **Figure 5**a. We can observe that the bare perovskite layer shows the highest PL intensity. Addition of the n-type layer partially quenches the signal, primarily due to increased nonradiative recombination at the perovskite/ETM interface.[43] The layer stack with the PCBC6 shows higher PL signal compared to other ETMs.

We extracted PLQY values from the PL spectra measured at low light intensity (excitation wavelength: 405 nm, intensity: 5 mW cm⁻²), using the embedded software tool of the spectrofluorometer, more details are provided in the Experimental Section. Then, we calculated the QFLS of the perovskite stacks following Equation (2).[44]

$$QFLS = QFLS_{rad} + kT \cdot \ln(PLQY) \tag{2}$$

where $QFLS_{rad}$ is the quasi-Fermi-level splitting in the radiative limit, k is the Boltzmann constant, and T is the temperature.

In the **Table 2** and Figure 5a, we provide the summary of PLQY values, together with the calculated QFLS, for the four cases described above. For the comparison, we also provide the average V_{OC} values determined from the J–V measurements of the respective photovoltaic devices. The bare perovskite layer shows the highest PL signal with the PLQY of 0.0366% (measured at 0.05 sun), which corresponds to the QFLS value

of 1.159 eV. The QFLS obtained for the PCBC6, PCBM and C₆₀ samples are 1.126, 1.093, and 1.089 eV, respectively. The samples containing PCBC6 as the n-type layer exhibit the highest device V_{OC} and the highest QFLS. This suggests that the voltage improvements recorded for the PCBC6 cells are strongly related to the reduced interface recombination at the n-type contact.

2.3.2. Photoluminescence Study

We extended the framework of the interface study by measuring the PL spectra of the complete perovskite solar cells with different ETMs (excitation wavelength: 532 nm, intensity: 100 mW cm⁻²), at two different working conditions: open-circuit (V_{OC} was also recorded) and short-circuit. We are showing the graphs in Figure 5b,c. The summary of V_{OC} values and integrated PL intensities are listed in **Table 3**.

We observe a clear trend, with the PCBC6-based device delivering the highest V_{OC}, followed by the C₆₀ cell type with 60 mV drop, and the PCBM sample with 130 mV drop in voltage in respect to the PCBC6 cell. This is consistent with the photovoltaic performance results presented in Figure 3. The integrated PL intensity follows the same order, being the highest for the PCBC6 and smallest for the PCBM cell type. When
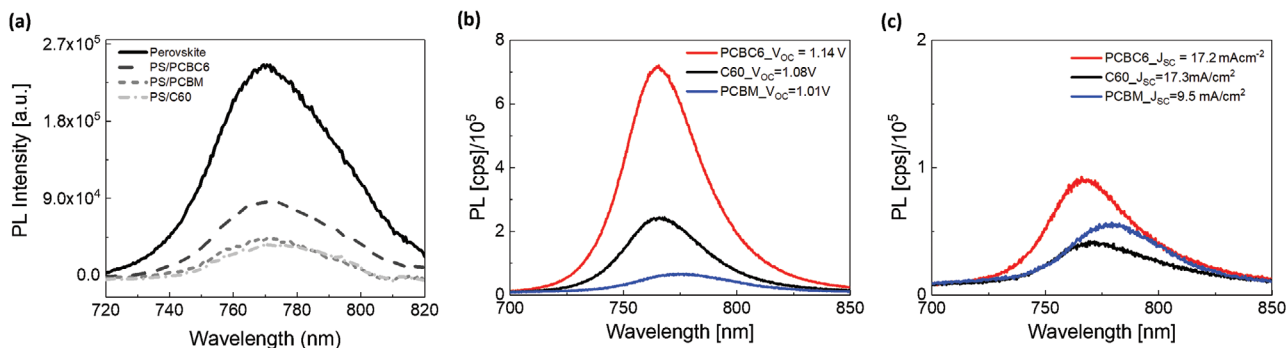

Figure 5. a) The PL spectra of perovskite samples (with and without different n-type layers) deposited on plain glass substrate. Spectral PL measurement of the flexible solar cells with different ETMs in b) open circuit and c) short circuit.

**ADVANCED
SCIENCE NEWS**

www.advancedsciencenews.com

**ADVANCED
FUNCTIONAL
MATERIALS**

www.afm-journal.de

Table 2. Summary of the PLQY and QFLS values determined from the spectroscopic measurements and V_{OC} values of respective solar cells obtained from the electrical measurements.

	PS	PS/PCBC6	PS/PCBM	PS/C$_{60}$
PLQY [%]	3.66×10^{-2}	1.02×10^{-2}	2.88×10^{-3}	2.47×10^{-3}
QFLS [eV]	1.159	1.126	1.093	1.089
Average V_{OC} [V]	–	1.07	1.01	1.03

Table 3. V_{oc}, J_{sc}, and spectrally integrated PL for the devices (in open-circuit and short-circuit) with C$_{60}$, PCBC6, and PCBM as ETMs.

Materials	Measurement in open circuit		Measurement in short circuit		
	V_{OC} [V]	PL-intensity [cps]	J_{SC} [mA cm^{-2}]	PL-intensity [cps]	PL quenching [$(V_{OC} - J_{SC})/V_{OC}$]
PCBC6	1.14	1.5×10^{8}	17.2	2.8×10^{7}	0.81
C$_{60}$	1.08	5.7×10^{7}	17.3	1.7×10^{7}	0.70
PCBM	1.01	2.3×10^{7}	9.5	2.0×10^{7}	0.13

we switch the solar cell working point from the open-circuit to short-circuit condition, photogenerated charge carriers are being extracted. Thus, the PL quenching monitored at this condition can be used as a measure of the carrier extraction ability for each device type. Both C$_{60}$ and PCBC6-based devices show high PL quenching which indicates their high charge carrier extraction efficacy. We should point out that the spin-coated PCBC6 film is likely to display larger inhomogeneity and thickness variations than evaporated C$_{60}$ layers. This could contribute to the fact that the C$_{60}$-based cell type also displayed the highest average short-circuit current density, as shown in Figure 3a. Higher inhomogeneity of the PCBC6 cell could lead to a slower rate of the charge transfer across the perovskite interface in the regions where PCBC6 layer is too thick. This could explain larger differences in the PCE values derived from the J–V and SPO measurements, which we pointed out above. It was reported before that interfacial extraction barriers in a perovskite solar cell could contribute to the hysteresis effect and reduced steady-state power output.[45] The direct link between optical and electrical measurements provided here strongly suggests that the PCBC6-based device displays reduced non-radiative recombination at the n-type interface, possibly due to perovskite surface passivation effect.

2.3.3. Transient Photovoltage and Transient Photocurrent (TPC) Study

In order to further corroborate the analysis of the perovskite interface with the selected n-type materials, we performed TPC

and TPV measurements. The TPC measurement was performed in a high perturbation regime, which means that the cell went from dark to a specific illumination set by the light emitting diode (LED) excitation light source. We applied ten different light intensities, ranging from 30 to 160 mW cm^{-2} (the details are provided in Table S1, Supporting Information). The cell was kept in the short-circuit condition during the entire measurement. The decay of current density was monitored over time after switching off the light. We integrated the current density time decay to obtain the extracted charge density. **Figure 6**a shows the charge density values derived at different perturbation light intensities. We can observe that the cell with C$_{60}$ layer exhibits slightly improved carrier extraction efficacy in comparison to the PCBC6 and PCBM types, especially at lower light intensities. This is consistent with the spectroscopic data discussed above. It could originate from the deeper LUMO level of the C$_{60}$ molecule when compared to the PCBM/PCBC6.[45] The TPV measurement was performed in a small perturbation regime. The cell was kept at open-circuit, with a specific background illumination applied from the LED light source. Then, a small overcurrent was sent to the LED to create a voltage perturbation (20 mV), which decay was subsequently monitored. Figure 6b displays the extracted recombination lifetimes derived from fitting voltage decay curves for different light intensities. The PCBC6 cell type exhibits the longest lifetimes (slower recombination) throughout the majority of used light intensity range. The C$_{60}$ device shows the fastest recombination, especially at the lower light intensity. Again, the transient decay results agree very well with the photoluminescence studies presented above.
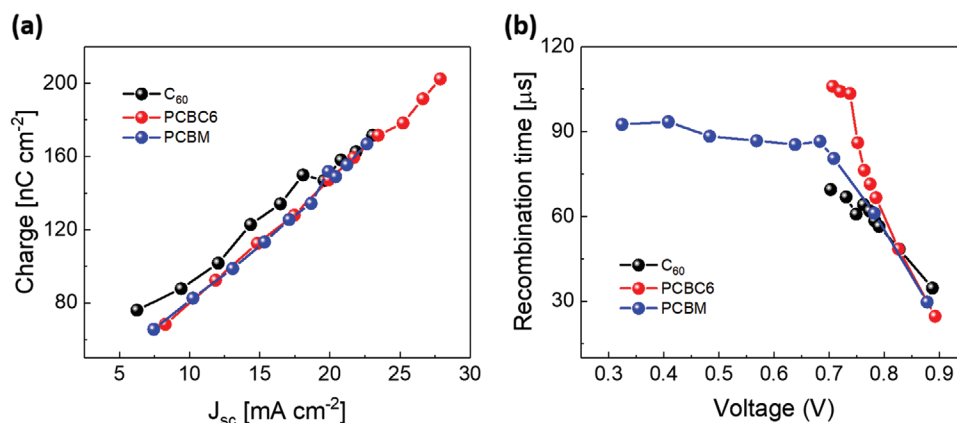

Figure 6. The analysis of the TPC/TPV measurements of PSCs with the different ETMs. a) Charge density extracted from the photocurrent decay measurements, plotted as a function of a short-circuit current density, which corresponds to varied perturbation light intensities. b) Recombination lifetimes derived from the fitting of photovoltage decay, plotted as a function of an open-circuit voltage at varied background light intensities.

**ADVANCED
SCIENCE NEWS**
www.advancedsciencenews.com

**ADVANCED
FUNCTIONAL
MATERIALS**
www.afm-journal.de

3. Conclusions

In summary, we have demonstrated a solution-processible fullerene-derivative, PCBC6, as an efficient electron transport material in perovskite solar cells of p-i-n configuration. Flexible devices of relatively large active areas (1 cm²), employing $Cs_{0.04}(MA_{0.17}FA_{0.83})_{0.96}Pb(I_{0.83}Br_{0.17})_3$ perovskite composition reached PCE values of up to 18.4% with the PCBC6 n-type layer. This is nearly 30% higher than the best performance obtained for the cells employing PCBM layer. By applying different imaging techniques, we have shown that this difference in large part can be assigned to significantly improved film morphology, thanks to higher solubility of PCBC6, and its stronger intermolecular interactions. Additionally, we have demonstrated facile scalable deposition of PCBC6 layers by applying ink-jet printing technique. The cells with printed PCBC6 films reached efficiencies above 17%. Through various spectroscopic and electrical characterization methods we have provided detailed analysis of the character of the interface between perovskite and selected n-type layers. Notably, PCBC6-based devices display reduced nonradiative recombination losses, as compared to C_{60} and PCBM cell types. This is consistent with higher open-circuit voltages recorded for PCBC6 samples. The caveat of PCBC6 material seems to be nonideal electron extraction efficacy, resulting in lower short-circuit current densities when compared to thinner and more uniform C_{60} films (thermally evaporated). It was recently discussed that majority carrier mobility of the organic interlayer in perovskite solar cells can limit the driving force for photocurrent generation in the case of low built-in potential.[46] Therefore, suitable PCBC6 doping strategy constitutes an interesting outlook for further improvement of this interface.

4. Experimental Section

Materials: PET substrates coated with IZO (sheet resistance of 15 Ω □⁻¹) were bought from Eastman Chemical Company, formamidinium iodide (FAI) was bought from Ajay North America, PTAA was bought from Osilla, [6,6]-phenyl-C61 butyric acid *n*-hexyl ester (PCBC6) was bought from Nano-C, and methylammonium bromide (MABr) was synthesized at Saule Technologies following the previously reported method.[47] All the rest of materials were purchased from Sigma-Aldrich and used as received without further purification.

Device Fabrication: Planar heterojunction flexible PSCs were fabricated with the following architecture: PET/IZO/PTAA/$Cs_{0.04}(MA_{0.17}FA_{0.83})_{0.96}$-$Pb(I_{0.83}Br_{0.17})_3$/PCBC6/BCP/Ag. PET/IZO (15 Ω □⁻¹) substrates were cut (18 × 13 mm² pieces) and patterned by dipping one side in the HCl solution (15 wt% in deionized (DI) water). The etched substrates were then sonicated in DI water and isopropanol. Before layer processing, 30 s of oxygen plasma treatment was applied. PTAA solution (2 mg mL⁻¹ in toluene) was spin coated under ambient conditions at 5000 rpm for 30 s, followed by annealing at 100 ℃ for 10 min, resulting in a ≈20 nm film. Subsequently, the samples were transferred into a nitrogen-filled glovebox for the perovskite layer deposition. The perovskite precursor solution composed of mixed cations and halides was prepared according to the procedure reported before.[48] First, stock solutions of PbI_2 and $PbBr_2$ (1.5 M) in dimethylformamide (DMF)/dimethyl sulfoxide (DMSO) mixture (4:1 v/v) were prepared. Then, for $FAPbI_3$ and $MAPbBr_3$ solutions, FAI and MABr powders were weighed out into separate vials, followed by addition of PbI_2 (into FAI) and $PbBr_2$ (into MABr) solutions. Both lead solutions were added in excess, to obtain an over stoichiometric lead content (FAI/MABr: PbI_2/$PbBr_2$ equals 1.0:1.09). The final perovskite precursor solution was prepared by mixing the

solutions of $FAPbI_3$ and $MAPbBr_3$ in a 5:1 v/v ratio. Then, 40 μL of CsI solution (1.5 M solution in DMSO) was added to 1 mL of the mixture. Perovskite layer (≈580 nm thick) was deposited on top of PTAA with a two-step spin-coating procedure, 1500 rpm for 2 s and 5000 rpm for 34 s. Anhydrous ethyl acetate (150 μL) was dispensed on the sample at the 11th second before the end of the spinning sequence. Then, the sample was kept at rest for 1 min before transferring to the hotplate for the two-step annealing process, 1 min at 60 °C and 60 min at 100 °C. The electron transporting layers were deposited by spin coating (PCBC6 or PCBM) or thermal evaporation (C_{60}). PCBC6 solution (20 mg mL⁻¹ in chlorobenzene) was spin coated at 4000 rpm for 30 s, and PCBM solution (20 mg mL⁻¹ in ortho-dichlorobenzene) was spin coated at 2000 rpm for 30 s. The solution-processed ETMs were annealed for 10 min at 60 ℃. Finally, 8 nm of BCP buffer layer and 100 nm of Ag electrode were deposited on top of devices by thermal evaporation at ≈10⁻⁶ mbar, through a shadow mask.

PCBC6 Ink Preparation and Ink-Jet Printing: PCBC6 was dissolved in chlorobenzene (10 mg mL⁻¹), followed by sonication for 10 min. The solution was then diluted with octane (1 mL of octane for 6 mL of PCBC6 solution). The ink was filtered with a 0.22 μm polytetrafluoroethylene (PTFE) filter before use. Ink-jet printing was done with a PixDro LP50 printer, equipped with a Konica Minolta printhead (512 nozzles). The printing settings were optimized with the resolution of 360 × 360 dpi.

Theoretical Methods: The DFT was employed for all the simulations reported in this paper. To assess the influence of the chemical variations on the energetic levels of PCBM and PCBC6, HOMO and LUMO energy levels of these molecules were calculated in toluene with the Gaussian 09 software, employing B3LYP/6-311++G** level of theory and polarizable conductor solvent model (C-PCM) implicit solvation model.[49,50] Aggregation energies of fullerene-based systems have already been theoretically studied by several research groups adopting different computational approaches.[51,52] In the case, estimation of this energy for solid state PCBM and PCBC6 were carried out with the CP2K software version 6.1, employing a Generalised Gradient Approximation (GGA)-Perdew-Burke-Ernzerhof (PBE) functional, double-zeta valence polarized (DZVP) basis sets, and Goedecker-Teter-Hutter (GTH) Pseudo Potentials, with a cutoff on the grid of 600 Ry and Grimme VdW correction (DFT-D3) to take into account dispersion interactions.[53–57]

Current–Voltage Characterization: Current density–voltage characterization and stabilized power output measurements were performed using a Keithley 2461 source measure unit under simulated Air Mass (AM) 1.5G irradiation (100 mA cm⁻²) using an AAA-rated solar simulator (Abet Technologies, sun 2000) calibrated against an RR-208-KG5 silicon reference cell (Abet Technologies). The mismatch factor for the studied perovskite solar cells was 0.94 and this value was used correct the intensity of the solar simulator lamp to provide 1 sun (for discussion see Section S1.6 and Table S4, Supporting Information). Solar cells were masked to 1 cm². *J–V* measurements were performed in two scan directions, from forward bias to short-circuit and from short-circuit to forward bias. The scanning rate was set to 500 mV s⁻¹. The stabilized power conversion efficiency (SPO) was measured at the maximum power point voltage for a duration of 30 s.

External Quantum Efficiency: The EQE was measured using Bentham PVE300 photovoltaic characterization system and the control software BenWin+.

Scanning Electron Microscopy: Cross-section images were obtained by employing focus ion beam scanning electron microscope (FEI Helios 600), with an accelerating voltage of 2 kV. The samples were prepared by depositing carbon and platinum films on top of a sample.

Atomic Force Microscopy: The AFM images were obtained using a Park Systems, Model XE7 in noncontact mode, and scanning over a range of 25 μm by 25 μm at a resolution of 128 × 128 data points. The surface roughness was measured as the root mean-squared roughness over the scanning area.

PLQY: Perovskite films were processed directly on pre-cleaned plain glass substrates. Subsequently, different electron transporting materials were deposited on top of perovskite layer (following the procedures described in the Device Fabrication section). The measuring setup was

based on FS5 Spectrofluorometer (Edinburgh Instruments), equipped with an integrating sphere. An excitation wavelength of 405 nm was used with the intensity of the order of 0.05 sun (5 mW cm^{-2}). This means that the PLQY and QFLS values are lower than those expected at 1 sun.[58] The PL signal is collected in the spectral range of 720–820 nm. A glass substrate was used as a reference for the glass/perovskite/electron transport layer (ETL) samples.

Photoluminescence of Solar Cells at Open-Circuit and Short-Circuit: Complete flexible perovskite solar cells were used for this experiment. The measurement setup was based on Andor Shamrock 193i Czerny-Turner type spectrometer. The illumination source for PL measurements was a frequency doubled continuous wave neodymium-doped yttrium aluminum garnet (Nd-YAG) laser from Pegasus laser systems (Pluto, P532.400, $\lambda = 532$ nm). The working point of the measured solar cell was set by a LabVIEW controlled Keithley 2400 source meter. To calibrate the excitation intensity, short circuit current of one cell was measured. The laser intensity was adjusted that the cells J_{SC} on the PL setup matched the J_{SC} previously measured on a mismatch corrected solar simulator (AM 1.5G equivalent). For samples having the same architecture and differing only in a transport layer material, the laser power was kept constant, so the measured PL intensities could be compared directly.

TPV and TPC Measurements: The TPV and TPC were measured with a commercial apparatus (Arkeo, Cicci Research s.r.l.) based on a high-speed Waveform Generator that drives a high-speed LED (5000 Kelvin). The device was connected to a transimpedance amplifier and a differential voltage amplifier to monitor short circuit current or open circuit voltage. The measurements were executed with varied light intensities throughout the measurement, using the white LED. The intensities ranged between 30 and 160 mW cm^{-2}. For each illumination level 200 traces were recorded, both in TPC and TPV experiment.

Supporting Information

Supporting Information is available from the Wiley Online Library or from the author.

Acknowledgements

Conflict of Interest

The authors declare no conflict of interest.

Keywords

[1] M. A. Green, A. Ho-Baillie, H. J. Snaith, *Nat. Photonics* **2014**, *8*, 506.

[2] T. Miyasaka, A. Kojima, K. Teshima, Y. Shirai, *J. Am. Chem. Soc.* **2009**, *131*, 7256.

[3] Best Research-Cell Efficiencies, https://www.nrel.gov/pv/assets/pdfs/best-research-cell-efficiencies.20200406.pdf (accessed: April 2020).

[4] H. Xie, X. Yin, Y. Guo, J. Liu, W. Que, G. Wang, *Phys. Status Solidi RRL* **2019**, *13*, 1800566.

[5] L. Qiu, S. He, L. K. Ono, S. Liu, Y. Qi, *ACS Energy Lett.* **2019**, *4*, 2147.

[6] K. Wojciechowski, D. Forgács, T. Rivera, *Sol. RRL* **2019**, *3*, 1900144.

[7] M. O. Reese, S. Glynn, M. D. Kempe, D. L. McGott, M. S. Dabney, T. M. Barnes, S. Booth, D. Feldman, N. M. Haegel, *Nat. Energy* **2018**, *3*, 1002.

[8] B. Chen, P. N. Rudd, S. Yang, Y. Yuan, J. Huang, *Chem. Soc. Rev.* **2019**, *48*, 3842.

[9] E. Aydin, M. de Bastiani, S. de Wolf, *Adv. Mater.* **2019**, *31*, 1900428.

[10] B. Roose, Q. Wang, A. Abate, *Adv. Energy Mater.* **2019**, *9*, 1803140.

[11] T. Liu, K. Chen, Q. Hu, R. Zhu, Q. Gong, *Adv. Energy Mater.* **2016**, *6*, 1600457.

[12] Q. Wali, F. J. Iftikhar, N. K. Elumalai, Y. Iqbal, S. Yousaf, S. Iqbal, R. Jose, *Curr. Appl. Phys.* **2020**, *20*, 720.

[13] Y. Bai, X. Meng, S. Yang, *Adv. Energy Mater.* **2018**, *8*, 1701883.

[14] M. Zhang, X. Zhan, *Adv. Energy Mater.* **2019**, *9*, 1900860.

[15] S. K. Jung, J. H. Heo, D. W. Lee, S. C. Lee, S. H. Lee, W. Yoon, H. Yun, S. H. Im, J. H. Kim, O. P. Kwon, *Adv. Funct. Mater.* **2018**, *28*, 1800346.

[16] Y. Shao, Z. Xiao, C. Bi, Y. Yuan, J. Huang, *Nat. Commun.* **2014**, *5*, 5784.

[17] J. Xu, A. Buin, A. H. Ip, W. Li, O. Voznyy, R. Comin, M. Yuan, S. Jeon, Z. Ning, J. J. McDowell, P. Kanjanaboos, J. P. Sun, X. Lan, L. N. Quan, D. H. Kim, I. G. Hill, P. Maksymovych, E. H. Sargent, *Nat. Commun.* **2015**, *6*, 7081.

[18] A. B. Djurišić, F. Z. Liu, H. W. Tam, M. K. Wong, A. Ng, C. Surya, W. Chen, Z. B. He, *Prog. Quantum Electron.* **2017**, *53*, 1.

[19] Y. Zheng, J. Kong, D. Huang, W. Shi, L. Mcmillon-Brown, H. E. Katz, J. Yu, A. D. Taylor, *Nanoscale* **2018**, *10*, 11342.

[20] C. S. Ponseca, E. M. Hutter, P. Piatkowski, B. Cohen, T. Pascher, A. Douhal, A. Yartsev, V. Sundström, T. J. Savenije, *J. Am. Chem. Soc.* **2015**, *137*, 16043.

[21] Y. Shao, Y. Yuan, J. Huang, *Nat. Energy* **2016**, *1*, 15001.

[22] L. L. Deng, S. Y. Xie, F. Gao, *Adv. Electron. Mater.* **2018**, *4*, 1700435.

[23] T. Gatti, E. Menna, M. Meneghetti, M. Maggini, A. Petrozza, F. Lamberti, *Nano Energy* **2017**, *41*, 84.

[24] Y. Bai, H. Yu, Z. Zhu, K. Jiang, T. Zhang, N. Zhao, S. Yang, H. Yan, *J. Mater. Chem. A* **2015**, *3*, 9098.

[25] H. K. Lin, Y. W. Su, H. C. Chen, Y. J. Huang, K. H. Wei, *ACS Appl. Mater. Interfaces* **2016**, *8*, 24603.

[26] K. Chen, Q. Hu, T. Liu, L. Zhao, D. Luo, J. Wu, Y. Zhang, W. Zhang, F. Liu, T. P. Russell, R. Zhu, Q. Gong, *Adv. Mater.* **2016**, *28*, 10718.

[27] Z. Liu, P. Liu, T. He, L. Zhao, X. Zhang, J. Yang, H. Yang, H. Liu, R. Qin, M. Yuan, *ACS Appl. Mater. Interfaces* **2020**, *12*, 26670.

[28] P. Ru, E. Bi, Y. Zhang, Y. Wang, W. Kong, Y. Sha, W. Tang, P. Zhang, Y. Wu, W. Chen, X. Yang, H. Chen, L. Han, *Adv. Energy Mater.* **2020**, *10*, 1903487.

[29] Z. Liu, S. Li, X. Wang, Y. Cui, Y. Qin, S. Leng, Y.-x. Xu, K. Yao, H. Huang, *Nano Energy* **2019**, *62*, 734.

[30] S. Hu, *Masters Thesis*, University of Tennessee, Knoxville **2013**.

[31] R. P. J. Bronger, J. P. Bermon, J. Herwig, P. C. J. Kamer, P. W. N. M. van Leeuwen, *Adv. Synth. Catal.* **2004**, *346*, 789.

[32] G. Paternò, A. J. Warren, J. Spencer, G. Evans, V. G. Sakai, J. Blumberger, F. Cacialli, *J. Mater. Chem. C* **2013**, *1*, 5619.

[33] L. Benatto, C. F. N. Marchiori, T. Talka, M. Aramini, N. A. D. Yamamoto, S. Huotari, L. S. Roman, M. Koehle, *Thin Solid Films* **2020**, *697*, 137827.

[34] Z. Yang, J. Xie, V. Arivazhagan, K. Xiao, Y. Qiang, K. Huang, M. Hu, C. Cui, X. Yu, D. Yang, *Nano Energy* **2017**, *40*, 345.

[35] M. Saliba, T. Matsui, J. Y. Seo, K. Domanski, J. P. Correa-Baena, M. K. Nazeeruddin, S. M. Zakeeruddin, W. Tress, A. Abate, A. Hagfeldt, M. Grätzel, *Energy Environ. Sci.* **2016**, *9*, 1989.

[36] B. Chen, M. Yang, S. Priya, K. Zhu, *J. Phys. Chem. Lett.* **2016**, *7*, 905.

[37] S. Ravishankar, S. Gharibzadeh, C. Roldán-Carmona, G. Grancini, Y. Lee, M. Ralaiarisoa, A. M. Asiri, N. Koch, J. Bisquert, M. K. Nazeeruddin, *Joule* **2018**, *2*, 788.

[38] M. Stolterfoht, C. M. Wolff, J. A. Márquez, S. Zhang, C. J. Hages, D. Rothhardt, S. Albrecht, P. L. Burn, P. Meredith, T. Unold, D. Neher, *Nat. Energy* **2018**, *3*, 847.

[39] E. A. Duijnstee, J. M. Ball, V. M. le Corre, L. J. A. Koster, H. J. Snaith, J. Lim, *ACS Energy Lett.* **2020**, *5*, 376.

[40] C. Bi, Q. Wang, Y. Shao, Y. Yuan, Z. Xiao, J. Huang, *Nat. Commun.* **2015**, *6*, 7747.

[41] D. Luo, W. Yang, Z. Wang, A. Sadhanala, Q. Hu, R. Su, R. Shivanna, G. F. Trindade, J. F. Watts, Z. Xu, T. Liu, K. Chen, F. Ye, P. Wu, L. Zhao, J. Wu, Y. Tu, Y. Zhang, X. Yang, W. Zhang, R. H. Friend, Q. Gong, H. J. Snaith, R. Zhu, *Science* **2018**, *360*, 1442.

[42] C. M. Wolff, P. Caprioglio, M. Stolterfoht, D. Neher, *Adv. Mater.* **2019**, *31*, 1902762.

[43] K. Wojciechowski, S. D. Stranks, A. Abate, G. Sadoughi, A. Sadhanala, N. Kopidakis, G. Rumbles, C. Z. Li, R. H. Friend, A. K. Y. Jen, H. J. Snaith, *ACS Nano* **2014**, *8*, 12701.

[44] P. Caprioglio, M. Stolterfoht, C. M. Wolff, T. Unold, B. Rech, S. Albrecht, D. Neher, *Adv. Energy Mater.* **2019**, *9*, 1901631.

[45] H. Wang, Y. He, Y. Li, H. Su, *J. Phys. Chem. A* **2012**, *116*, 255.

[46] O. J. Sandberg, J. Kurpiers, M. Stolterfoht, D. Neher, P. Meredith, S. Shoaee, A. Armin, *Adv. Mater. Interfaces* **2020**, *7*, 2000041.

[47] R. K. Singh, R. Kumar, A. Kumar, N. Jain, R. K. Singh, J. Singh, *J. Alloys Compd.* **2018**, *743*, 728.

[48] M. Saliba, J. P. Correa-Baena, C. M. Wolff, M. Stolterfoht, N. Phung, S. Albrecht, D. Neher, A. Abate, *Chem. Mater.* **2018**, *30*, 4193.

[49] M. J. Frisch, G. W. Trucks, H. B. Schlegel, G. E. Scuseria, M. A. Robb, J. R. Cheeseman, G. Scalmani, V. Barone, G. A. Petersson, H. Nakatsuji, X. Li, M. Caricato, A. V. Marenich, J. Bloino, B. G. Janesko, R. Gomperts, B. Mennucci, H. P. Hratchian, J. V. Ortiz, A. F. Izmaylov, J. L. Sonnenberg, D. Williams-Young, F. Ding, F. Lipparini, F. Egidi, J. Goings, B. Peng, A. Petrone, T. Henderson, D. Ranasinghe, et al., Gaussian 16, Revision C.01, Gaussian, Inc., Wallingford CT **2016**.

[50] M. Cossi, N. Rega, G. Scalmani, V. Barone, *J. Comput. Chem.* **2003**, *24*, 669.

[51] M. F. N. Taufique, S. Choudhury, S. Banerjee, *J. Phys. Chem. C* **2019**, *123*, 22368.

[52] N. R. Tummala, C. Sutton, S. G. Aziz, M. F. Toney, C. Risko, J. L. Bredas, *Chem. Mater.* **2015**, *27*, 8261.

[53] J. Hutter, M. Iannuzzi, F. Schiffmann, J. Vandevondele, *Wiley Interdiscip. Rev.: Comput. Mol. Sci.* **2014**, *4*, 15.

[54] J. P. Perdew, K. Burke, M. Ernzerhof, *Phys. Rev. Lett.* **1996**, *77*, 3865.

[55] S. Grimme, J. Antony, S. Ehrlich, H. Krieg, *J. Chem. Phys.* **2010**, *132*, 154104.

[56] S. Goedecker, M. Teter, *Phys. Rev. B* **1996**, *54*, 1703.

[57] J. VandeVondele, J. Hutter, *J. Chem. Phys.* **2007**, *127*, 114105.

[58] C. H. Chiang, C. G. Wu, *Nat. Photonics* **2016**, *10*, 196.

7.Patent description

Title of application: A PEROVSKITE STRUCTURE, A PHOTOVOLTAIC CELL AND A METHOD FOR PREPARATION THEREOF

Application number: EP22461539.3, 25/04/2022

Authors: WILK Barbara; IVANOVSKA Tanja; WOJCIECHOWSKI Konrad

Barbara Wilk contribution:

- Invention;
- Providing the proofs of invention (deposition and characterization of the layers);
- Testing new materials for extending the scope of patent;
- Support in defining the claims and application writing.

Due to the current status of the patent application, sensitive data are kept confidential.

7.1.Background of the invention

The international certification tests for solar cells require operation for a long time at elevated temperature, and to pass this the organic component of the hybrid perovskites may need to be replaced. The inorganic perovskite solar cells represent a group of perovskite solar cells with an inorganic perovskite absorber layer which have significantly higher thermal stability than the organic-inorganic perovskite counterparts. Thus, inorganic perovskites may be the future of perovskite technology. $CsPbI_3$ can crystallize in four different crystallographic phases such as perovskite cubic phase (α), tetragonal phase (β), orthorhombic phase (γ) and non-perovskite orthorhombic phase (δ). The specific n-i-p device architecture requires a layered structure consisting of the substrate with electrode, electron transport layer (ETL), perovskite absorber, hole transport layer (HTL), and counter electrode. One of the limitations of this architecture and concept of preparation is the high annealing temperature for the inorganic perovskite. Obtaining photoactive perovskite phases (α, β or γ) requires post-processing above 200°C which limits the choice of substrates, as well as requires higher consumption of energy for device preparation.

7.2.Description of the invention

By incorporation of a seeding layer (meaning a thin 1-20 nm layer of a specific material) on top of the ETL or modifying the ETL itself, one can obtain perovskite crystallization at low temperatures. Essentially, the seeding layer or ETL modification facilitates the nucleation

of the perovskite $CsPbI_3$ phase at low temperature and provides improved thermodynamic stability (formed black $CsPbI_3$ is more stable at room temperature).

The difference in crystallinity between inorganic perovskite prepared in the standard way and using described seeding layer approach was evaluated by X-ray diffraction measurement. Figure 7.1 shows the change in the crystallographic structure of perovskite absorber grown on ETL layer -Tin Oxide (SnO_2), SnO_2 coated by seeding layers made of S1, S2, S3, and on SnO_2 modified by S1 addition.
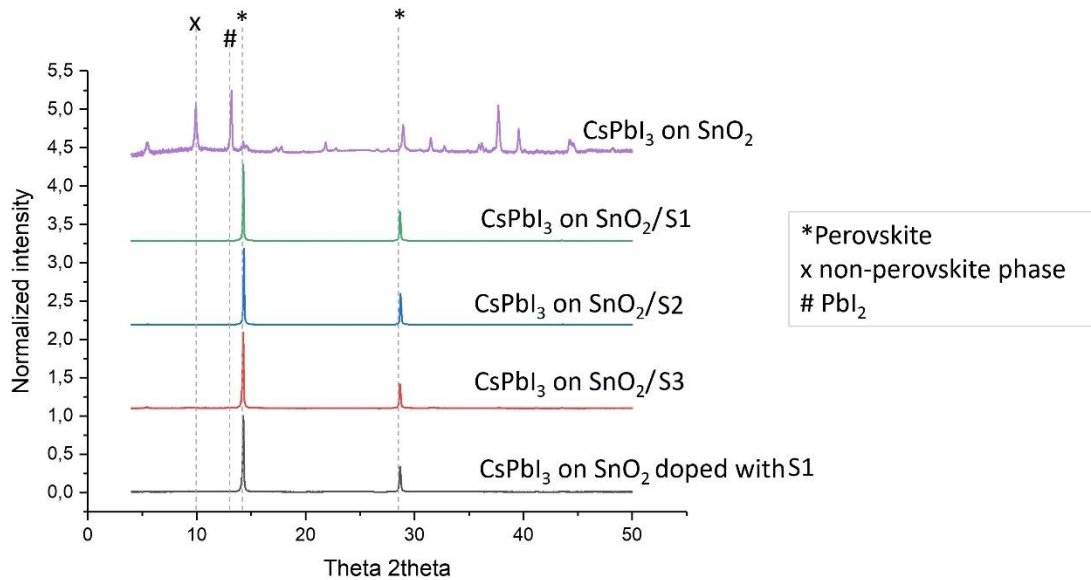

Figure 7.1 X-ray diffractogram patterns of the perovskite crystalized on SnO₂, SnO₂ covered by different seeding layers and on modified SnO₂

Perovskite films deposited on the seeding layer or modified ETL crystallized in the desired phase at 100 °C. The perovskite phase is present on several different seeding layers or modified SnO_2, while only the non-perovskite phase (δ) is present when the perovskite is deposited directly on top of unmodified ETL (SnO_2). Different ETLs can be used, such as TiO_2, ZnO, fullerenes, etc. Figure 7.2 shows that once the perovskite phase is formed with the presence of the seeding layer, it does not undergo a phase transition to the non-perovskite phase upon prolonged storage. Thus, not only quality but also thermodynamic stability at room temperature of the film is enhanced.
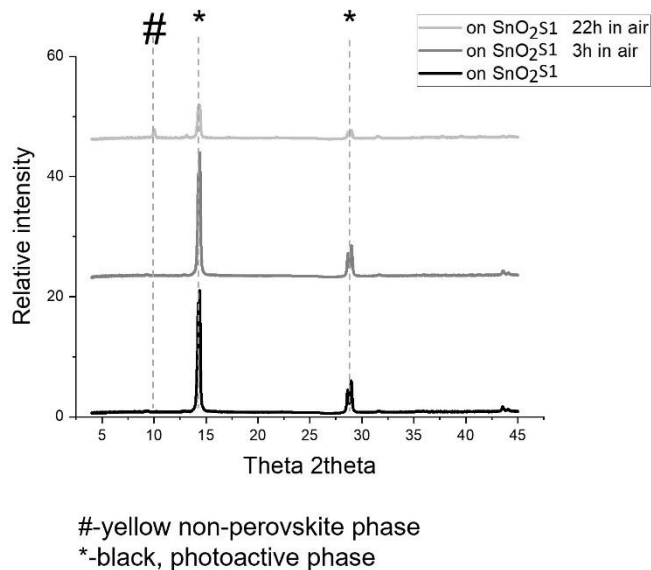
#-yellow non-perovskite phase
*-black, photoactive phase

Figure 7.2 X-ray diffractograms of inorganic perovskite crystallized on SnO2 covered by S1 seeding layer

7.3.Industrial application of the invention

Described invention allows to fabricate inorganic perovskite layer at low temperature (below 120°C) in ambient conditions. The invention can be applied in the production of optoelectronic devices based on $CsPbI_3$ inorganic perovskite, allowing the usage of flexible substrates and temperature-sensitive materials. Invented procedure allowed to print inorganic perovskite in industrial conditions, but its applicability is not limited to inkjet printing. Proposed architecture with additional seeding layer can be also obtained by other solution-based coating methods extending the application of the invention.

8. CONCLUSIONS

The work presented in this thesis has been concerned with the development of the inkjet printing process for perovskite solar cells fabrication. It was focused on optimizing the ink compositions and processing conditions for different perovskite materials and functional layers.

Inkjet printing was found to be a very useful tool for the deposition of functional inks including perovskite precursor solutions. The specific features of inkjet like high precision of drop placement, small ink consumption and ability to customize the shape of the printout are attractive for large area deposition of thin layers of perovskite solar cell. However, the development of the inkjet printing process is very challenging. It was shown in this thesis, that the design of the ink, especially for perovskite printing, requires complex research including a detailed study of ink rheology as well as ink stability, drying profile, and toxicity. The hypothesis concerning the application of the inkjet technique for perovskite solar cells production has been proved. Inkjet printing has been implemented to print three different perovskite formulations and one functional transport layer (ETL) proving its usability for PSCs production.

Choosing inkjet printing for perovskite deposition forced to analyse the solutions from a different perspective, uncommon for standard perovskite deposition techniques (like spin-coating). It was shown in the publication about mixed cation perovskite printing that the observation of jetting behaviour can lead to an understanding of the coordination mechanism occurring in the solution. Thus, it can be concluded that inkjet printing is very useful, especially at the research and development stage, where observations of rheological parameters of precursor solutions may bring additional insights into the chemical interactions happening in the ink.

Additionally, using inkjet printing enforces the open-air conditions as the machines are usually big and not glove-box compatible, which brings another challenge on the way to successful perovskite deposition in the industrial environment. In this thesis, the importance of ink toxicity and air compatible crystallization was addressed.

Work published in this thesis has demonstrated that the inkjet printing technique is capable of large-area fabrication of perovskite solar cells. The research presented in this thesis delivered several observations and conclusions which can serve as a guideline for further optimization of perovskite solar cells processing critical to advancing the future development of this technology.

Optimized strategies are ready-made, industrially viable procedures for inkjet printing of mixed cation perovskite, quasi-2D perovskite and $PCBC_6$ based ETL layer. The invention described in the patent application can be applied in a wide range of solution-based techniques for inorganic perovskite coating. Thus, obtained results have a high implementation potential in the perovskite industry.

References

[1]   M. Gordon, M. Weber, and P. Raj, "Global energy demand to grow 47% by 2050, with oil still top source: US EIA," pp. 1–6, 2021, [Online]. Available: https://www.spglobal.com/platts/en/market-insights/latest-news/oil/100621-global-energy-demand-to-grow-47-by-2050-with-oil-still-top-source-us-eia.

[2]   N. K. M. A. Alrikabi, "Renewable Energy Types," *J. Clean Energy Technol.*, vol. 2, no. 1, pp. 61–64, 2014, doi: 10.7763/jocet.2014.v2.92.

[3]   Paul Breeze, *Power Generation Technologies*, Third Edit. 2019.

[4]   M. A. Green, "Forty years of photovoltaic research at UNSW," *J. Proc. R. Soc. New South Wales*, vol. 148, no. 455–456, pp. 2–14, 2015.

[5]   National Renewable Energy Laboratory, "Best Research- Cell Efficiencies." http://www.nrel.gov/ncpv/images/efficiency_chart.jpg. Accessed 7.07.2022

[6]   S. De Wolf *et al.*, "Organometallic halide perovskites: Sharp optical absorption edge and its relation to photovoltaic performance," *J. Phys. Chem. Lett.*, vol. 5, no. 6, pp. 1035–1039, 2014, doi: 10.1021/jz500279b.

[7]   J. H. Noh, S. H. Im, J. H. Heo, T. N. Mandal, and S. Il Seok, "Chemical Management for Colorful, E ffi cient, and Stable Inorganic – Organic Hybrid Nanostructured Solar Cells," 2013.

[8]   W. J. Yin, T. Shi, and Y. Yan, "Unusual defect physics in CH3NH3PbI3 perovskite solar cell absorber," *Appl. Phys. Lett.*, vol. 104, no. 6, 2014, doi: 10.1063/1.4864778.

[9]   X. He *et al.*, "40.1% Record Low-Light Solar-Cell Efficiency by Holistic Trap-Passivation using Micrometer-Thick Perovskite Film," *Adv. Mater.*, vol. 33, no. 27, pp. 1–10, 2021, doi: 10.1002/adma.202100770.

[10]   K. Wojciechowski, D. Forgács, and T. Rivera, "Industrial Opportunities and Challenges for Perovskite Photovoltaic Technology," *Sol. RRL*, vol. 3, no. 9, pp. 1–9, 2019, doi: 10.1002/solr.201900144.

[11]   J. Nelson, *The Physics of Solar Cells*. Imperial College Press, 2003.

[12]   NREL, "Reference Air Mass 1.5 Spectra." https://www.nrel.gov/grid/solar-resource/spectra-am1.5.html.

[13]   A. S. Bhalla, R. Guo, and R. Roy, "The perovskite structure – a review of its role in ceramic science and technology," *Mater. Res. Innov.*, vol. 4, no. 1, pp. 3–26, 2000, [Online]. Available: http://link.springer.com/article/10.1007/s100190000062.

[14]   Z. Bojarski, M. Giła, K. Stróż, and M. Surowiec, *Krystalografia*, 3rd ed. Warszawa: PWN, 2014.

[15]   Anon, "Chapter 3 Perovskite Perfect Lattice 3.1," in *Certificated engineer*, vol. 61, no. 6, 1988, pp. 22–23.

[16]   A. Kojima, K. Teshima, Y. Shirai, and T. Miyasaka, "Organometal halide perovskites as visible-light sensitizers for photovoltaic cells," *J. Am. Chem. Soc.*, vol. 131, no. 17, pp. 6050–6051, 2009, doi: 10.1021/ja809598r.

[17]   P. S. Whitfield *et al.*, "Structures, Phase Transitions and Tricritical Behavior of the Hybrid Perovskite Methyl Ammonium Lead Iodide," *Sci. Rep.*, vol. 6, no. June, pp. 1–16, 2016, doi: 10.1038/srep35685.

[18]   M. M. Lee, J. Teuscher, T. Miyasaka, T. N. Murakami, and H. J. Snaith, "Efficient hybrid solar cells based on meso-superstructured organometal halide perovskites," *Science (80-.).*, vol. 338, no. 6107, pp. 643–647, 2012, doi: 10.1126/science.1228604.

[19]   H. S. Kim *et al.*, "Lead iodide perovskite sensitized all-solid-state submicron thin film mesoscopic solar cell with efficiency exceeding 9%," *Sci. Rep.*, vol. 2, pp. 1–7, 2012, doi: 10.1038/srep00591.

[20]   A. S. Shikoh and A. Polyakov, "A Quantitative Analysis of the Research Trends in Perovskite Solar Cells in 2009–2019," *Phys. Status Solidi Appl. Mater. Sci.*, vol. 217, no. 23, 2020, doi: 10.1002/pssa.202000441.

[21]   T. C. J. Yang, P. Fiala, Q. Jeangros, and C. Ballif, "High-Bandgap Perovskite Materials for Multijunction Solar Cells," *Joule*, vol. 2, no. 8, pp. 1421–1436, 2018, doi: 10.1016/j.joule.2018.05.008.

[22]   L. Schmidt-mende *et al.*, "Roadmap on organic – inorganic hybrid perovskite semiconductors and devices Roadmap on organic – inorganic hybrid perovskite semiconductors and devices," vol. 109202, no. October, 2021, doi: 10.1063/5.0047616.

[23]   R. Prasanna *et al.*, "Band Gap Tuning via Lattice Contraction and Octahedral Tilting in Perovskite Materials for Photovoltaics," *J. Am. Chem. Soc.*, vol. 139, no. 32, pp. 11117–11124, 2017, doi: 10.1021/jacs.7b04981.

[24]   G. Tang, P. Ghosez, and J. Hong, "Band-edge orbital engineering of perovskite semiconductors for optoelectronic applications," *J. Phys. Chem. Lett.*, vol. 12, no. 17, pp. 4227–4239, 2021, doi: 10.1021/acs.jpclett.0c03816.

[25]   F. Ünlü *et al.*, "Understanding the interplay of stability and efficiency in A-site engineered lead halide perovskites," *APL Mater.*, vol. 8, no. 7, 2020, doi: 10.1063/5.0011851.

[26]   J.-H. Lee *et al.*, "Resolving the Physical Origin of Octahedral Tilting in Halide Perovskites," 2016, doi: 10.1021/acs.chemmater.6b00968.

[27]   T. S. Sherkar *et al.*, "Recombination in Perovskite Solar Cells: Significance of Grain Boundaries, Interface Traps, and Defect Ions," *ACS Energy Letters*, vol. 2, no. 5. pp. 1214–1222, 2017, doi: 10.1021/acsenergylett.7b00236.

[28]   L. M. Herz, "Charge-Carrier Mobilities in Metal Halide Perovskites: Fundamental Mechanisms and Limits," *ACS Energy Lett.*, vol. 2, no. 7, pp. 1539–1548, 2017, doi: 10.1021/acsenergylett.7b00276.

[29]   F. Zhang, B. Yang, Y. Li, W. Deng, and R. He, "Extra long electron-hole diffusion lengths in CH3NH3PbI3-: XClx perovskite single crystals," *J. Mater. Chem. C*, vol. 5, no. 33, pp. 8431–8435, 2017, doi: 10.1039/c7tc02802d.

[30]   S. D. Stranks *et al.*, "Electron-hole diffusion lengths exceeding 1 micrometer in an organometal trihalide perovskite absorber," *Science (80-.).*, vol. 342, no. 6156, pp. 341–344, 2013, doi: 10.1126/science.1243982.

[31]   G. Xing, N. Mathews, S. S. Lim, Y. M. Lam, S. Mhaisalkar, and T. C. Sum, "Long-Range Balanced Electron- and Hole-Transport Lengths in Organic-Inorganic CH 3 NH 3 PbI 3," vol. 6960, no. October, pp. 498–500, 2013.

[32]   V. M. Le Corre *et al.*, "Charge Transport Layers Limiting the Efficiency of Perovskite Solar Cells: How to Optimize Conductivity, Doping, and Thickness," *ACS Appl. Energy Mater.*, vol. 2, no. 9, pp. 6280–6287, 2019, doi: 10.1021/acsaem.9b00856.

[33]   H. Wang *et al.*, "Progress in perovskite solar cells towards commercialization—a review," *Materials (Basel).*, vol. 14, no. 21, pp. 1–41, 2021, doi: 10.3390/ma14216569.

[34]   S. Zhang and G. Han, "Intrinsic and environmental stability issues of perovskite photovoltaics," *Prog. Energy*, vol. 2, no. 2, p. 022002, 2020, doi: 10.1088/2516-1083/ab70d9.

[35]   G. E. Eperon, S. D. Stranks, C. Menelaou, M. B. Johnston, L. M. Herz, and H. J. Snaith, "Formamidinium lead trihalide : a broadly tunable perovskite for e ffi cient planar heterojunction solar," *Energy Environ. Sci.*, vol. 7, pp. 982–988, 2014, doi: 10.1039/c3ee43822h.

[36]   Z. Li, M. Yang, J. S. Park, S. H. Wei, J. J. Berry, and K. Zhu, "Stabilizing Perovskite Structures by Tuning Tolerance Factor: Formation of Formamidinium and Cesium Lead Iodide Solid-State Alloys," *Chem. Mater.*, vol. 2, no. 1, pp. 284–292, 2015, doi: 10.1021/acs.chemmater.5b04107.

[37]   S. Mazumdar, Y. Zhao, and X. Zhang, "Stability of Perovskite Solar Cells: Degradation Mechanisms and Remedies," *Front. Electron.*, vol. 2, no. August, pp. 1–34, 2021, doi: 10.3389/felec.2021.712785.

[38]   B. Conings *et al.*, "Intrinsic Thermal Instability of Methylammonium Lead Trihalide Perovskite," *Adv. Energy Mater.*, vol. 5, no. 15, 2015, doi: 10.1002/aenm.201500477.

[39]   D. W. DeQuilettes *et al.*, "Photo-induced halide redistribution in organic-inorganic perovskite films," *Nat. Commun.*, vol. 7, no. May, 2016, doi: 10.1038/ncomms11683.

[40]   E. T. Hoke, D. J. Slotcavage, E. R. Dohner, A. R. Bowring, H. I. Karunadasa, and M. D. McGehee, "Reversible photo-induced trap formation in mixed-halide hybrid perovskites for photovoltaics," *Chem. Sci.*, vol. 6, no. 1, pp. 613–617, 2015, doi: 10.1039/c4sc03141e.

[41]   D. Di Girolamo *et al.*, "Ion Migration-Induced Amorphization and Phase Segregation as a Degradation Mechanism in Planar Perovskite Solar Cells," *Adv. Energy Mater.*,

vol. 10, no. 25, 2020, doi: 10.1002/aenm.202000310.

[42] G. Richardson *et al.*, "Can slow-moving ions explain hysteresis in the current-voltage curves of perovskite solar cells?," *Energy Environ. Sci.*, vol. 9, no. 4, pp. 1476–1485, 2016, doi: 10.1039/c5ee02740c.

[43] Y. Kato, L. K. Ono, M. V. Lee, S. Wang, S. R. Raga, and Y. Qi, "Silver Iodide Formation in Methyl Ammonium Lead Iodide Perovskite Solar Cells with Silver Top Electrodes," *Adv. Mater. Interfaces*, vol. 2, no. 13, pp. 2–7, 2015, doi: 10.1002/admi.201500195.

[44] M. Saliba, K. Nazeeruddin, S. M. Zakeeruddin, T. Matsui, J. Seo, and K. Domanski, "Cesium-containing triple cation perovskite solar cells : improved stability , reproducibility and high efficiency," *Energy Environ. Sci.*, 2016, doi: 10.1039/C5EE03874J.

[45] G. Grancini *et al.*, "One-Year stable perovskite solar cells by 2D/3D interface engineering," *Nat. Commun.*, vol. 8, pp. 1–8, 2017, doi: 10.1038/ncomms15684.

[46] K. M. Lee *et al.*, "Enhanced efficiency and stability of quasi-2D/3D perovskite solar cells by thermal assisted blade coating method," *Chem. Eng. J.*, vol. 405, no. June 2020, p. 126992, 2021, doi: 10.1016/j.cej.2020.126992.

[47] C. Pereyra, H. Xie, and M. Lira-Cantu, "Additive engineering for stable halide perovskite solar cells," *J. Energy Chem.*, vol. 60, pp. 599–634, 2021, doi: 10.1016/j.jechem.2021.01.037.

[48] C. Manspeaker, S. Venkatesan, A. Zakhidov, and K. S. Martirosyan, "Role of interface in stability of perovskite solar cells," *Current Opinion in Chemical Engineering*, vol. 15. Elsevier Ltd, pp. 1–7, Feb. 01, 2017, doi: 10.1016/j.coche.2016.08.013.

[49] S. Zhang *et al.*, "Improved performance and stability of perovskite solar modules by interface modulating with graphene oxide crosslinked CsPbBr 3 quantum dots," *Energy Environ. Sci.*, vol. 15, no. 1, pp. 244–253, 2022, doi: 10.1039/D1EE01778K.

[50] V. Babu *et al.*, "Improved Stability of Inverted and Flexible Perovskite Solar Cells with Carbon Electrode," *ACS Appl. Energy Mater.*, vol. 3, no. 6, pp. 5126–5134, Jun. 2020, doi: 10.1021/ACSAEM.0C00702/SUPPL_FILE/AE0C00702_SI_001.PDF.

[51] J.-M. Cha, J.-W. Lee, D.-Y. Son, H.-S. Kim, I.-H. Jang, and N.-G. Park, "Mesoscopic perovskite solar cells with an admixture of nanocrystalline TiO 2 and Al 2 O 3 : role of interconnectivity of TiO 2 in charge collection," *Nanoscale*, vol. 8, no. 12, pp. 6341–6351, 2016, doi: 10.1039/C5NR05974G.

[52] R. Ranjan *et al.*, "Enhanced efficiency and thermal stability of mesoscopic perovskite solar cells by adding PC70BM acceptor," *Sol. Energy Mater. Sol. Cells*, vol. 202, p. 110130, Nov. 2019, doi: 10.1016/j.solmat.2019.110130.

[53] M. Liu, M. B. Johnston, and H. J. Snaith, "Efficient planar heterojunction perovskite solar cells by vapour deposition.," *Nature*, vol. 501, no. 7467, pp. 395–8, Sep. 2013, doi: 10.1038/nature12509.

[54] Q. Jiang *et al.*, "Planar-Structure Perovskite Solar Cells with Efficiency beyond 21%," *Adv. Mater.*, vol. 29, no. 46, p. 1703852, Dec. 2017, doi: 10.1002/adma.201703852.

[55] D. Bi *et al.*, "Effect of Different Hole Transport Materials on Recombination in," *J. Phys. Chem. Lett.*, vol. 4, pp. 1532–1536, 2013, [Online]. Available: http://pubs.acs.org/doi/abs/10.1021/jz400638x.

[56] S. Li, Y. L. Cao, W. H. Li, and Z. S. Bo, "A brief review of hole transporting materials commonly used in perovskite solar cells," *Rare Met.*, vol. 40, no. 10, pp. 2712–2729, 2021, doi: 10.1007/s12598-020-01691-z.

[57] A. Magomedov *et al.*, "Self-Assembled Hole Transporting Monolayer for Highly Efficient Perovskite Solar Cells," *Adv. Energy Mater.*, vol. 8, no. 32, 2018, doi: 10.1002/aenm.201801892.

[58] N. Rai, S. Rai, P. K. Singh, P. Lohia, and D. K. Dwivedi, "Analysis of various ETL materials for an efficient perovskite solar cell by numerical simulation," *J. Mater. Sci. Mater. Electron.*, vol. 31, no. 19, pp. 16269–16280, 2020, doi: 10.1007/s10854-020-04175-z.

[59] P. Roy, N. Kumar Sinha, S. Tiwari, and A. Khare, "A review on perovskite solar cells: Evolution of architecture, fabrication techniques, commercialization issues and status," *Sol. Energy*, vol. 198, no. January, pp. 665–688, 2020, doi: 10.1016/j.solener.2020.01.080.

[60] Z. Zhou and S. Pang, "Highly efficient inverted hole-transport-layer-free perovskite solar cells," *J. Mater. Chem. A*, vol. 8, no. 2, pp. 503–512, 2020, doi: 10.1039/c9ta10694d.

[61] M. Abbas, L. Zeng, F. Guo, M. Rauf, X. C. Yuan, and B. Cai, "A critical review on crystal growth techniques for scalable deposition of photovoltaic perovskite thin films," *Materials (Basel).*, vol. 13, no. 21, pp. 1–42, 2020, doi: 10.3390/ma13214851.

[62] A. F. Akbulatov *et al.*, "Film Deposition Techniques Impact the Defect Density and Photostability of MAPbI3Perovskite Films," *J. Phys. Chem. C*, vol. 124, no. 39, pp. 21378–21385, 2020, doi: 10.1021/acs.jpcc.0c07673.

[63] Y. H. Chiang, M. Anaya, and S. D. Stranks, "Multisource Vacuum Deposition of Methylammonium-Free Perovskite Solar Cells," *ACS Energy Lett.*, vol. 5, no. 8, pp. 2498–2504, 2020, doi: 10.1021/acsenergylett.0c00839.

[64] S. Ngqoloda *et al.*, "Air-Stable Hybrid Perovskite Solar Cell by Sequential Vapor Deposition in a Single Reactor," *ACS Appl. Energy Mater.*, vol. 3, no. 3, pp. 2350–2359, 2020, doi: 10.1021/acsaem.9b01925.

[65] Q. Guesnay, F. Sahli, C. Ballif, and Q. Jeangros, "Vapor deposition of metal halide perovskite thin films: Process control strategies to shape layer properties," *APL Mater.*, vol. 9, no. 10, 2021, doi: 10.1063/5.0060642.

[66] T. Miyadera, T. Sugita, H. Tampo, K. Matsubara, and M. Chikamatsu, "Highly Controlled Codeposition Rate of Organolead Halide Perovskite by Laser Evaporation Method," *ACS Appl. Mater. Interfaces*, vol. 8, no. 39, pp. 26013–26018,

2016, doi: 10.1021/acsami.6b07837.

[67]   H. Wei *et al.*, "Flash-evaporation printing methodology for perovskite thin films," *NPG Asia Mater.*, vol. 9, no. 6, 2017, doi: 10.1038/am.2017.91.

[68]   G. Popov *et al.*, "Atomic Layer Deposition of PbI 2 Thin Films," *Chem. Mater.*, vol. 31, no. 3, pp. 1101–1109, 2019, doi: 10.1021/acs.chemmater.8b04969.

[69]   C. Borri *et al.*, "First proof-of-principle of inorganic lead halide perovskites deposition by magnetron-sputtering," *Nanomaterials*, vol. 10, no. 1, pp. 1–11, 2020, doi: 10.3390/nano10010060.

[70]   J. Li *et al.*, "Highly Efficient Thermally Co-evaporated Perovskite Solar Cells and Mini-modules," *Joule*, vol. 4, no. 5, pp. 1035–1053, 2020, doi: 10.1016/j.joule.2020.03.005.

[71]   K. Yan *et al.*, "Hybrid Halide Perovskite Solar Cell Precursors: Colloidal Chemistry and Coordination Engineering behind Device Processing for High Efficiency," *J. Am. Chem. Soc.*, vol. 137, no. 13, pp. 4460–4468, 2015, doi: 10.1021/jacs.5b00321.

[72]   D. P. McMeekin *et al.*, "Crystallization Kinetics and Morphology Control of Formamidinium–Cesium Mixed-Cation Lead Mixed-Halide Perovskite via Tunability of the Colloidal Precursor Solution," *Adv. Mater.*, vol. 29, no. 29, 2017, doi: 10.1002/adma.201607039.

[73]   Q. Wang *et al.*, "Scaling behavior of moisture-induced grain degradation in polycrystalline hybrid perovskite thin films," *Energy Environ. Sci.*, vol. 10, no. 2, pp. 516–522, 2017, doi: 10.1039/c6ee02941h.

[74]   S. Sánchez, L. Pfeifer, N. Vlachopoulos, and A. Hagfeldt, "Rapid hybrid perovskite film crystallization from solution," *Chem. Soc. Rev.*, vol. 50, no. 12, pp. 7108–7131, 2021, doi: 10.1039/d0cs01272f.

[75]   A. Khaleghi, S. M. Sadrameli, and M. Manteghian, "Thermodynamic and kinetics investigation of homogeneous and heterogeneous nucleation," *Rev. Inorg. Chem.*, vol. 40, no. 4, pp. 167–192, 2020, doi: 10.1515/revic-2020-0004.

[76]   Y. Zhao *et al.*, "Perovskite seeding growth of formamidinium-lead-iodide-based perovskites for efficient and stable solar cells," *Nat. Commun.*, vol. 9, no. 1, pp. 1–10, 2018, doi: 10.1038/s41467-018-04029-7.

[77]   M. K. Gangishetty, R. W. J. Scott, and T. L. Kelly, "Effect of relative humidity on crystal growth, device performance and hysteresis in planar heterojunction perovskite solar cells," *Nanoscale*, vol. 8, no. 12, pp. 6300–6307, 2016, doi: 10.1039/c5nr04179a.

[78]   S. D. Hoath, *Fundamentals of Inkjet Printing*. 2016.

[79]   R. D. Boehm, P. R. Miller, J. Daniels, S. Stafslien, and R. J. Narayan, "Inkjet printing for pharmaceutical applications," *Mater. Today*, vol. 17, no. 5, pp. 247–252, 2014, doi: 10.1016/j.mattod.2014.04.027.

[80]   "Inkjet." http://www.dp3project.org/technologies/digital-printing/inkjet.Accessed: 07.07.2022

[81] H. Wijshoff, "The dynamics of the piezo inkjet printhead operation," *Phys. Rep.*, vol. 491, no. 4–5, pp. 77–177, 2010, doi: 10.1016/j.physrep.2010.03.003.

[82] X. Li *et al.*, "A vacuum flash-assisted solution process for high-efficiency large-area perovskite solar cells," *Science (80-.).*, vol. 353, no. 6294, pp. 58–62, 2016, doi: 10.1126/science.aaf8060.

[83] A. Laaksonen and J. Malila, "Properties of water and ice," *Nucleation of Water*, pp. 31–44, 2022, doi: 10.1016/B978-0-12-814321-6.00011-7.

[84] M. V. Navarro, "Inkjet printing : a fl exible manufacturing of functional ceramic coatings by Chemical Solution Deposition," Universitat Autonoma de Barcelona, 2014.

[85] J. Fromm, "Numerical calculation of the fluid dynamics of drop-on-demand jets," *IBM J. Res. Dev.*, 1984, doi: 10.1147/RD.283.0322.

[86] B. D. N.Reis, "Ink Jet Deposition of Ceramic Suspensions: Modeling and Experiments of Droplet Formation," *MRS Symp. Proc.*, vol. 624, pp. 65–70, 2000.

[87] Z. Du, X. Yu, and Y. Han, "Inkjet printing of viscoelastic polymer inks," *Chinese Chem. Lett.*, vol. 29, no. 3, pp. 399–404, 2018, doi: 10.1016/j.cclet.2017.09.031.

[88] N. Gómez, E. Quintana, and J. C. Villar, "Effect of Paper Surface Properties on Coated Paper Wettability with Different Fountain Solutions," *BioResources*, vol. 9, no. 3, pp. 4226–4241, 2014, doi: 10.15376/biores.9.3.4226-4241.

[89] M. Pykönen *et al.*, "Effects of atmospheric pressure plasma activation on inkjet print quality," *Int. Conf. Digit. Print. Technol.*, no. January, pp. 404–409, 2007.

[90] P. Q. M. Nguyen, L. P. Yeo, B. K. Lok, and Y. C. Lam, "Patterned surface with controllable wettability for inkjet printing of flexible printed electronics," *ACS Appl. Mater. Interfaces*, vol. 6, no. 6, pp. 4011–4016, 2014, doi: 10.1021/am4054546.

[91] H. Y. Park, B. J. Kang, D. Lee, and J. H. Oh, "Control of surface wettability for inkjet printing by combining hydrophobic coating and plasma treatment," *Thin Solid Films*, vol. 546, pp. 162–166, 2013, doi: 10.1016/j.tsf.2013.03.067.

[92] J. M. Goddard and J. H. Hotchkiss, "Polymer surface modification for the attachment of bioactive compounds," *Prog. Polym. Sci.*, vol. 32, no. 7, pp. 698–725, 2007, doi: 10.1016/j.progpolymsci.2007.04.002.

[93] R. Morent, N. De Geyter, T. Desmet, P. Dubruel, and C. Leys, "Plasma surface modification of biodegradable polymers: A review," *Plasma Process. Polym.*, vol. 8, no. 3, pp. 171–190, 2011, doi: 10.1002/ppap.201000153.

[94] S. T. (Eds. . J. Izdebska, *Printing on Polymers. Fundamentals and Applications*. Oxford, 2016.

[95] N. De Geyter and R. Morent, *Cold plasma surface modification of biodegradable polymer biomaterials*. Woodhead Publishing Limited, 2014.

[96] E. P. Stuckert and E. R. Fisher, "Ar/O2 and H2O plasma surface modification of SnO2 nanomaterials to increase surface oxidation," *Sensors Actuators, B Chem.*,

vol. 208, pp. 379–388, 2015, doi: 10.1016/j.snb.2014.11.049.

[97]   D. P. R. Thanu, E. S. Srinadhu, M. Zhao, N. V. Dole, and M. Keswani, *Fundamentals and applications of plasma cleaning*, vol. 11. Elsevier Inc., 2018.

[98]   Hachioji-shi, "Ultraviolet-Ozone Surface Treatment, Three Bond Tech. News," *Three Bond thechnical news*, vol. 17, pp. 1–10, 1987.

[99]   M. Dietzel, S. Haferl, Y. Ventikos, and D. Poulikakos, "Marangoni and variable viscosity phenomena in picoliter size solder droplet deposition," *J. Heat Transfer*, vol. 125, no. 2, pp. 365–376, 2003, doi: 10.1115/1.1532014.

[100] X. Zhang, W. Yang, J. Qi, and Y. Hu, "Preparing Ambient-Processed Perovskite Solar Cells with Better Electronic Properties via Preheating Assisted One-Step Deposition Method," *Nanoscale Res. Lett.*, vol. 15, no. 1, 2020, doi: 10.1186/s11671-020-03407-9.

[101] P. Kumnorkaew *et al.*, "Interface modification of CH3NH3PbI3/PCBM by pre-heat treatment for efficiency enhancement of perovskite solar cells," *Curr. Appl. Phys.*, vol. 17, no. 4, pp. 488–494, 2017, doi: 10.1016/j.cap.2017.01.015.